Etude de la dynamique auto-entretenue des bandes turbulentes et de la turbulence pleinement développée dans un écoulement de canal

Enza Parente

HESAM UNIVERSITÉ

Arts et Métiers Sciences et Technologies

ÉCOLE DOCTORALE SCIENCES ET MÉTIERS DE L'INGÉNIEUR
Laboratoire Dynfluid - Campus de Paris

THÈSE

présentée par : **Enza PARENTE**
soutenue le : **15 Novembre 2021**

pour obtenir le grade de : **Docteur d'HESAM Université**

préparée à : **École Nationale Supérieure d'Arts et Métiers**
Spécialité : **Mécanique et Matériaux**

Sustaining turbulent bands and fully-developed turbulence in channel flow

THÈSE dirigée par :
M. ROBINET Jean-Christophe, Mme CHERUBINI Stefania

et co-encadrée par:
M. DE PALMA Pietro

Jury

M. Carlo COSSU	Directeur de Recherche,LHEEA, Nantes	Président
Mme Laurette S. TUCKERMAN	Directeur de Recherche, PMMH-ESPCI, Paris	Rapporteure
M. Richard KERSWELL	Professeur, DAMTP, Cambridge University	Rapporteur
M. Yohann DUGUET	Chargé de recherche, LIMSI-CNRS, Orsay	Examinateur
M. Jean-Christophe ROBINET	Professeur, ENSAM Paris	Examinateur
Mme Stefania CHERUBINI	Professeur, DMMM, Politecnico di Bari	Examinateur
M. Pietro DE PALMA	Professeur, DMMM, Politecnico di Bari	Examinateur

THÈSE

Department of Mechanics, Mathematics and Management
MECHANICAL AND MANAGEMENT ENGINEERING
Ph.D. Program
SSD: ING-IND/06–FLUID DYNAMICS
SSD: ING-IND/08-FLUID MACHINERY

Final Dissertation

Sustaining turbulent bands and fully-developed turbulence in channel flow

by
Enza Parente

Referees:

Prof. Laurette S. TUCKERMAN

Prof. Rich KERSWELL

Supervisors:

Prof. Stefania Cherubini

Prof. Jean-Christophe Robinet

Prof. Pietro De Palma

Coordinator of Ph.D Program:
Prof. Giuseppe Pompeo Demelio

Course n°34, 01/11/2018-31/10/2021

Résumé

Cette thèse vise à étudier les principaux mécanismes impliqués dans les écoulements de type canal autour de la transition vers la turbulence. Plus particulièrement, il existe une gamme de nombres de Reynolds pour laquelle la turbulence reste localisée sous la forme de bandes obliques turbulentes plongées dans un écoulement laminaire. Dans cette thèse, les principaux mécanismes à l'origine et responsables de l'évolution de ces bandes turbulentes sont étudiés au travers de techniques d'optimisation linéaires et non linéaires. Tout d'abord, dans un canal de grande dimension, il a été démontré que la perturbation d'énergie minimale capable de générer des bandes turbulentes est localisée et caractérisée par des structures à petite et grande échelles. Selon le nombre de Reynolds, ce *minimal seed* évolue dans le temps avec deux mécanismes différents : pour $Re \lesssim 1200$ une bande oblique isolée est créée ; alors que pour $Re \gtrsim 1200$, une évolution symétrique dans la direction transverse est observée, donnant lieu à deux bandes distinctes. Ensuite, en réduisant la complexité du problème à un domaine incliné, on constate que deux éléments principaux sont nécessaires pour induire la transition vers des bandes turbulentes : i) un mécanisme linéaire de type *lift-up* est nécessaire à la génération des *streaks* à l'intérieur des bandes turbulentes ; ii) des tourbillons à grande échelle assurant la localisation spatiale. Dans la dernière partie de cette thèse, afin d'étudier les structures cohérentes habituellement observées dans les écoulements turbulents, la méthode d'optimisation non linéaire est étendue aux écoulements de canal turbulent et une 'nouvelle' méthode mathématique pour le calcul des solutions cohérentes invariantes est proposées. Dans ces deux méthodes, les équations instationnaires de Navier-Stokes sont écrites en moyenne de Reynolds et sous une forme perturbative autour du champ moyen turbulent ; des solutions en termes de structures à différentes échelles turbulentes sont trouvées.

Mots clés : bandes turbulentes, transition sous-critique, optimisation non-linéaire, écoulement turbulent, structures cohérentes, système dynamique.

Abstract

This thesis aims at studying the main mechanisms involved in transitional and turbulent channel flows. Concerning the transitional channel flow, there is a range of Reynolds numbers for which turbulent oblique bands within the laminar flow are observed. In this thesis, the main mechanisms involved in the origin and growth of these turbulent bands are investigated using linear and nonlinear optimization techniques. First, in a large-sized channel, it is shown that the minimal-energy perturbation able to generate turbulent bands has a spot-like structure characterized by small- and large-scale structures. Depending on the Reynolds number, this minimal seed evolves in time with two different mechanisms: for $Re \lesssim 1200$ an isolated oblique band is created; whereas, for $Re \gtrsim 1200$, a quasi spanwise-symmetric evolution is observed, giving rise to two distinct bands. Then, reducing the problem complexity to a tilted domain, it is found that two main elements are necessary to induce transition towards turbulent bands: i) a linear energy growth mechanism such as the lift-up for generating streaks inside the turbulent bands; ii) large-scale vortices ensuring spatial localisation.
In the last part of this thesis, in order to investigate the coherent structures usually observed in turbulent flows, the nonlinear optimization technique is extended to the turbulent channel flow and a 'new' mathematical framework for the computation of statistically-invariant coherent solutions is proposed. In both techniques, the unsteady Reynolds-Averaged Navier-Stokes equations written in a perturbative form with respect to the turbulent mean flow are used and solutions with structures at multiple turbulent scales are found.

Keywords: turbulent bands, subcritical transition, nonlinear optimization, turbulent flows, coherent structures, dynamical system.

Contents

List of Tables

List of Figures

Summary

It is well known since the experiment of Reynolds (1883) that, in shear flows, turbulence can be triggered for Reynolds number lower than the critical one found via linear stability analysis, so transition to turbulence may arise subcritically. Moreover, in the pipe, plane Couette, and plane Poiseuille flow, there is a range of Reynolds numbers for which, in certain flow conditions, turbulent localised regions coexist with the laminar flow when the statistically-steady turbulent state is reached. Some examples are the puffs in the case of pipe flow or the oblique turbulent bands in the case of plane Couette and Poiseuille flows.

In plane Poiseuille flow, Tsukahara *et al.* (2005) for the first time observed numerically oblique turbulent bands tilted in the streamwise direction and plunged in the laminar flow. In the first part of this Ph.D. work, we are interested in investigating the generation of turbulent bands and understanding the main mechanism involved in the origin and growth of turbulent bands. In the literature, two distinct methodologies have been used to trigger these laminar-turbulent patterns: decreasing the Reynolds number until the statistically-steady turbulent-laminar pattern is reached (Tsukahara *et al.*, 2005; Tuckerman *et al.*, 2014; Kashyap *et al.*, 2020); or perturbing the laminar flow with localised disturbances with enough energy to trigger localised turbulent regions (Duguet *et al.*, 2010; Aida *et al.*, 2010; Tao & Xiong, 2013; Xiong *et al.*, 2015). To find a suitable initial perturbation able to trigger turbulence in the form of a laminar-turbulent pattern, we have investigated the generation of turbulent bands via nonlinear optimization, first used by Cherubini *et al.* (2010*a*) and Pringle & Kerswell (2010), searching for the first time the *minimal seed* in a very large channel flow. Moreover, we have investigated the Reynolds number influence on the optimal growth of perturbations and analysed the mechanism of creation of turbulent bands. In particular, these turbulent bands present a small-scale flow, characterised by streaks and vortices, and are surrounded by a large-scale flow. For this reason, different hypotheses are suggested in the literature concerning their origin linked with these two flow

scales. Some authors conjectured that the streaks constituting the small-scale flow are generated via an inflectional spanwise instability (Xiao & Song, 2020) and these structures at the head of the turbulent bands are responsible for the turbulent band growth and self-sustaining (Shimizu & Manneville, 2019; Song & Xiao, 2020). Conversely, others authors speculate that the large scale flow is responsible for the turbulent band sustaining (Duguet & Schlatter, 2013; Tao *et al.*, 2018). However, the main mechanisms at the origin of the turbulent bands are still not completely clear, especially concerning streaks nucleation. To elucidate this point, in the first part of this work, we search for a possible relation between the optimal energy growth of streaks at the head of the turbulent band and the bands' generation and sustaining. Moreover, we investigate the energy growth mechanism in a tilted domain searching for linear and nonlinear optimal perturbations in tilted and non-tilted domain.

In the second part of this work, the dynamic of a fully turbulent channel flow is analysed. Coherent structures found in turbulent flow are mostly elongated oscillating structures, called streaks; notably, two scales of motions are identified, small scale structures in the near-wall region characterised by a spanwise streaks spacing of $\lambda^+ \approx 100$ and a large scale flow in the outer region with an average spanwise length comparable to the channel half-width. In the near-wall region the small scale structures, characterised by streaks and vortices, are continuously generated through the *self-sustained process* (SPP) (Hamilton *et al.*, 1995; Waleffe, 1997), which is autonomous and does not requires the presence of large scale structures. The study of this self-sustained process lead to the research of *exact coherent structures*, which are invariant solutions of the Navier-Stokes equations, mostly characterised by near-wall structures (Kawahara & Kida, 2001). At the same time, it was observed that the large scale structures populating the turbulent flow in the outer region have the form of large scale oscillating streaks (Tomkins & Adrian, 2003) or packets of hairpin vortices (Adrian, 2007). To analyse if a self-sustained process exists (and is autonomous) also for these large-scale structures, Hwang & Cossu (2010*b*) have performed Large-Eddy Simulations (LES) with an over-filtered Smagorinsky method, finding large scale streaky structures that remain self-sustained even when the small-scale motion is quenched. Using the same approach, Rawat *et al.* (2015) found large-scale exact coherent solutions that exist even in the absence of small-scale oscillations.

Likewise, Farano *et al.* (2017, 2018), searching for nonlinear optimal solutions around the mean flow, have found perturbations able to reproduce extreme events. These optimal perturbations present small- and large-scale structures depending on the friction Reynolds number and on the target time.

For low friction Reynolds numbers, the optimal perturbation exhibits hairpin vortices originated by the breakup of the near-wall streaks; whereas, for higher values of Re_τ, it is mostly composed of large-scale streaks. Following the formulation used by Farano *et al.* (2017), in an attempt for reaching values of Re_τ for which an autonomous self-sustained process at large scale exists, we have tried to extend the nonlinear optimization problem to turbulent flows at larger values of Re for different target times. However, due to the nonconvex nature of the nonlinear Navier-Stokes equations, different local optima are found for a given set of initial energy and target time, undermining the robustness of such approach for finding a preferential energy growth mechanism at high Re for fully turbulent flows. For this reason, we have chosen to follow a different approach attempting to found invariant solutions able to describe the turbulent motions for high values of the Reynolds number. Thus, in the last part of this work we have provided a 'new' mathematical framework for the computation of statistically-invariant coherent solutions of the unsteady Reynolds-averaged Navier-Stokes equations written in a perturbative form with respect to the turbulent mean flow, using a suitable approximation of the Reynolds stress tensor. With this set of equations, solutions with structures at multiple scales are found, without any filtering of small-scale structures, allowing the direct and inverse cascade mechanisms by which energy is transmitted scale-by-scale.

0.1 Organization of the manuscript

In Chapter 1, the context of the work is provided. First, an analysis of the state of the art concerning subcritical transition to turbulence and patterned turbulence in channel flow is provided. Secondly, fundamental notions about optimal perturbation and minimal seed are introduced. Finally, an introduction on the dynamical system approach in fluid dynamics is provided.
Chapter 2 presents the governing equations and numerical methods used in this thesis.
Chapter 3 is dedicated to the research of minimal seed to generate oblique turbulent bands; the numerical strategy and the main results are reported. In Chapter 4, via linear and nonlinear optimizations the main mechanisms allowing the generation of the turbulent bands in tilted domains are presented. Some results on nonlinear optimal perturbation in turbulent channel flow are shown in chapter 5. In Chapter 6, a new strategy to search invariant solutions at high Reynolds numbers is presented and the major results are reported.
Finally, general conclusions and perspectives are provided in Chapter 7.

Chapter 1

Context

Contents

1.1 Subcritical transition to turbulence

There are several open questions in fluid dynamics regarding the transition to turbulence in shear flows. The Reynolds number, defined as $Re = Uh/\nu$, represents the control parameter to characterize the state of the flow. The linear stability analysis allows to establish a critical value Re_c, the *critical Reynolds number*. Above this value ($Re > Re_c$), the flow is asymptotically unstable and small perturbations are able to trigger turbulence in the flow, via a linear mechanism; instead, for $Re < Re_c$ the flow is *linearly* stable. However, since the experiment by Reynolds (1883), who first observed subcritical transition to turbulence in a wall bounded shear flow, it is known that turbulence may arise for Reynolds numbers smaller than the critical one. Indeed, for some shear flows, such as pipe flow and plane Couette flow, the linear stability analysis predicts linear stability at all Re although,

in some conditions, these flows exhibit transition to turbulence and sustained turbulent flow regime. Otherwise, there are flows, such as plane Poiseuille or boundary layer flows, for which linear stability analysis predicts a much higher critical Reynolds number compared to the value for which transition to turbulence is actually observed.

Therefore, in such flows, another critical Reynolds number is introduced, the *global Reynolds number* or *energy Reynolds number* (Re_g). This quantity defines the threshold value of Re below which all the perturbations decay to the laminar flow, and thus the flow is unconditionally stable. Conversely, for $Re > Re_g$ the flow is defined conditionally stable, i.e. the flow becomes unstable only in certain conditions, depending on the perturbation spatial distribution and/or energy. For these reasons, in such flows, transition to turbulence occurs subcritically.

In figure 1.1 the bifurcation diagram representing subcritical transition considering as control parameter the Reynolds number is shown. If $Re < Re_g$, the flow appears only in its laminar state. Conversely, for $Re > Re_c$ the turbulent state is triggered even by infinitesimal perturbations. On the other hand, in the range $Re_g < Re < Re_c$ the laminar and turbulent states are both achievable, depending on the amplitude and shape of the perturbations affecting the laminar state. For example, in the case of the plane Poiseuille flow, linear stability analysis predicts a critical Reynolds number equal to $Re_c = 5772.2$ (Orszag, 1971). This value is much larger compared to the approximate threshold for turbulent transition found experimentally at $Re \approx 1000$, above which turbulent spots are observed and travel into the laminar flow without decaying (Carlson *et al.*, 1982).

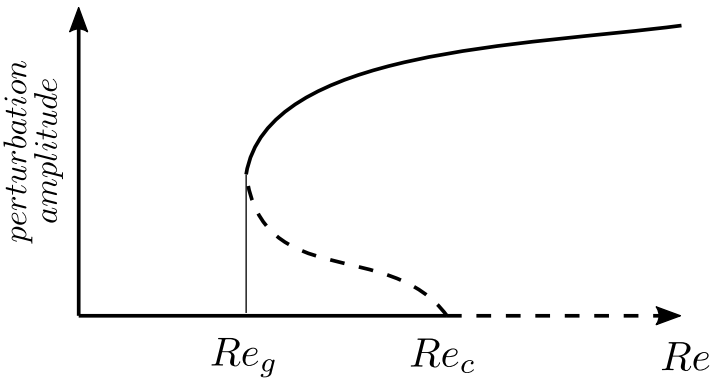

Figure 1.1: Bifurcation diagram for subcritical transition to turbulence in shear flows, as plane Poiseuille flow.

1.1.1 Localised turbulence in shear flows

In the range of Reynolds numbers $Re_g < Re < Re_c$, when the flow departs from the laminar state, two different behaviours may be identified: the flow can be *transitional*, or characterised by a fully developed turbulent regime. In transitional flows, turbulence does not arise at the same time in the whole domain, being preceded by the formation of localised flow structures that grow in amplitude and spread in space. Transition via localised turbulence is definitely realistic, because, in real flow configuration, turbulence is triggered by localised imperfection of the wall surface, acoustic waves, or other spatially compact environmental disturbances.

The first of these localized flow features to be observed were turbulent spots, which have been investigated by many researchers in the past. Emmons (1951) was the first to experimentally show that turbulent spots may trigger turbulence; later, this was confirmed experimentally and numerically in plane channel flow (Carlson *et al.*, 1982; Henningson & Kim, 1991; Klingmann, 1992; Aida *et al.*, 2010, 2011; Lemoult *et al.*, 2013, 2014) and in boundary layer flow (Cantwell *et al.*, 1978; Henningson *et al.*, 1987; Levin & Henningson, 2007) analysing the spots characteristics. In pipe flows, rather, other localized flow structures dubbed *puffs* are observed both numerically and experimentally (Eckhardt *et al.*, 2007; Avila *et al.*, 2011). Puffs are localised, downstream-travelling flow structures within a laminar field, sustained by the energy provided by the neighbouring laminar motion at the upstream end of the puff. They can decay, split or merge, filling the laminar flow with turbulent fluctuations.

More recently, Duguet *et al.* (2010) have shown that locally perturbing the plane Couette flow, the fully turbulent state is preceded by the formation of turbulent bands. The same behaviour was observed by Tao & Xiong (2013) and Xiong *et al.* (2015), where it was observed that, after injecting a localised perturbation, turbulent bands grow obliquely in the domain until decay or breakdown to turbulence. In the latter case, it was determined that the turbulent bands lifetime is longer than that of turbulent spots. Besides having a crucial role in the turbulent transition, oblique turbulent bands characterise also the (transiently) turbulent state in shear flows at low Reynolds numbers, as shown by Tsukahara *et al.* (2005). In fact, in the pipe, plane Couette, and plane Poiseuille flow, there is a range of moderate Reynolds numbers for which experiments and numerical simulations have shown that turbulence is not homogeneous in space, since spatially-localized regions characterised by laminar and turbulent behaviour coexist when the statistically-steady turbulent state is reached.

Indeed, elongated oblique self-sustained turbulent bands located in a laminar flow appear in plane

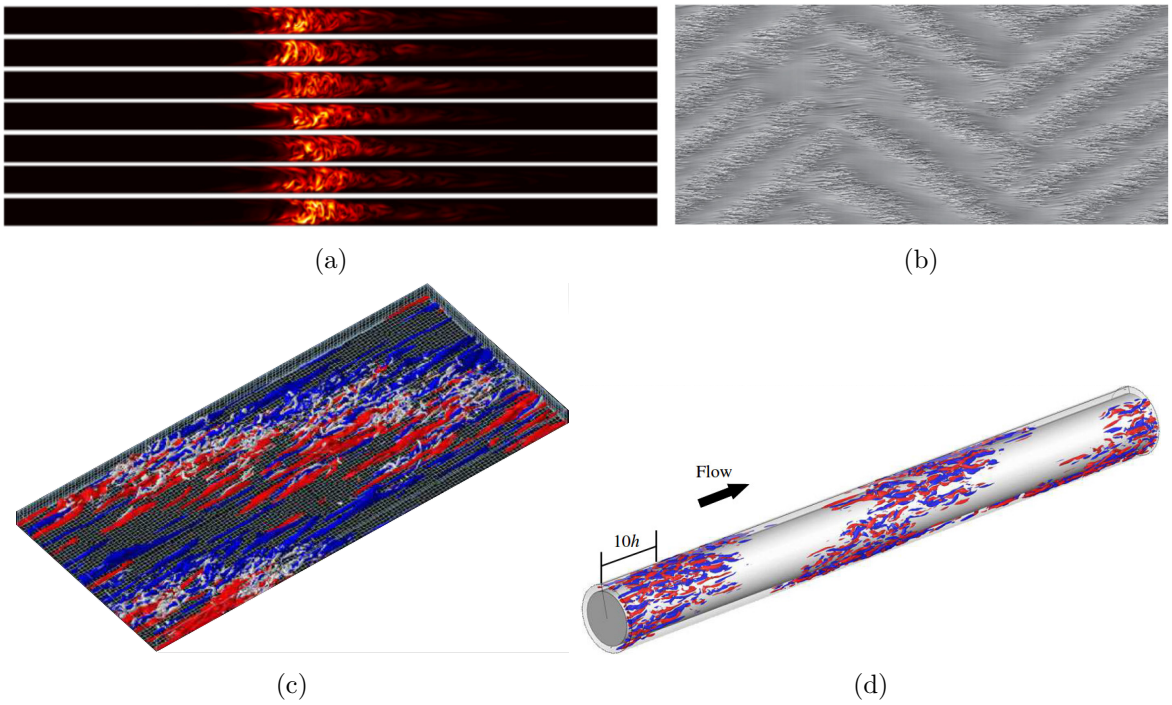

Figure 1.2: Localised turbulence in shear flow. (a) Puff evolution in round pipe flow at $Re = 2000$ (from Song *et al.* (2017)). (b) Turbulent-laminar bands in Coeutte flow at $Re = 330$ (from Duguet *et al.* (2010)). (c) Turbulent bands in plane channel flow (from Tsukahara *et al.* (2005)). (d) Localised helical turbulence in annular Couette flow (from Kunii *et al.* (2019)).

Couette flow at $Re > 290$ (Prigent *et al.*, 2002; Barkley & Tuckerman, 2005; Duguet *et al.*, 2010; Tuckerman & Barkley, 2011) and in plane Poiseuille flow for $Re \geq 1000$ (Tsukahara *et al.*, 2014; Tuckerman *et al.*, 2014; Tao *et al.*, 2018; Shimizu & Manneville, 2019; Kashyap *et al.*, 2020). In particular, due to the symmetry in the streamwise direction, in the Couette flow the turbulent bands are stationary; while, in the plane Poiseuille flow are free to travel in the streamwise direction.

This turbulent laminar pattern is also observed in the form of a helically-shaped turbulent patch in counter-rotating Taylor Couette flow by Coles & Van Atta (1966) and in annular Couette flow for a particular ratio of the two coaxial cylinders by Kunii *et al.* (2019). Turbulent bands are also found in a channel with heat transfer (Tsukahara *et al.*, 2006). Furthermore, Deusebio *et al.* (2015) extended the analysis of intermittent flows in stratified Couette flow, identifying the region of existence varying the Reynolds and Richardson numbers. Turbulent bands in channel flow exhibit a magnetic field are found by Zikanov *et al.* (2014). A more detailed analysis of turbulent-laminar patterns in shear flows is tackled in review of Tuckerman *et al.* (2020).

1.1.2 Turbulent bands in channel flow

As previously mentioned, in plane Poiseuille flow turbulent-laminar oblique patterns were observed experimentally for $Re = 1000$ by Carlson *et al.* (1982). Tsukahara *et al.* (2005) numerically observed localised turbulent bands tilted in the streamwise direction within in a laminar flow. Numerical simulations were able to reproduce these patterns also at lower Reynolds numbers (Xiong *et al.*, 2015; Tao & Xiong, 2017; Kashyap *et al.*, 2020), estimating a threshold value for turbulent bands at $Re \approx 660$, according to Tao *et al.* (2018). Moreover, Song & Xiao (2020) recently reported the onset of turbulent bands even at Reynolds number as low as $Re = 500$, generated by forcing the flow with a local perturbation with a sufficiently strong spanwise inflection. They showed that this forcing method allows to generate bands at very low values of the Reynolds number, for which bands previously appeared to be not sustained. This procedure was motivated by the work of Xiao & Song (2020), where the authors performed a linear stability analysis of the mean velocity profile extracted in a small domain at the head of the turbulent band. Employing stability analysis, it was suggested that spanwise inflectional instability may be the mechanism involved in the growth and self-sustaining process of turbulent bands.

1.1.2.1 Domain size influence on turbulent bands dynamics

In addition to the Reynolds number, the domain size plays an important role in the growth and self-interaction of turbulent bands. When the domain considered is sufficiently large, turbulent bands can grow for longer times, avoiding the probability of interaction with themselves or other bands. For this reason, several works were performed to study the influence of the domain extension on the onset of turbulent bands. Further, in a large domain, it is possible to analyse the competition between angle and wavelength. In fact, in channel flow, varying the Reynolds number it was observed that turbulent bands may arise with different angles in the range $24° - 40°$ (Xiong *et al.*, 2015; Kashyap *et al.*, 2020). In order to reduce the computational cost, some numerical studies cleverly considered computational domains tilted in the direction of the bands, as done for the plane Couette flow by Barkley & Tuckerman (2005) and for the plane Poiseuille flow by Tuckerman *et al.* (2014). Although very interesting for studying the dynamics of a single band, using the tilted domain constrains the turbulent bands to develop at a fixed angle and avoids (or reduces) the interactions with other bands, resulting in a consequently less rich dynamics.

1.1.2.2 Generating turbulent bands in channel flow

In the literature, two strategies are typically used to obtain laminar-turbulent bands. The first one consists in starting from a spatially-homogeneous statistically-steady turbulent state, and slowly decreasing the Reynolds number until patterned laminar regions in the initially turbulent flow begins to be observed (Tsukahara *et al.*, 2005; Tuckerman *et al.*, 2014; Kashyap *et al.*, 2020). This method usually leads to the formation of statistically-steady laminar-turbulent patterns. The figure 1.3 shows the spanwise velocity evolution corresponding to a direct numerical simulation in which the Reynolds number is decreased in decrements of 100. For $Re = 2300$, turbulence is statistically uniform in the whole domain. For $1900 < Re < 1400$, turbulent bands appear in the domain. Further decreasing the Reynolds number, the flow complexity is reduced until a single band is identified in the flow.

Another possible method to obtain the turbulent bands consists in perturbing the laminar flow

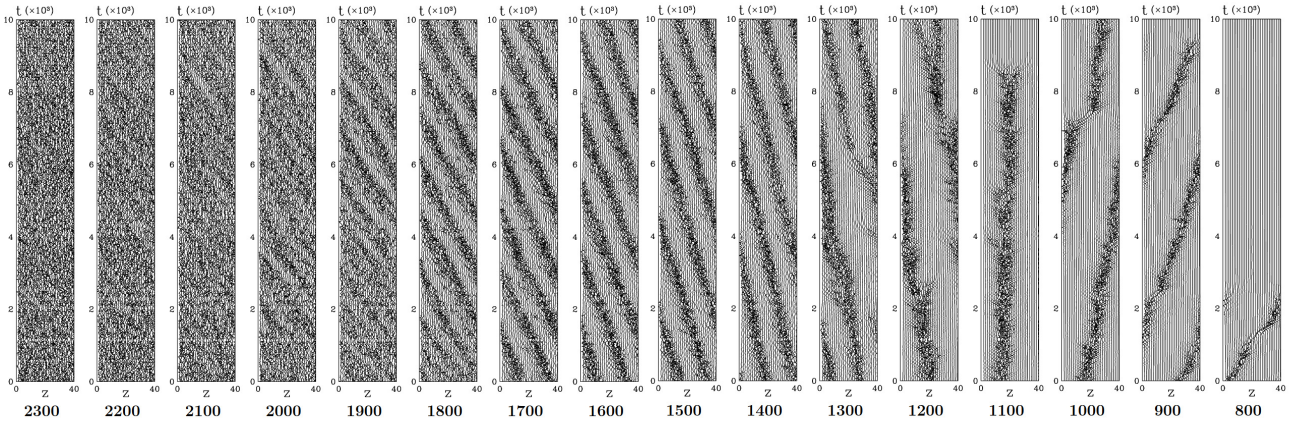

Figure 1.3: Spanwise velocity evolution corresponding to a simulation in which the Reynolds number is decreased in decrements of 100. The visualization shows the transition from a fully developed turbulent flow to the laminar-turbulent pattern at low Reynolds numbers (from Tuckerman *et al.* (2014)).

with suitable localised disturbances having enough energy to trigger localized regions of turbulence eventually evolving into oblique stripes (Duguet *et al.* (2010), Aida *et al.* (2010), Aida *et al.* (2011), Tao & Xiong (2013), Xiong *et al.* (2015)).

When focusing on the second method, the amplitude, the shape and the localization of these initial perturbations should be carefully chosen to ensure their growth towards oblique bands. Depending on their shape, perturbations with higher amplitude may decay, while weaker perturbations may lead the flow to transition.

1.1.2.3 Turbulent bands origin and growth

Recently, many works have focused on the origin and growth of turbulent bands. In a large domain, Shimizu & Manneville (2019) observed that streaks are generated at the head of the turbulent band and suggest that streaks generation could be the origin of the self-sustaining process of a single turbulent band. According to this hypothesis, investigating a small domain at the head of the band, Xiao & Song (2020) have performed a linear stability analysis of the mean flow computed in three different regions at the head of the band. They have notably found that an inflectional spanwise instability generates streaks structures similar to those found at the head of a turbulent band, and they have proposed that this instability can be at the origin of the growth of the turbulent band. Based on this hypothesis, Song & Xiao (2020) have searched for a forcing that induces inflectional instability in the flow, able to trigger turbulence in the form of turbulent bands in a large domain. On the other hand, using a nonlinear approach Paranjape *et al.* (2020) have searched for an edge state in a tilted domain and they have found a localised nonlinear travelling wave solution that shows properties very similar to those of turbulent bands in a tilted domain.

Conversely, Tao *et al.* (2018) suggest that, for triggering and sustaining a turbulent band, a large-scale

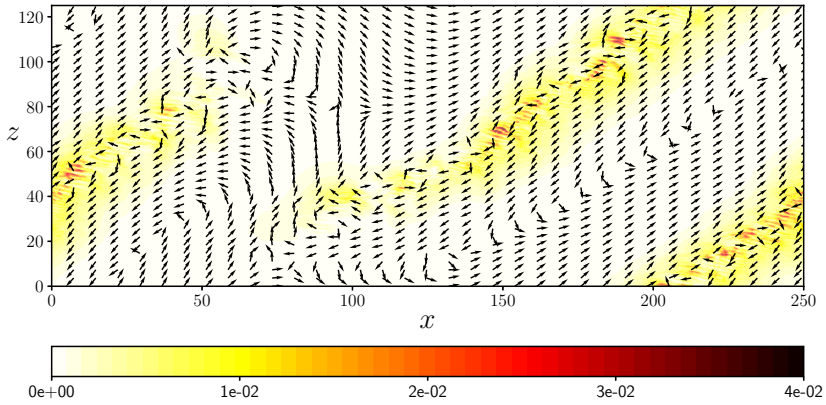

Figure 1.4: Isocontours of the crossflow energy with the normalized y-integrated large scale flow (vectors) obtained with a DNS at $Re = 700$.

flow is necessary. In fact, as shown in figure 1.4, all turbulent bands are characterized by a small-scale flow inside the turbulent region, characterised by streaks and vortices, surrounded by large-scale vortices, parallel to the turbulent bands and having opposite directions on their two sides. In particular, Duguet & Schlatter (2013) have argued that the validity of the continuity equation for this large-scale

flow is responsible for the turbulent band oblique evolution.

Shimizu & Manneville (2019) observed that turbulent bands are sustained by an active streak generation at the head of the bands, while streaks decay is found in the tail. Moreover, Tao *et al.* (2018) reported a strong increase of the total disturbance kinetic energy corresponding with the creation of turbulent bands. This energy increase follows an almost algebraic growth, instead of an exponential behaviour, as should be expected in the case of asymptotic instability as that reported by Xiao & Song (2020).

1.2 Optimal perturbation in shear flows

How explained previously, small perturbation theory (i.e. linear stability analysis) predicts that the primary instability arising in shear flows is characterised by two-dimensional perturbations such as Tollmien-Schlichting waves, found in the case of plane channel or boundary layer flows. However, Kendall (1985) and Matsubara & Alfredsson (2001) have experimentally observed streaks in the transitional regime, linking this coherent structures to secondary instability and *bypass transition*. Notably, it was also proposed that the growth of the streaky structures may be linked to transient growth theory. From a mathematical point of view, Landahl (1980) and Trefethen *et al.* (1993) showed that the non-normality of the linearised Navier-Stokes equations can be responsible for linear transient amplification of the perturbations. In this case, perturbations having an initially small amplitude can reach in a finite time a very large energy, being able to trigger nonlinear effects bringing the flow to transition at Reynolds numbers lower than the critical one. Butler & Farrell (1992) and Reddy & Henningson (1993) suggested that non-modal growth can arise from the interaction of damped eigenmodes, which are nearly anti-parallel. In order to investigate the potential amplification that non normality can provide to the flow, one can search numerically, in a linear framework, for the perturbations causing the maximum possible transient energy amplification, called *optimal perturbations*. These *optimal* flow structures exhibit the maximum possible growth in a given finite time. In particular, Farrell (1988) have shown that in channel flow the linear optimal perturbation is always characterised by streamwise-independent structures of alternating high- and low- momentum, called *streaks* (see figure 1.5). Particularly, for plane channel and boundary layer flows, it has been found that an algebraic kinetic energy growth of perturbations is induced when weak counter-rotating vortices generate high-amplitude streaky structures through a linear mechanism, labelled *lift-up* mechanism.

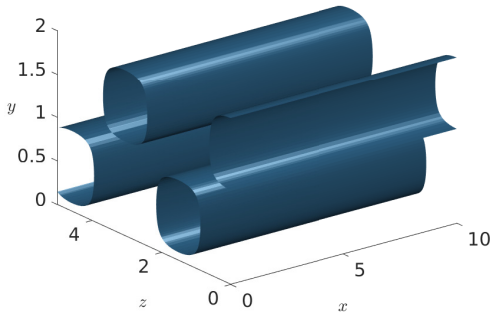

Figure 1.5: Three-dimensional representation of streaks and counter-rotating vortices for Poiseuille flow at Re = 1000, $\alpha = 0$ and $\beta = 2.05$.

These two flow structures, which are easily retrieved by optimal transient growth analysis (Luchini, 2000), are two of the fundamental elements of the self-sustaining process which supports turbulence in shear flows (Hamilton *et al.*, 1995; Waleffe, 1997), together with secondary instability of the streaks which is linked to the creation of inflectional points in the velocity profiles.

1.2.1 Optimal perturbations in the nonlinear framework

However, these streamwise-invariant, spatially elongated structures are different from perturbations that are usually observed in real flows during transition. Indeed, as introduced in the previous sections, in real flow transition to turbulence is observed in the form of localised structures as puffs, spots and turbulent bands, whereas linear optimal disturbance are virtually extended in the whole domain. The formation of turbulent spots from localized perturbations for $Re_g < Re < Re_c$ has been investigated in channel and boundary layer flows (Henningson *et al.*, 1993; Levin & Henningson, 2007). Perturbations with "simple" shapes such as pulses, jets (Singer & Joslin, 1994) or localized pairs of alternated vortices (Levin & Henningson, 2007) have been often used to study the spot formation, since they are usually easy to reproduce experimentally. However, in these studies, the initial perturbation does not guarantee an energy growth as large as that induced by optimal perturbations, so these perturbations usually require a large initial amplitude to trigger turbulence within the flow. Whereas, extending the research of the optimal perturbation to a nonlinear framework have shown that nonlinear optimal perturbations are more efficient in term of energy growth compared to the linear ones. These nonlinear optimal perturbations are characterised by wavy streaks and vortices, but, compared to the linear

perturbations, are strongly localised in the domain, so they are able to induce transition with a much smaller energy then their linear counterpart.

The methodology to find these perturbations is based on nonlinear variational optimization, which has been performed for pipe flow by Pringle & Kerswell (2010) and Pringle *et al.* (2012), for boundary layer flow by Cherubini *et al.* (2010*a*), Cherubini *et al.* (2011), Cherubini *et al.* (2015) and Vavaliaris *et al.* (2020), and for plane Couette flow by Monokrousos *et al.* (2011), Rabin *et al.* (2012), Duguet *et al.* (2013) and Cherubini & De Palma (2013). These authors optimize a functional linked to the turbulent dynamics, namely the perturbation kinetic energy (see Pringle & Kerswell (2010); Pringle *et al.* (2012); Rabin *et al.* (2012); Cherubini & De Palma (2013)) or the time-averaged dissipation (see Monokrousos *et al.* (2011); Duguet *et al.* (2013)), including nonlinear terms into the optimization and thus following the evolution of the perturbation until transition is initiated. The whole procedure is explained in detail in Chapter 2.2, while results on the plane Poiseuille flow are provided in Chapters 3-4.

1.3 Self-sustaining process in wall-bounded flow

As previously mentioned, both linear and nonlinear optimal perturbations are characterized by streamwise streaks and vortices, indicating that these structures are linked to a robust energy-production mechanism typical of shear flows. In fact, streaks are the most typical example of coherent motion in turbulent flows, first observed by Kline *et al.* (1967) as "surprisingly well-organized spatially and temporally dependent motions". These elongated structures are continuously generated by the lift-up mechanism, as introduced by Landahl (1980), which is one of the building blocks of the *self-sustained cycle* theorized in the nineties by Hamilton *et al.* (1995) and Waleffe (1997). When the streaks, produced from streamwise vortices via the lift-up mechanism, reach a sufficiently large amplitude they become unstable via an inflectional instability (Waleffe, 1995; Reddy *et al.*, 1998), which leads to their breakdown. Via a nonlinear mechanism, the streaks breakdown regenerates the streamwise vorticity, that creates the streamwise vortices. Notably, for some values of Reynolds numbers, and for some streamwise and spanwise wavelengths, this process is self-sustained. In particular, this self-sustained process (SSP) consists of three steps, as sketched in the schematic representation in figure 1.6: i) streaks generation via streamwise vortices thanks to the non modal lift-up mechanism; ii) streaks breakdown due to nonlinear saturation and secondary instability; iii) nonlinear interactions recreating

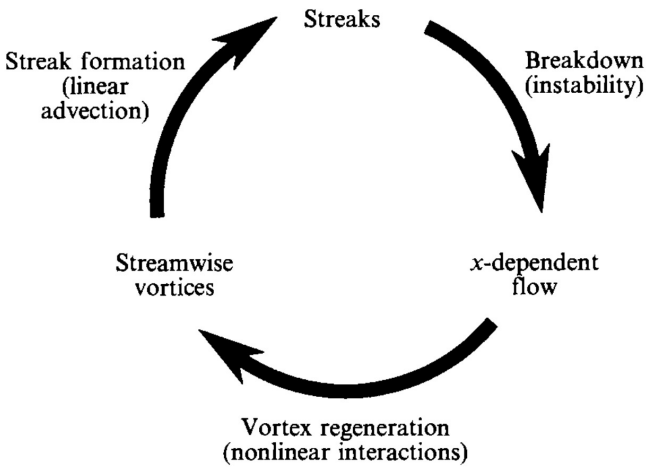

Figure 1.6: Schematic representation of the self-sustaining process (from Hamilton *et al.* (1995)).

the streamwise vorticity, leading back to the first step.

It is important to notice that the streaky motion is not only observed in the transitional regime, but also in the fully turbulent flows. In the latter case, streaky structures having different scales characterise the fully turbulent flow, ranging from the inner scale, characterising the coherent structures populating the near wall region, to the outer scale, typical of much larger structures observed in the outer region. Kline *et al.* (1967) have indicated that the spanwise spacing of streaks observed in the near wall region of a boundary layer, is approximately $\lambda^+ \approx 100$, in wall units (i.e. normalized using u_τ and the viscous length scale $\delta_\nu = \nu/u_\tau$). This spanwise spacing is found for other shear flows, and is invariant with the Reynolds number, as noticed by Smith & Metzler (1983). Conversely, the outer region is constituted by large-scale coherent structures in the form of large-scale oscillating streaks (Tomkins & Adrian, 2003) or packets of hairpin vortices (Adrian, 2007) with average spanwise length $\lambda \approx \mathcal{O}(h)$, with h the outer length scale (i.e. the channel half width or the boundary layer thickness). Namely, these structures present typical streamwise and spanwise size of $\lambda_x \approx 2-3h$ and $\lambda_z \approx 1-1.5h$, respectively.

Although the self-sustained process was initially observed in the inner layer region (Hamilton *et al.*, 1995; Waleffe, 1997; Jiménez & Pinelli, 1999), a growing body of evidence has recently indicated that equivalent, mutually independent regeneration cycles are active in the logarithmic and outer regions as well (Hwang & Cossu, 2010*a*,*b*, 2011; Hwang, 2015; Hwang *et al.*, 2016*a*; Cossu & Hwang, 2017), giving rise to large- and very-large-scale motion with average streamwise wavelength $\lambda_x \approx \mathcal{O}(10h)$ (Kovasznay *et al.*, 1970; Komminaho *et al.*, 1996; Kim & Adrian, 1999; del Alamo & Jiménez, 2003;

Hutchins & Marusic, 2007). The statistical and dynamical features of these self-sustaining motions associated with streaks and quasi-streamwise vortices at different scales are consistent with the attached eddy hypothesis introduced by Townsend (1980).

1.3.1 Self-sustaining process at large scale

Concerning the origin and dynamics of the large scale structures, a diffused hypothesis is that their formation is linked to a mechanism similar to the self-sustaining process of the transitional flows. In plane channel and boundary layer flows, del Álamo & Jiménez (2006); Pujals *et al.* (2009) and Cossu *et al.* (2009) have performed a linear transient growth analysis of perturbations of a mean velocity profile of a fully turbulent flow, modelling the small coherent motion with an eddy viscosity. By means of this analysis, they have confirmed the previously mentioned conjecture, concluding that a *coherent lift-up* mechanism and a consequent self-sustained process are detected also for large-scale structures. In particular, in the case of plane channel flow, for large Reynolds numbers the optimal gain presents two peaks at two optimal spanwise wavelengths (del Álamo & Jiménez, 2006; Pujals *et al.*, 2009), one scaling in outer units with an optimal wavelength $\lambda_z \approx 4h$, and the second scaling in inner units with $\lambda_z^+ \approx 100$, consistent with the spanwise spacing of the near-wall streaks. Moreover, according to experimental evidence, the maximum energy growth of the optimal perturbation associated with the outer scales increases with the Reynolds number; conversely, the energy growth at the inner scale is smaller and invariant to the Reynolds number (see figure 1.7).

In turbulent shear flows, the large-scale motions interact with the structures at small scales. In order

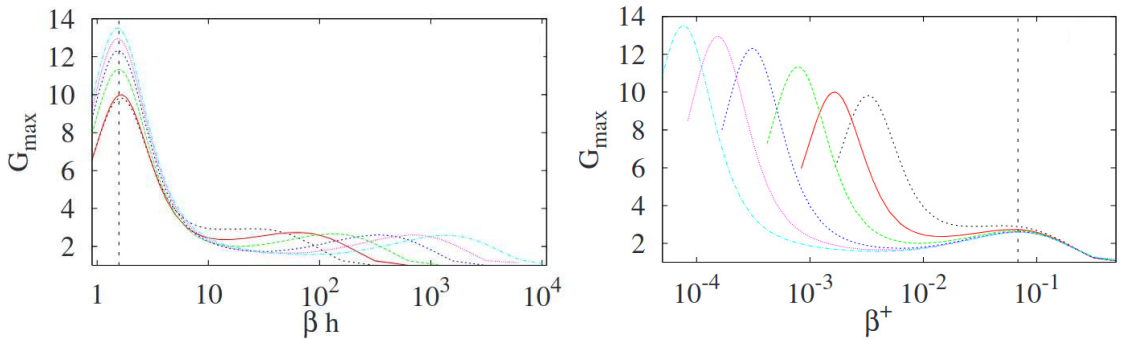

Figure 1.7: Maximum growth G_{max} evolution in function of the spanwise wavenumber for different Reynolds numbers. Representation: (a) in outer units with an optimal spanwise wavelength $\lambda_z \approx 4h$; (b) in inner units with an optimal spanwise wavelength $\lambda_z^+ \approx 92$ (from Pujals *et al.* (2009)).

to establish whether the large scale self-sustaining process is independent of the near-wall process, Hwang & Cossu (2010*a*) have performed Large-Eddy Simulations (LES) in both channel and Couette flow filtering and artificially increasing the Smagorinsky constant C_S, i.e. the cut-off characteristic length, to suppress the small scale motion. Even in this artificially quenched case, they still observed large-scale streaky structures. This result have clearly demonstrated that the large-scale motion can be self-sustained, since it survives when smaller-scale active motions in the near-wall and in the logarithmic regions are artificially quenched and replaced by purely dissipative structures. Hwang & Cossu (2011) extended this method to intermediate flow units finding self-sustained streaky structures with length characteristic of the logarithmic layer motion.

However, this over-filtered approach does not allow the investigation of the nature of the energy transfer between structures of different scales. Despite the motion at large scales can be sustained even when the wall cycle is quenched, in high-Reynolds-number turbulent flows multiple and non-trivial interactions exist between structures at different scales (Cimarelli *et al.*, 2016; Cho *et al.*, 2018). In a very recent work, Doohan *et al.* (2021) have shown that wall-normal energy is transferred from large to small scales inducing energy production at the wall via the Orr mechanism. While, a non-negligible amount of energy is transferred from small to large scales Cho *et al.* (2018), possibly due to small-scale sinuous streak instability as conjectured by Doohan *et al.* (2021). Thus, coherent structures at different scales are intimately connected by direct and inverse cascade mechanisms by which energy is transmitted scale-by-scale among different regions of the flow Cimarelli *et al.* (2016).

Using the perturbative Reynolds-Averaged Navier-Stokes equations (PRANS), Farano *et al.* (2017, 2018) have found nonlinear optimal perturbations characterised by hairpin vortices originated by the breakup of the near-wall streaks for low values of friction Reynolds number; and, at higher friction Reynolds numbers, the nonlinear optimal perturbation consists in large-scale and small-scale streaks. Moreover, these nonlinear optimal perturbations may reproduce high-energetic events, such as ejections and sweeps, recurrently observed in wall-bounded turbulent flows (Farano *et al.*, 2017). These optimal perturbations can provide crucial information about the interaction of energetic structures at different scales, and the related mechanisms of energy exchange and production. The whole optimization procedure is explained in detail in the next chapter, while some results on the plane Poiseuille flow are provided in Chapter 5.

1.4 Dynamical system view in fluid dynamics

In an effort to model the dynamics of turbulent shear flow, Hopf (1948) conjectured that a chaotic saddle composed of invariant solutions of the Navier-Stokes equations sustains transient turbulence in shear flows. The first nontrivial fixed point of the Navier-Stokes equations was found by Nagata (1990) in plane Couette flow and later recovered by Waleffe (1998). Starting from this solution, Waleffe (2001) extended the research of invariant solutions also in plane Poiseuille flow, via a homotopy continuation from the plane Couette to the plane Poiseuille flow. The invariant solution found by Waleffe (2001) showed the same features of the near-wall structures, i.e. streaks flanked by streamwise vortices. For these reasons he decided to call these structures *exact coherent structures*. Furthermore, the periodic orbit found by Kawahara & Kida (2001) in the plane Couette flow was found to show similar near-wall structures, exhibiting all the phases of the self-sustaining process (see figure 1.8).

The same three fundamental mechanisms that compose the regeneration cycle of wall turbulence

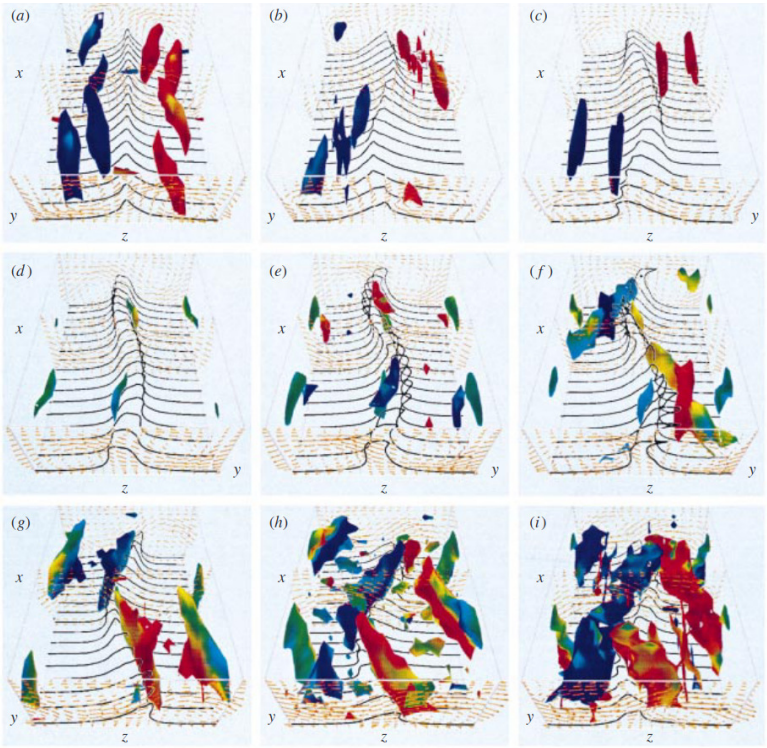

Figure 1.8: Periodic orbit found by Kawahara & Kida (2001) exhibiting the self-sustaining process.

have been found to sustain several invariant solutions of the Navier-Stokes equations in the form of equilibria, travelling waves or (relative) periodic orbits (Faisst & Eckhardt, 2003; Hof *et al.*, 2004;

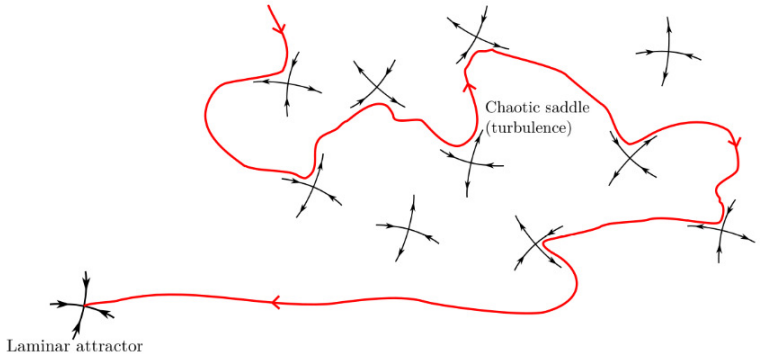

Figure 1.9: Schematic visualization of a transient trajectory in the phase space (from Kreilos (2014)).

Wedin & Kerswell, 2004; Eckhardt *et al.*, 2007; Duguet *et al.*, 2008; Gibson *et al.*, 2009; Schneider *et al.*, 2010; Willis *et al.*, 2013; Deguchi *et al.*, 2013; Gibson & Brand, 2014; Zammert & Eckhardt, 2014; Park & Graham, 2015; Barnett *et al.*, 2017; Budanur *et al.*, 2017).

Performing the stability analysis on these solutions, one or more eigenvalues exhibiting asymptotic growth are found, which implies the unstable nature of the coherent exact solutions. Thus, as sketched in figure 1.9, the chaotic saddle consists of a series of invariant solutions and, being these solutions unstable, trajectories in the state space may approach one of these solutions, remain in their neighborhood for a finite time before being pushed away along one of the unstable directions to approach other solutions through heteroclinic orbits (Farano *et al.*, 2019), resulting in a chaotic walk in the state space.

Typical coherent structures populating transitional and turbulent flows, such as streaks and streamwise vortices, have been successfully captured by these fully nonlinear, dynamically unstable solutions of the Navier-Stokes equations which populate state space and support turbulent dynamics with their entangled stable and unstable manifolds.

Many efforts have been done for deriving low-order models based on these invariant solutions, allowing to accurately describe the statistical properties of a turbulent flow (Cvitanović, 2013). Recently, Chandler & Kerswell (2013) successfully applied the periodic orbit theory to the case of a two-dimensional Kolmogorov flow at a moderate Reynolds number. However, a low-order model of a fully developed three-dimensional turbulent flow is yet to be achieved, and would probably require the discovery of many new invariant solutions at sufficiently high Reynolds number. Unfortunately, the computation of such invariant solutions at large Reynolds numbers is a hard challenge, due to the multiple bifurca-

tions they typically undergo. In the case of fully turbulent flows at high friction Reynolds number, a valuable approach for computing invariant solutions is resorting to Large-Eddy Simulations (LES), as proposed by Hwang & Cossu (2010*b*, 2011). In particular, choosing filtering widths larger than those typically used for reproducing results of Direct Numerical Simulations (DNS), allows one to filter out a large range of scales that could not be resolved within the chosen numerical grid. This approach, relying on "over-filtered" LES, with the Smagorinsky constant C_S controlling the strength of the filtering, is well suited for investigating the self-sustained nature of coherent large-scale motion, as done at first for the plane channel flow by Hwang & Cossu (2010*b*, 2011) and Rawat *et al.* (2016), and for the plane Couette flow by Rawat *et al.* (2015) at relatively low Reynolds numbers and for the channel and asymptotic suction boundary layer flow at large friction Reynolds numbers Hwang *et al.* (2016*b*); Azimi *et al.* (2020). However, this overfiltered approach does not allow to investigate the nature of the energy transfer between coherent structures of different scales. A deeper understanding of the energetic bond connecting small- and large-scale structure in turbulent flows can be achieved by the computation of statistically-invariant coherent states which characterise the multiple-scale, coherent part of the motion around the turbulent mean flow, without any filtering of small-scale structures, as proposed in Chapter 6.

1.4.1 Edge of chaos

In the phase space, it is possible to identify a boundary that delimits the basin of attraction of the laminar state. This boundary separates the initial conditions that decay to the laminar fixed point to the perturbations that visit the chaotic saddle. The concept of the laminar-turbulent separatrix was introduced by Itano & Toh (2001) and later called *edge of chaos* by Skufca *et al.* (2006).

The invariant solutions that lay on this hyper-surface are called edge states. These solutions are relative attractors, i.e., they are attractive for initial conditions on the edge of chaos but repelling for perturbations having a component transverse to this hypersurface. The edge states can be multiple and made by equilibrium points (Schneider *et al.*, 2008), nonlinear travelling waves (Viswanath, 2008; Rawat *et al.*, 2016; Paranjape *et al.*, 2020), periodic or relative periodic orbits (Itano & Toh, 2001; Kreilos *et al.*, 2013; Rawat *et al.*, 2014).

According to the theorems on the uniqueness of the solution of differential equations (Coddington & Levinson (1995), Chapter 1) every initial condition presents only one possible trajectory that might

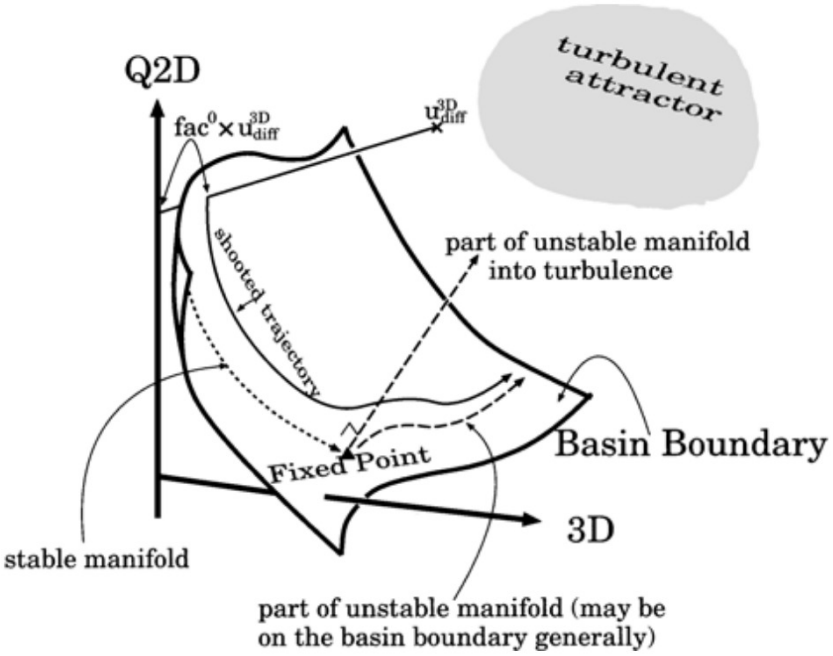

Figure 1.10: Schematic visualization of the phase space (from Itano & Toh (2001)).

decay towards the laminar state or diverge in the turbulent attractor. However, in the cases under consideration, turbulence is not due to the presence of a turbulent attractor, but to a chaotic saddle, on which perturbations walk for a limited (long) time before decaying to the laminar fixed point. Thus, in order to identify the perturbations that characterise the surface between laminar and turbulent behavior we should evaluate the lifetime of perturbations. The lifetime of an initial condition is defined as the time it takes the trajectory to approach the neighborhood of the laminar fixed point. Following this definition, perturbations characterised by a finite lifetime are in the basin of attraction of the laminar solution; on the contrary, perturbations with infinite lifetime pertain to the edge of chaos. To compute the states on the edge of chaos, it is necessary to use an edge-tracking technique. As introduced by Itano & Toh (2001) and Toh & Itano (2003), it is possible to constrain the solution to remain in a neighbourhood of the edge of chaos by a one-parameter bisection technique, this method is labelled "shooting method". This procedure is described in detail in Chapter 2.3.1.

1.4.2 Minimal seeds for turbulent transition

From a state-space point of view, the problem of finding perturbations eventually leading to turbulence consists in placing the starting point of the trajectory outside the boundary of the basin of

attraction of the laminar solution. Notably, the most relevant point of this boundary is its energy

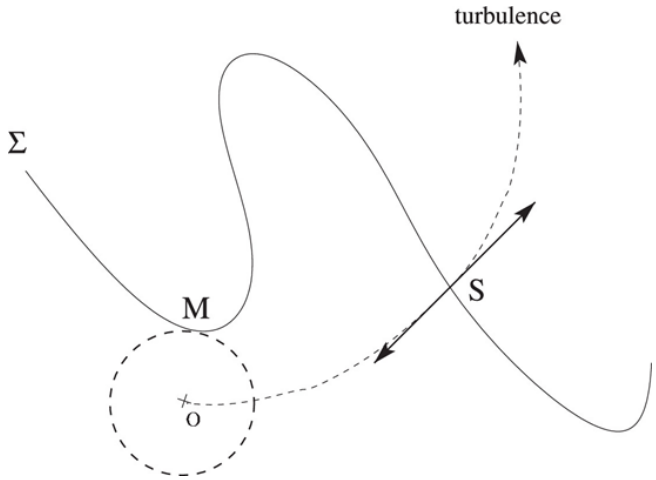

Figure 1.11: Schematic view of the energy minimum. O is the (stable) laminar state with is basin of attraction B(O). M is the minimal perturbation able to trigger transition to the turbulent state and S is the edge state(from Duguet *et al.* (2013)).

minimum, since it represents the minimal (in energy norm) perturbation of the laminar state that can lead the flow to transition. This point in the phase space has been dubbed, by Rabin *et al.* (2012), *minimal seed* for turbulent transition. Looking at the figure 1.11, the point O is the stable laminar flow (fixed point) with its basin of attraction B(O) delimited by the hypersurface Σ. On this surface, it is possible to identify the minimal seed in M, i.e. the point having the minimal distance from O, representing the minimal energy required for escaping from the laminar attractor. This energy minimum has been assessed for several shear flows, allowing to find minimal thresholds for transition. The determination of these energy thresholds is of primary importance for control purposes, since passive or active control methods such as boundary manipulation (Rabin *et al.*, 2014) or profile flattening (Marensi *et al.*, 2019) able to increase this minimal energy would render these flows less prone to transition.

To find these *minimal* perturbations, the nonlinear optimization detailed in Chapter 2 is coupled with an energy bisection as introduced by Rabin *et al.* (2012) for plane Couette flow, and than carried out by Duguet *et al.* (2013) for plane Couette flow and by Cherubini *et al.* (2015); Vavaliaris *et al.* (2020) for boundary layer flow. In all these studies, the kinetic energy was considered as the objective function of the optimization and the optimal perturbations associated with the minimal input energy were spatially localised. Similar behaviour was found in Couette flow by Monokrousos *et al.* (2011)

maximizing the time integral of the entropy production. A detailed review of these methods is reported in Kerswell *et al.* (2014); Kerswell (2018).

The minimal seeds obtained using the optimization-and-bisect method are found to change with the Reynolds number, presenting a power-law scaling of the initial energy $E_{0_{min}} \propto Re^{-\gamma}$. In particular, in plane Couette flows, a minimal energy threshold varying with the Reynolds number as $Re^{-2.7}$ has been found by Duguet *et al.* (2013), in quantitative agreement with experimental estimates for pipe flows. Whereas, for the asymptotic-suction boundary layer Cherubini *et al.* (2015) found a scaling law of this energy threshold of Re^{-2}. However, to the authors knowledge, the minimal seed computation has never been carried out for the channel flow. Moreover, all the minimal seed computations reported in the literature have been carried out in small domains, not allowing to observe laminar-turbulent patterned flow states. In large domains, where laminar-turbulent oblique bands exist, the minimal transition thresholds can be potentially different from that obtained in small domains. Moreover, the analysis of these minimal perturbations and of their evolution towards oblique bands can potentially unveil the main mechanisms leading to the formation and sustainment of these laminar-turbulent patterns. To investigate these points, we compute minimal seeds for triggering turbulent bands in plane Poiseuille flow, as will be discussed in detail in Chapter 3.

Chapter 2

Governing equations and numerical methods

Contents

2.1 Problem formulation

The incompressible flow dynamics in shear flows is governed by the Navier-Stokes equations:

$$\begin{cases} \nabla \cdot \mathbf{u} = 0 \\ \dfrac{\partial \mathbf{u}}{\partial t} = -(\mathbf{u} \cdot \nabla)\mathbf{u} - \nabla p + \dfrac{1}{Re}\nabla^2 \mathbf{u} \end{cases} \tag{2.1}$$

where $\mathbf{u}(\mathbf{x}, t)$ is the velocity field, $p(\mathbf{x}, t)$ is the pressure and $Re = Uh/\nu$ is the Reynolds number, defined with the maximum velocity of the laminar Poiseuille flow U, the half channel height h and the kinematic viscosity ν.

2.1.1 Perturbative Navier-Stokes equations

The instantaneous field is decomposed into the sum of a base flow $\mathbf{Q}_0 = [U_0, 0, 0, P_0]^T$ and a perturbation $\mathbf{q}' = [u', v', w', p']$, in the following way:

$$\mathbf{q}(x, y, z, t) = \mathbf{Q}_0(y) + \mathbf{q}'(x, y, z, t),$$

where the base state $\mathbf{Q}_0$ represents the time-independent part of the solution, i.e. the fixed point of the problem; while, $\mathbf{q}'$ is the unknown of the problem and it is time-dependent. The magnitude of the perturbation is considered of the same order of that of the base state, and for this reason, it is not possible to introduce the linear hypothesis and then, the perturbative Navier-Stokes equations in nonlinear formulation are obtained:

$$\begin{cases} \nabla \cdot \mathbf{u}' = 0 \\ \dfrac{\partial \mathbf{u}'}{\partial t} = -(\mathbf{u}' \cdot \nabla)\mathbf{u}' - (\mathbf{u}' \cdot \nabla)\mathbf{U}_0 - (\mathbf{U}_0 \cdot \nabla)\mathbf{u}' - \nabla p' + \dfrac{1}{Re}\nabla^2 \mathbf{u}' \end{cases} \tag{2.2}$$

with $U_0(y) = 1 - y^2$, the laminar Poiseuille velocity profile.

2.1.2 Perturbative Reynolds-Averaged Navier-Stokes

When studying the dynamics of perturbations characterising the turbulent flow, it can be appropriate to move the point of view to the vicinity of the turbulent mean flow. This is achieved by using a Reynolds decomposition approach similar to that used by Eitel-Amor *et al.* (2015) and Farano *et al.* (2017), where the flow vector is expressed as the sum of a mean flow $\overline{\mathbf{Q}} = [\overline{\mathbf{U}}, P]^T = [\overline{U}, 0, 0, \overline{P}]^T$ (where $\overline{\bullet}$ denotes long-time and space averaging along the streamwise and spanwise directions) and a fluctuation $\tilde{\mathbf{q}} = [\tilde{\mathbf{u}}, \tilde{p}]^T$, comprising the coherent and incoherent part of the perturbations of the mean flow. Time- and space- averaging along the wall-parallel directions the Navier-Stokes equations, and subtracting these averaged equations from the Navier-Stokes equations leads to the Perturbative Reynolds-Averaged Navier-Stokes (PRANS) equations, which describe in a statistical way the nonlinear evolution of fluctuations of the mean turbulent flow as:

$$\begin{cases} \nabla \cdot \tilde{\mathbf{u}} = 0 \\ \dfrac{\partial \tilde{\mathbf{u}}}{\partial t} = -(\tilde{\mathbf{u}} \cdot \nabla)\tilde{\mathbf{u}} - (\tilde{\mathbf{u}} \cdot \nabla)\overline{\mathbf{U}} - (\overline{\mathbf{U}} \cdot \nabla)\tilde{\mathbf{u}} - \tilde{\nabla} p + \dfrac{1}{Re}\nabla^2 \tilde{\mathbf{u}} + \nabla \cdot \overline{\tilde{\mathbf{u}}\tilde{\mathbf{u}}}, \end{cases} \tag{2.3}$$

where the term $\overline{\tilde{\mathbf{u}}\tilde{\mathbf{u}}}$ is the Reynolds stress tensor τ. Notice that steady solutions of the PRANS equations, as well as the mean flow itself, are sustained by the Reynolds stress term, which is in

turn sustained by the coherent and incoherent part of the fluctuations. The mean velocity profile for channel flow is well approximated by the analytical expression proposed by Reynolds & Tiederman (1967):

$$\frac{d\overline{U}^+}{dy} = -\frac{Re_\tau y}{\nu_T^+(y)}, \tag{2.4}$$

$\overline{U}^+ = \overline{U}/u_\tau$ and $Re_\tau = u_\tau h/\nu$ since it is the friction Reynolds number based on the friction velocity $u_\tau = \sqrt{\tau_w/\rho}$, where τ_w is the wall shear stress, and $\nu_T^+ = \nu_T/\nu$ is the ratio between the total viscosity $\nu_T = \nu + \nu_t$ and the kinematic viscosity ν, ν_t being the turbulent eddy viscosity. The derivation of this analytical formulation for the mean turbulent velocity profile is reported in the appendix B. The total eddy viscosity is modeled using the analytic approximation proposed by Cess (1958), as assumed in previous works (Reynolds & Hussain, 1972; del Álamo & Jiménez, 2006; Hwang, 2016).

Since this mean velocity profile is not a solution of the Navier-Stokes equations, in order to close the problem, the divergence of the Reynolds stress tensor τ in equation (2.3) needs to be modelled. A common way to write this term is using the Boussinesq's Eddy Viscosity hypothesis $\tau_{ij} = -\overline{\tilde{u}_i\tilde{u}_j} = \nu_t\overline{S}_{ij}$ (Pope, 2001), where $\overline{S}$ is the shear stress tensor. Considering a fully developed channel flow whose statistics are averaged in the streamwise and spanwise direction, the divergence of the Reynolds stress tensor has only two non-zero components, i.e., $d\tau_{12}(y)/dy$ and $d\tau_{22}(y)/dy$ (notice that the latter term cannot be incorporated in the pressure term since the other isotropic components have derivative equal to zero).

The former term is approximated using the above mentioned eddy viscosity hypothesis, while the latter is modelled by using the rescaling proposed by Chen *et al.* (2018), as:

$$\overline{\tilde{u}\tilde{v}} = -\nu_t\frac{d\overline{U}}{dy} \quad \text{and} \quad \overline{\tilde{v}\tilde{v}}^+ = \overline{\tilde{u}\tilde{v}}^+\left(\frac{l_{22}^+}{l_{12}^+}\right)^2, \tag{2.5}$$

l_{12}^+, l_{22}^+ being the Reynolds stress lengths defined as:

$$l_{i2}^+ = c_{i2}y^{+\frac{i+2}{2}}\left(1+\left(\frac{y^+}{y_{sub}^+}\right)^4\right)^{\frac{1}{8}}\left(1+\left(\frac{y^+}{y_{buf}^+}\right)^4\right)^{-\frac{1+i}{8}\frac{1-r^4}{4(1-r)}}\left(1+\left(\frac{r_{core\,i2}}{r}\right)^2\right)^{\frac{i}{4}}, \tag{2.6}$$

where $i = 1, 2$, $r = 1 - y$ is the distance from the centerline, $y_{sub}^+ = 9.7$ is the sub-layer thickness, $y_{buf}^+ = 41$ is the buffer layer thickness, $r_{core12} = 0.27$ and $r_{core22} = 0.3$ are the central core layers, and the parameters c_{12}, c_{22} are function of these quantities. The parameter c_{12} is define as:

$$c_{12} = \frac{l_0}{y_{sub}^{+3/2}Z_{core}}, \qquad l_0 = \frac{\kappa y_{sub}^{+2}}{y_{buf}^+}, \qquad Z_{core} = (1+r_{core}^2)^{1/4}.$$

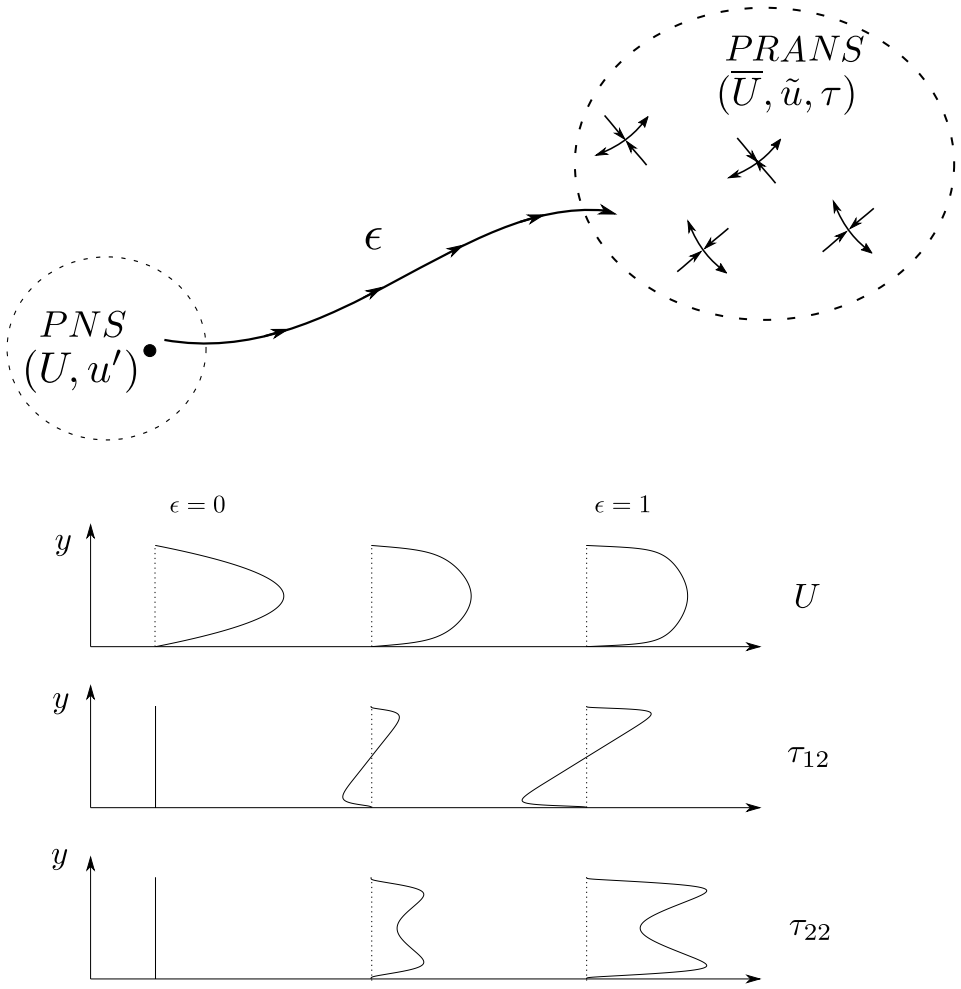

Figure 2.1: Schematic visualization of the continuation procedure from the Perturbative Navier-Stokes equations ($\epsilon = 0$) to the Perturbative Unsteady Reynolds-Averaged Navier-Stokes equations ($\epsilon = 1$).

with the parameter $\kappa = 0.45$. While, the parameter c_{22} is:

$$c_{22} = \frac{\kappa y_{sub}^{+1/2}}{\sqrt{y_{buf}^{+3}\left(1 + r_{22core}^2\right)}},$$

where the parameter $\kappa = 0.52$, but for moderate friction Reynolds number ($Re_\tau < 300$) $\kappa = 0.5$. This analytical formulation has been validated by comparing the mean turbulent flow and the Reynolds stress tensor components with those obtained by DNS at $Re = 3300$ ($Re_\tau = 180$) by Kim *et al.* (1987) and at $Re = 12450$ ($Re_\tau = 590$) by Moser *et al.* (1999) (see appendix C).

2.1.2.1 Continuation from the PNS to the PRANS framework

As discussed in the Context Chapter, a deeper understanding of the energetic bond connecting small- and large-scale structure in turbulent flows can be achieved by the computation of statistically-invariant coherent states which characterise the coherent part of the motion around the turbulent mean flow, without any filtering of small-scale structures. Towards this aim, we use the PRANS mathematical framework for the computation of travelling waves characterising the motion of turbulent fluctuations around the mean flow. In fact, this set of equations has been found efficient for characterising extreme events having an energy spectrum very similar to that of the fully turbulent flow Farano *et al.* (2017, 2018). Continuing in this statistical framework known invariant solutions of the Navier-Stokes equations at high friction Reynolds numbers, statistically-invariant motions containing both large- and small-scale coherent structures such as streaks and streamwise vortices, might be obtained, that represent the main motion of turbulent flows.

As sketched in figure 2.1, a homotopy procedure is used for continuously passing from equations (2.2) to (2.3), which have an almost identical structure, except for the steady flow used as reference and for the presence of the Reynolds stress tensor. Since these quantities depend directly on the turbulent eddy viscosity, the continuation is performed by continuously increasing this quantity from zero to its characteristic turbulent value expressed by the Cess model (Cess, 1958). Toward this purpose, we define an effective turbulent eddy viscosity, $\epsilon\nu_t$, where ϵ is a real positive number in the range $[0, 1]$, and ν_t is expressed as:

$$\nu_t = \frac{\nu}{2}\left\{1 + \left(\frac{\kappa^2 Re_\tau^2}{9}\right)\left(2\hat{\eta} - \hat{\eta}^2\right)^2\left(3 - 4\hat{\eta} + 2\hat{\eta}^2\right)^2\left\{1 - \exp\left[\frac{(|\hat{\eta} - 1| - 1)\, Re_\tau}{A}\right]\right\}^2\right\}^{\frac{1}{2}} - \frac{1}{2}. \quad (2.7)$$

with $\hat{\eta} = \eta + 1$ defined in the domain $[0, 2]$, $\kappa = 0.426$ and $A = 25.4$, as assumed in previous works (del Álamo & Jiménez, 2006; Pujals *et al.*, 2009; Hwang, 2016).

Continuation from the PNS to the PRANS equations is achieved by increasing the coefficient ϵ from 0 to 1, and using the effective turbulent eddy viscosity $\epsilon\nu_t$ in the analytical expression of the Reynolds stress tensor components τ_{11}, τ_{12} in equation (2.5) and in the mean flow profile in equation (2.4), where $\nu_T^+ = 1 + \epsilon\nu_t/\nu$.

The procedure consists in selecting a known travelling wave solution of the Navier-Stokes equations, subtracting the laminar flow solution for defining the corresponding perturbation, which is a travelling

wave solution of equations (2.2) , and continuing it in ϵ using the following equations:

$$\begin{cases} \nabla \cdot \tilde{\mathbf{u}} = 0 \\ -C\dfrac{\partial \tilde{\mathbf{u}}}{\partial x} = -(\tilde{\mathbf{u}} \cdot \nabla)\tilde{\mathbf{u}} - (\tilde{\mathbf{u}} \cdot \nabla)\overline{\mathbf{U}} - (\overline{\mathbf{U}} \cdot \nabla)\tilde{\mathbf{u}} - \tilde{\nabla} p + \dfrac{1}{Re}\nabla^2 \tilde{\mathbf{u}} - \nabla \cdot \epsilon \nu_t \overline{S}(\overline{\mathbf{U}}) \\ \overline{\mathbf{U}}(y) = \left[1 - \int \dfrac{Re_\tau^2 y}{Re(1+\epsilon\frac{\nu_t}{\nu})} dy, 0, 0\right]^T \end{cases} \tag{2.8}$$

where C is the phase velocity of the Galilean frame in which the solution is steady.

When $\epsilon = 0$, $Re_\tau^2 = 2Re$ and one recovers $\overline{U} = 1 - y^2 = U$, the Reynolds-stress tensor components being null. In this limit, the equations (2.8) coincide with the PNS equations (2.2) and consequently $\tilde{u}$ coincides with u'. When $\epsilon = 1$, one obtains the turbulent expression of ν_t given in equation (2.7), so that the turbulent mean velocity profile and the Reynolds stress tensor components in equations (2.5) are obtained. Notice that, similarly to a homotopy procedure, the solutions obtained for $\epsilon =]0, 1[$ have no physical sense. Moreover, for $\epsilon \neq 1$, $\tilde{\mathbf{u}}$ can have a non-zero mean, since $\overline{\mathbf{U}}$ represents the mean flow only in turbulent flow conditions, which are achieved only for $\epsilon = 1$. The whole procedure, which is sketched in figure 2.1, is implemented within the open-source software Channelflow (channelflow.ch) (Gibson *et al.*, 2021).

Continuation from the PNS to the PRANS equations is performed enforcing a constant volume flux and consequently fixing the bulk velocity $U_b = \int_{-1}^{1} U(y)dy$. Thus, while ϵ increases from 0 to 1, the friction Reynolds number grows from the laminar (Re_τ^L) towards the turbulent (Re_τ^T) value as:

$$Re_\tau = (1-\epsilon)Re_\tau^L + \epsilon Re_\tau^T = [(1-\epsilon)u_\tau^L + \epsilon u_\tau^T]\frac{h}{\nu}, \tag{2.9}$$

where $u_\tau^L = \sqrt{3U_b\nu/h}$ is the friction velocity of the laminar flow and u_τ^T is the friction velocity of the turbulent flow, which, using Dean's approximation for the skin friction in fully turbulent flow (Dean, 1978), can be expressed as:

$$u_\tau^T = \sqrt{\frac{0.073}{2}U_b^2\left(\frac{2U_b h}{\nu}\right)^{-0.025}}. \tag{2.10}$$

The results of this continuation procedure are provided in Chapter 6.

2.2 Optimization problem formulation

As mentioned in the previous Chapter, at subcritical values of the Reynolds number, the non-normality of the linearised Navier-Stokes equations can be responsible for linear transient amplification of the perturbations. In this case, perturbations having an initially small amplitude can reach in a

finite time a very large energy being able to trigger nonlinear effects bringing the flow to transition at Reynolds numbers lower than the critical one. In order to investigate the potential amplification that non normality can provide to the flow, one can search numerically for the perturbations causing the maximum possible transient energy amplification in a given finite time. These flow structures are called *optimal perturbations*, and can be recovered using a variational optimization in a linearized or nonlinear framework. The optimization problem consists of searching the perturbation $\mathbf{u}'$ that maximises the objective function, in this case, the energy gain, and verifies the following constraints:

- it must be a solution of the Navier-Stokes equations;
- it must be divergence free;
- it must have initial energy equal to a given one, E_0.

Then, the Lagrangian functional is defined as:

$$\begin{aligned}\mathcal{L}(u_i', p', u_i^\dagger, p^\dagger, u_i'(0), u_i'(T), \lambda) = \frac{E(T)}{E(0)} \\ - \int_0^T \int_V u_i^\dagger \left(\frac{\partial u_i'}{\partial t} + \frac{\partial (u_i' u_j')}{\partial x_j} + \frac{\partial (U_i u_j')}{\partial x_j} + \frac{\partial (u_i' U_j)}{\partial x_j} + \frac{\partial p}{\partial x_i} - \frac{1}{Re} \frac{\partial^2 u_i'}{\partial x_j} \right) dV dt \\ - \int_0^T \int_V p^\dagger \frac{\partial u_i'}{\partial x_i} dV dt - \lambda \left(\frac{E_0}{E(0)} - 1 \right).\end{aligned} \tag{2.11}$$

where:

$$E(T) = \frac{1}{2V} \int_V u_i'(T) u_i'(T) dV \quad and \quad E(0) = \frac{1}{2V} \int_V u_i'(0) u_i'(0) dV$$

are the energy at the target time T and the energy of the initial perturbation, respectively. Moreover, $u_i^\dagger$, $p^\dagger$ and λ are the Lagrangian multipliers (or adjoint variables).
To find the maximum of the optimization function $\mathcal{L}$, one has to impose that its variations with respect to every independent variable are equal to zero,

$$\delta \mathcal{L} = \left(\frac{\partial \mathcal{L}}{\partial u_i'}, \delta u_i' \right) + \left(\frac{\partial \mathcal{L}}{\partial u_i^\dagger}, \delta u_i^\dagger \right) + \left(\frac{\partial \mathcal{L}}{\partial \lambda} \right) \delta \lambda + \left(\frac{\partial \mathcal{L}}{\partial p^\dagger} \right) \delta p^\dagger + \left(\frac{\partial \mathcal{L}}{\partial p'} \right) \delta p' = 0,$$

giving the following equations that set up the optimization problem:

$$\frac{\partial \mathcal{L}}{\partial \lambda} := E(0) = E_0 \tag{2.12a}$$

$$\frac{\partial \mathcal{L}}{\partial u_i^\dagger} := \frac{\partial u_i'}{\partial t} + u_j' \frac{\partial u_i'}{\partial x_j} + u_j' \frac{\partial U_i}{\partial x_j} + U_j \frac{\partial u_i'}{\partial x_j} + \frac{\partial p}{\partial x_i} - \frac{1}{Re} \frac{\partial^2 u_i'}{\partial x_j} = 0 \tag{2.12b}$$

$$\frac{\partial \mathcal{L}}{\partial p^\dagger} := \frac{\partial u_i'}{\partial x_i} = 0 \tag{2.12c}$$

$$\frac{\partial \mathcal{L}}{\partial u_i'} := \frac{\partial u_i^\dagger}{\partial t} - u_j^\dagger \frac{\partial u_i'}{\partial x_j} + u_j' \frac{u_i^\dagger}{\partial x_j} - u_j^\dagger \frac{\partial U_i}{\partial x_j} + U_j \frac{\partial u_i^\dagger}{\partial x_j} + \frac{\partial p^\dagger}{\partial x_i} - \frac{1}{Re} \frac{\partial^2 u_i^\dagger}{\partial x_j} = 0 \tag{2.12d}$$

$$\frac{\partial \mathcal{L}}{\partial p'} := \frac{\partial u_i^\dagger}{\partial x_i} = 0 \tag{2.12e}$$

$$\frac{\partial \mathcal{L}}{\partial u_i'(T)} := u_i'(T) - u_i^\dagger(T) = 0 \tag{2.12f}$$

$$\frac{\partial \mathcal{L}}{\partial u_i'(0)} := u_i^\dagger(0) - \lambda u_i'(0) \tag{2.12g}$$

Equations (2.12a), (2.12b) and (2.12c) are the constraints imposed on the optimization problem and equations (2.12d) and (2.12e) are the adjoint Navier-Stokes equations. Furthermore, the equation (2.12f) represents the compatibility condition, while, the equation (2.12g) is the update condition.

2.2.1 Derivation of direct and adjoint equations

The equations (2.12a)-(2.12c) are obtained directly differentiating the Lagrangian functional (2.11) with respect to the Lagrangian multipliers.

For equation (2.12b):

$$\frac{\partial \mathcal{L}}{\partial u_k^\dagger} = 0 \Longrightarrow \int_0^T \int_V \frac{\partial u_i^\dagger}{\partial u_k^\dagger} \left(\frac{\partial u_i'}{\partial t} + U_j \frac{\partial u_i'}{\partial x_j} + u_j' \frac{\partial U_i}{\partial x_j} + \frac{\partial p'}{\partial x_i} - \frac{1}{Re} \frac{\partial^2 u_i'}{\partial x_j^2} + u_j' \frac{\partial u_i'}{\partial x_j} \right) dV dt = 0,$$

$$\int_0^T \int_V \delta_{ik} \left(\frac{\partial u_i'}{\partial t} + U_j \frac{\partial u_i'}{\partial x_j} + u_j' \frac{\partial U_i}{\partial x_j} + \frac{\partial p'}{\partial x_i} - \frac{1}{Re} \frac{\partial^2 u_i'}{\partial x_j^2} + u_j' \frac{\partial u_i'}{\partial x_j} \right) dV dt = 0.$$

There is not dependence between direct variables and adjoint variables, that is $\partial q_i / \partial q_k^\dagger = 0$ and $\partial q_i^\dagger / \partial q_k = 0$, too. $\delta_{ik} = \partial u_i^\dagger / \partial u_k^\dagger$ is the Knoneker delta and remembering its propriety that $q_i \delta_{ik} = q_k$, one has

$$\int_0^T \int_V \left(\frac{\partial (u_i' \delta_{ik})}{\partial t} + U_j \frac{\partial (u_i' \delta_{ik})}{\partial x_j} + u_j' \frac{\partial (U_i \delta_{ik})}{\partial x_j} + \frac{\partial p'}{\partial x_i} \delta_{ik} - \frac{1}{Re} \frac{\partial^2 (u_i' \delta_{ik})}{\partial x_j^2} + u_j' \frac{\partial (u_i' \delta_{ik})}{\partial x_j} \right) dV dt = 0,$$

$$\int_0^T \int_V \left(\frac{\partial u_k'}{\partial t} + U_j \frac{\partial u_k'}{\partial x_j} + u_j' \frac{\partial U_k}{\partial x_j} + \frac{\partial p'}{\partial x_k} - \frac{1}{Re} \frac{\partial^2 u_k'}{\partial x_j^2} + u_j' \frac{\partial u_k'}{\partial x_j} \right) dV dt = 0.$$

Imposing that the integral has to be null, being the integrated functional equal to zero in all the domain and at each time step, the equation (2.12b) is obtained.
In the same way, it is obtained the equation (2.12c):

$$\frac{\partial \mathcal{L}}{\partial p^\dagger} = 0 \Longrightarrow -\int_0^T \int_V \frac{\partial u_i}{\partial x_i} dV dt = 0 \Longrightarrow \frac{\partial u_i}{\partial x_i} = 0.$$

To obtain the equations (2.12d)-(2.12e) one has to integrate by part each term of the Lagrangian functional (2.11).

$$\mathcal{L}(u_i', p', u_i^\dagger, p^\dagger, u_i'(0), u_i'(T), \lambda) = \frac{E(T)}{E(0)} +$$
$$-\int_0^T \int_V \Bigg(\underbrace{u_i^\dagger \frac{\partial u_i'}{\partial t}}_{1} + \underbrace{u_i^\dagger \frac{\partial (u_i' U_j)}{\partial x_j}}_{2} + \underbrace{u_i^\dagger \frac{\partial (U_i u_j')}{\partial x_j}}_{3} + \underbrace{u_i^\dagger \frac{\partial p'}{\partial x_i}}_{4} - \underbrace{\frac{1}{Re} u_i^\dagger \frac{\partial^2 u_i'}{\partial x_j^2}}_{5} + \underbrace{u_i^\dagger \frac{\partial (u_i' u_j')}{\partial x_j}}_{6} \Bigg) dV dt +$$
$$-\int_0^T \int_V \underbrace{p^\dagger \frac{\partial u_i'}{\partial x_i}}_{7} dV dt - \lambda \left(\frac{E_0}{E(0)} - 1 \right).$$

Then, integrating by part each term:

$$1: \int_0^T \int_V u_i^\dagger \frac{\partial u_i'}{\partial t} dV dt = \cancel{\int_0^T \left[u_i^\dagger u_i' \right]_{\partial V} dt} - \int_0^T \int_V u_i' \frac{\partial u_i^\dagger}{\partial t} dV dt = -\int_0^T \int_V u_i' \frac{\partial u_i^\dagger}{\partial t} dV dt$$

where the first integral on the RHS is null due to the boundary conditions imposition on the direct and adjoint perturbation, i.e. the direct and adjoint perturbations are equal to zero on the domain boundaries ($u_i' = u_i^\dagger = 0$);

$$2: \int_0^T \int_V u_i^\dagger \frac{\partial (u_i' U_j)}{\partial x_j} dV dt = \cancel{\int_0^T \left[u_i^\dagger u_i' U_j \right]_{\partial V} dt} - \int_0^T \int_V u_i' U_j \frac{\partial u_i^\dagger}{\partial x_j} dV dt = -\int_0^T \int_V u_i' U_j \frac{\partial u_i^\dagger}{\partial x_j} dV dt;$$

$$3: \int_0^T \int_V u_i^\dagger \frac{\partial (U_i u_j')}{\partial x_j} dV dt = \int_0^T \int_V u_i^\dagger \left(u_j' \frac{\partial U_i}{\partial x_j} + \cancel{U_i \frac{\partial u_j'}{\partial x_j}} \right) dV dt = \int_0^T \int_V u_i^\dagger u_j' \frac{\partial U_i}{\partial x_j} dV dt,$$

with $\partial u_j'/\partial x_j = 0$ due to the mass conservation;

$$4: \int_0^T \int_V u_i^\dagger \frac{\partial p'}{\partial x_i} dV dt = \cancel{\int_0^T \left[u_i^\dagger p' \right]_{\partial V} dt} - \int_0^T \int_V p' \frac{\partial u_i^\dagger}{\partial x_i} dV dt = -\int_0^T \int_V p' \frac{\partial u_i^\dagger}{\partial x_i} dV dt;$$

$$5: \int_0^T \int_V \frac{1}{Re} u_i^\dagger \frac{\partial^2 u_i'}{\partial x_j^2} dV dt = \cancel{\int_0^T \left[\frac{1}{Re} u_i^\dagger \frac{\partial u_i'}{\partial x_j} \right]_{\partial V} dt} - \int_0^T \int_V \frac{1}{Re} \frac{\partial u_i^\dagger}{\partial x_j} \frac{\partial u_i'}{\partial x_j} dV dt =$$
$$= -\int_0^T \int_V \frac{1}{Re} \frac{\partial u_i^\dagger}{\partial x_j} \frac{\partial u_i'}{\partial x_j} dV dt = \cancel{-\int_0^T \left[\frac{1}{Re} \frac{\partial u_i^\dagger}{\partial x_j} u_i' \right]_{\partial V} dt} + \int_0^T \int_V \frac{1}{Re} u_i' \frac{\partial^2 u_i^\dagger}{\partial x_j^2} dV dt =$$
$$= \int_0^T \int_V \frac{1}{Re} u_i' \frac{\partial^2 u_i^\dagger}{\partial x_j^2} dV dt;$$

$$6: \int_0^T \int_V u_i^\dagger \frac{\partial (u_i' u_j')}{\partial x_j} dV dt = \int_0^T \int_V u_i^\dagger \left(u_j' \frac{\partial u_i'}{\partial x_j} + u_i' \frac{\partial u_j'}{\partial x_j} \right) dV dt = \int_0^T \int_V u_i^\dagger u_j' \frac{\partial u_i'}{\partial x_j} dV dt;$$

$$7: \int_0^T \int_V p^\dagger \frac{\partial u_i'}{\partial x_i} dV dt = \int_0^T \left[p^\dagger u_i' \right]_{\partial V} dt - \int_0^T \int_V u_i' \frac{\partial p^\dagger}{\partial x_i} dV dt = - \int_0^T \int_V u_i' \frac{\partial p^\dagger}{\partial x_i} dV dt.$$

After integration by part, the Lagrangian functional becomes:

$$\mathcal{L}(u_i', p', u_i^\dagger, p^\dagger, u_i'(0), u_i'(T), \lambda) = \frac{E(T)}{E(0)} +$$
$$+ \int_0^T \int_V \left(u_i' \frac{\partial u_i^\dagger}{\partial t} + u_i' U_j \frac{\partial u_i^\dagger}{\partial x_j} - u_i^\dagger u_j' \frac{\partial U_i}{\partial x_j} + p' \frac{\partial u_i^\dagger}{\partial x_i} - \frac{1}{Re} u_i' \frac{\partial^2 u_i^\dagger}{\partial x_j^2} - u_i^\dagger u_j' \frac{\partial u_i'}{\partial x_j} \right) dV dt +$$
$$+ \int_0^T \int_V u_i' \frac{\partial p^\dagger}{\partial x_i} dV dt - \lambda \left(E_0 - E(0) \right)$$

Deriving this equation with respect to p', one obtains the equation (2.12e):

$$\frac{\partial \mathcal{L}}{\partial p'} = 0 \Longrightarrow \int_0^T \int_V \frac{\partial u_i^\dagger}{\partial x_i} dV dt = 0 \Longrightarrow \frac{\partial u_i^\dagger}{\partial x_i} = 0.$$

Furthermore, deriving the last expression of the Lagrangian functional with respect to the variable u_k', one has:

$$\frac{\partial \mathcal{L}}{\partial u_k'} = 0 \Longrightarrow \frac{\partial}{\partial u_k'} \int_0^T \int_V \left(u_i' \frac{\partial u_i^\dagger}{\partial t} + u_i' U_j \frac{\partial u_i^\dagger}{\partial x_j} - u_i^\dagger u_j' \frac{\partial U_i}{\partial x_j} - \frac{1}{Re} u_i' \frac{\partial^2 u_i^\dagger}{\partial x_j^2} - u_i^\dagger u_j' \frac{\partial u_i'}{\partial x_j} + u_i' \frac{\partial p^\dagger}{\partial x_i} \right) dV dt = 0$$

$$\int_0^T \int_V \left(\frac{\partial u_i'}{\partial u_k'} \frac{\partial u_i^\dagger}{\partial t} + U_j \frac{\partial u_i'}{\partial u_k'} \frac{\partial u_i^\dagger}{\partial x_j} - u_i^\dagger \frac{\partial u_j'}{\partial u_k'} \frac{\partial U_i}{\partial x_j} - \frac{1}{Re} \frac{\partial u_i'}{\partial u_k'} \frac{\partial^2 u_i^\dagger}{\partial x_j^2} - u_i^\dagger \frac{\partial u_j'}{\partial u_k'} \frac{\partial u_i'}{\partial x_j} - u_i^\dagger u_j' \frac{\partial}{\partial u_k'} \left(\frac{\partial u_i'}{\partial x_j} \right) + \frac{\partial u_i'}{\partial u_k'} \frac{\partial p^\dagger}{\partial x_i} \right) dV dt = 0$$

$$\int_0^T \int_V \left(\delta_{ik} \frac{\partial u_i^\dagger}{\partial t} + U_j \delta_{ik} \frac{\partial u_i^\dagger}{\partial x_j} - u_i^\dagger \delta_{jk} \frac{\partial U_i}{\partial x_j} - \frac{1}{Re} \delta_{ik} \frac{\partial^2 u_i^\dagger}{\partial x_j^2} - u_i^\dagger \delta_{jk} \frac{\partial u_i'}{\partial x_j} - u_i^\dagger u_j' \frac{\partial}{\partial u_k'} \left(\frac{\partial u_i'}{\partial x_j} \right) + \delta_{ik} \frac{\partial p^\dagger}{\partial x_i} \right) dV dt = 0$$

$$\int_0^T \int_V \left(\frac{\partial (u_i^\dagger \delta_{ik})}{\partial t} + U_j \frac{\partial (u_i^\dagger \delta_{ik})}{\partial x_j} - u_i^\dagger \frac{\partial U_i}{\partial x_j} \delta_{jk} - \frac{1}{Re} \frac{\partial^2 (u_i^\dagger \delta_{ik})}{\partial x_j^2} - u_i^\dagger \frac{\partial u_i'}{\partial x_j} \delta_{jk} - u_i^\dagger u_j' \frac{\partial}{\partial u_k'} \left(\frac{\partial u_i'}{\partial x_j} \right) + \frac{\partial p^\dagger}{\partial x_i} \delta_{ik} \right) dV dt = 0$$

$$\int_0^T \int_V \left(\frac{\partial u_k^\dagger}{\partial t} + U_j \frac{\partial u_k^\dagger}{\partial x_j} - u_i^\dagger \frac{\partial U_i}{\partial x_k} - \frac{1}{Re} \frac{\partial^2 u_k^\dagger}{\partial x_j^2} - u_i^\dagger \frac{\partial u_i'}{\partial x_k} \underbrace{- u_i^\dagger u_j' \frac{\partial}{\partial u_k'} \left(\frac{\partial u_i'}{\partial x_j} \right)}_{I} + \frac{\partial p^\dagger}{\partial x_k} \right) dV dt = 0.$$

Term I needs further development.

$$I: \int_0^T \int_V u_i^\dagger u_j' \frac{\partial}{\partial u_k'} \left(\frac{\partial u_i'}{\partial x_j} \right) dV dt = \int_0^T \int_V \left[u_i^\dagger u_j' \frac{\partial u_i'}{\partial u_k'} \right]_{\partial V} dV dt - \int_0^T \int_V \frac{\partial u_i'}{\partial u_k'} \frac{\partial (u_i^\dagger u_j')}{\partial x_j} dV dt =$$
$$= - \int_0^T \int_V \delta_{ik} \frac{\partial (u_i^\dagger u_j')}{\partial x_j} dV dt = - \int_0^T \int_V \frac{\partial (u_i^\dagger \delta_{ik} u_j')}{\partial x_j} = - \int_0^T \int_V \frac{\partial (u_k^\dagger u_j')}{\partial x_j} dV dt.$$

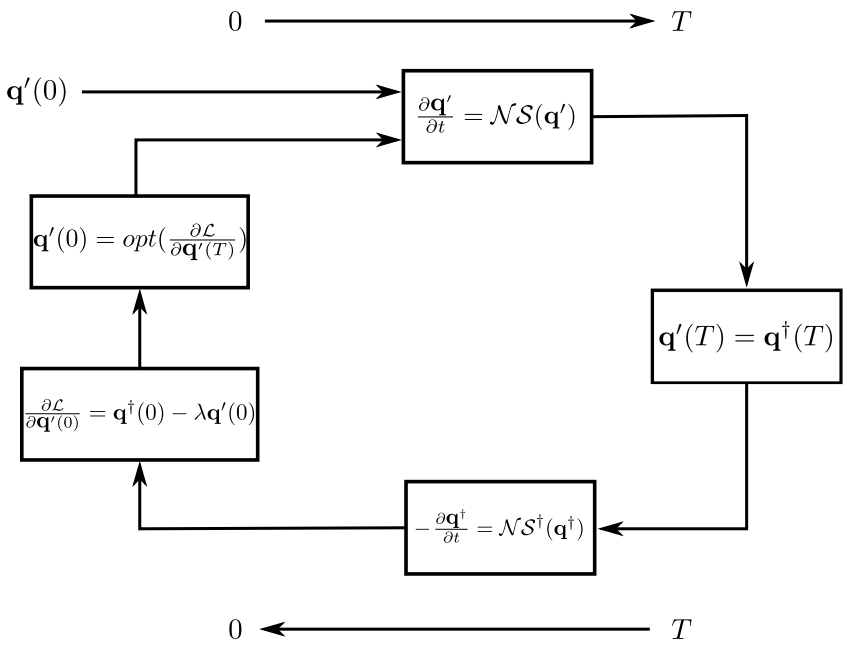

Figure 2.2: Direct-adjoint looping alghoritm scheme.

In this way, the last equation becomes:

$$\int_0^T \int_V \left(\frac{\partial u_k^\dagger}{\partial t} + \frac{\partial (U_j u_k^\dagger)}{\partial x_j} - u_i^\dagger \frac{\partial U_i}{\partial x_k} - \frac{1}{Re} \frac{\partial^2 u_k^\dagger}{\partial x_j^2} - u_i^\dagger \frac{\partial u_i'}{\partial x_k} + \frac{\partial (u_k^\dagger u_j')}{\partial x_j} + \frac{\partial p^\dagger}{\partial x_k} \right) dV dt = 0.$$

Imposing that the integral has to vanish, finally one gets the adjoint equations (2.12d)

$$\frac{\partial u_k^\dagger}{\partial t} + \frac{\partial (U_j u_k^\dagger)}{\partial x_j} - u_i^\dagger \frac{\partial U_i}{\partial x_k} - \frac{1}{Re} \frac{\partial^2 u_k^\dagger}{\partial x_j^2} - u_i^\dagger \frac{\partial u_i'}{\partial x_k} + \frac{\partial (u_k^\dagger u_j')}{\partial x_j} + \frac{\partial p^\dagger}{\partial x_k} = 0.$$

2.2.2 Direct-adjoint algorithm

The optimization algorithm is solved using a direct-adjoint looping algorithm sketched in figure 2.2. During one cycle, the direct Navier-Stokes equations are integrated in time from 0 to a given target time T using a given initial condition. At time t = T, a terminal condition for the direct problem is converted in a terminal condition for the adjoint equations via the compatibility equation (2.12f). The adjoint equations are integrated backward in time and a new initial condition is computed to restart the whole optimization problem.

The initial condition update is carried out with a gradient rotation algorithm as previously done by Foures *et al.* (2013); Farano *et al.* (2016, 2017). Taking into account the gradient in the equation

(2.12g):

$$\frac{\partial \mathcal{L}}{\partial u_i'(0)} := u_i'(0) - \lambda^{-1} u_j^\dagger(0). \tag{2.13}$$

As can be seen, the current expression of the gradient depends on the Lagrange multiplier λ whose value is unknown at present. One can however write down a mathematical expression of this gradient orthogonalised with respect to u_i':

$$\frac{\partial \mathcal{L}}{\partial u_i'(0)}^{\perp} = \frac{\partial \mathcal{L}}{\partial u_i'(0)} - \frac{\langle \frac{\partial \mathcal{L}}{\partial u_i'(0)}, u_i' \rangle}{\langle u_i', u_i' \rangle} u_i'. \tag{2.14}$$

Introducing the analytical expression of the gradient (2.12g), the orthogonalised gradient can be expressed as:

$$\begin{aligned} \frac{\partial \mathcal{L}}{\partial u_i'(0)}^{\perp} &= (u_i^\dagger - \lambda u_i') - \frac{\langle (u_i^\dagger - \lambda u_i'), u_i' \rangle}{\langle u_i', u_i' \rangle} u_i' \\ &= u_i^\dagger - \lambda u_i' - \frac{\langle u_i^\dagger, u_i' \rangle}{\langle u_i', u_i' \rangle} u_i' + \lambda \frac{\langle u_i', u_i' \rangle}{\langle u_i', u_i' \rangle} u_i'. \end{aligned} \tag{2.15}$$

After simplifications, the orthogonalised gradient finally reads:

$$\frac{\partial \mathcal{L}}{\partial u_i'(0)}^{\perp} = u_i^\dagger - \frac{\langle u_i^\dagger, u_i' \rangle}{\langle u_i', u_i' \rangle} u_i'. \tag{2.16}$$

Then, the expression of the orthogonalised gradient (2.16) depends only on the direct variable u_i' and the adjoint $u_i^\dagger$, while the dependence on the unknown Lagrange multiplier λ has been completely removed from the optimisation problem. Normalising this new gradient such that:

$$\mathbf{G}^n = \sqrt{\frac{E_0}{\langle \frac{\partial \mathcal{L}}{\partial u_i'(0)}^{\perp}, \frac{\partial \mathcal{L}}{\partial u_i'(0)}^{\perp} \rangle}} \frac{\partial \mathcal{L}}{\partial u_i'(0)}^{\perp} \tag{2.17}$$

now allows us to look for the update $u_i'^{n+1}$ as a simple linear combination of $u_i'^n$ and $\mathbf{G}^n$ given by:

$$u_i'^{n+1} = \cos(\alpha) u_i'^n + \sin(\alpha) \mathbf{G}^n. \tag{2.18}$$

Since $u_i'^n$ and $\mathbf{G}^n$ form an orthonormal set of vectors, this update $u_i'^{n+1}$ now fulfills, directly by construction, the constraint on the initial energy (2.12a).

Due to the presence of several sub-optima in the nonlinear regime, to ensure the convergence of the method to the maximum of the functional, a check needs to be put on the value of the angle α used for the update of the solution. In this work, every calculation has been started with $\alpha = \pi/4$. However, if the gain $\lambda_{n+1}(T)$ computed at iteration $n+1^{th}$ is smaller than the gain $\lambda_n(T)$ at the previous one,

then the update u_i^{n+1} is re-updated with a different value of α, typically $\alpha = \alpha/2$, until the condition $\lambda_{n+1}(T) > \lambda_n(T)$ is achieved.
In the appendix A, some validations of the nonlinear optimization are shown.

2.2.3 Checkpointing technique

In the nonlinear form of the adjoint equations (2.12d), the term $u'_j \partial u_i^\dagger / \partial x_j$ establishes a coupling between direct and adjoint variables. This term in the nonlinear optimization framework makes difficult the numerical resolution of the problem in terms of memory, especially for larger domains and for optimization at high target times, since it is required the storage of the direct flow field u'_j at each time step. To reduce the storage required for the computation, a checkpointing technique is used, similar to that used by Griewank & Walther (2000) and Hinze *et al.* (2006).
In figure 2.3 the checkpointing technique scheme is reported, in which with red cross symbols are specified the N checkpoint steps chosen, so that the target time is divided into N steps. The checkpointing technique consists in the following steps:

1. the direct equations are solved from 0 to T_{N-1} and the direct flow fields are stored at each N checkpoint steps (T_1,T_2...,T_N);

2. the direct equations are solved in the last step (from T_{N-1} to T_N) storing the direct solutions at each time steps; thus, the adjoint equations are solved backward in time;

3. the previous procedure is repeated for all the checkpoint steps advancing from the end up to $t = 0$.

Therefore, this technique reduces the memory storage, resulting in an increase in terms of computational cost due to the repetition of the resolution of the direct problem.

2.3 *Channelflow* code

In this work, the *Channelflow* (channelflow.ch) (Gibson *et al.* (2021)) open source code developed initially by J.F Gibson (Gibson et al. (2008)) is used for all the calculations.
In $Channelflow$ code are implemented the perturbative Navier-Stokes equations (2.2) for a known laminar velocity profile $\mathbf{U} = [U(y), 0, 0]$ associated to the base pressure gradient dP/dx.

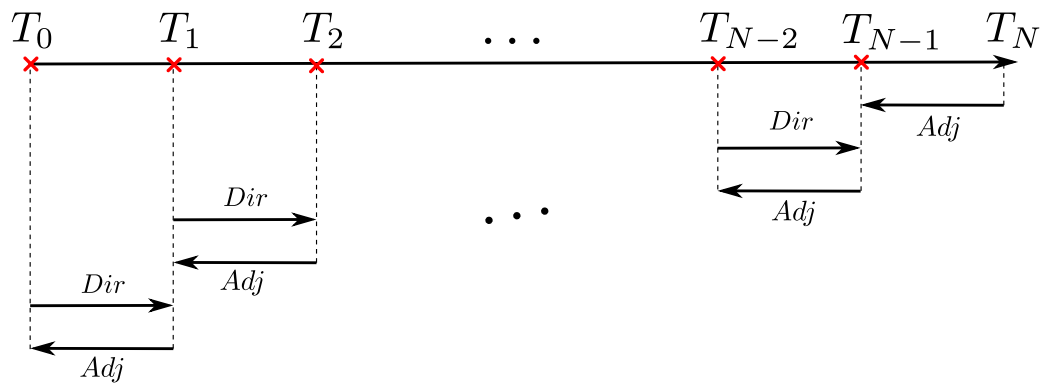

Figure 2.3: Checkpointing technique scheme. The red "X" symbols indicate the chosen checkpointing times.

For the equations is used a spectral discretisation in spatial directions (Fourier × Chebyshev × Fourier), then the velocity vector presents the following mathematical form:

$$\mathbf{u}(\mathbf{x}) = \sum_{k_x=-N_x/2+1}^{N_x/2} \sum_{n_y=0}^{N_y-1} \sum_{k_z=-N_z/2+1}^{N_z/2} \hat{\hat{\mathbf{u}}}_{k_x,n_y,k_z} \overline{T}_{n_y}(y) e^{2\pi i(k_x x/L_x + k_z z/L_z)} \tag{2.19}$$

where $\mathbf{x} = (x, y, z)$ and $\overline{T}_n$ is the nth Chebyshev polynomial. With (N_x, N_y, N_z) are indicating the grid points in the domain $L_x \times L_y \times L_z$. A third-order semi-implicit backward difference scheme is used for the time integration. An influence matrix method with Chebyshev tau correction was used to enforce no-slip boundary condition at the walls.

Channelflow has its own subroutines to perform the edge tracking and the parameter continuation. In the appendix D, some test cases performed with *Channelflow* code are shown.

2.3.1 Edge-tracking

The edge tracking technique implemented in *Channelflow* code requires a suitable initial condition $\mathbf{u}'_0$ that is premultiplied by a parameter λ

$$\mathbf{u}_0 = \lambda \mathbf{u}'_0.$$

Furthermore, it is necessary to choose two values λ_L, for which the initial perturbation decays to the laminar solution, and λ_T, for which the solution evolves to the chaotic state.

This edge-tracking technique consists of three steps: first a bisection step, then the solution found with the bisection is advanced in time and at the end, a new solution is chosen for the bisection. In

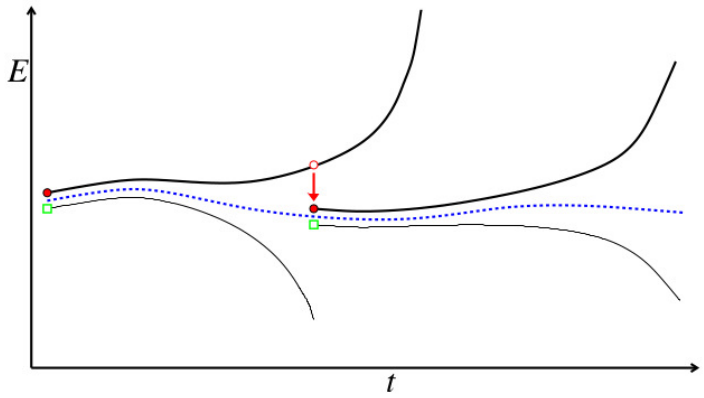

Figure 2.4: Schematic visualization of the initial condition approximation method. Initially, a pair of initial conditions are chosen: red filled circle on the turbulent side, green open box on the opposite laminar side. After a certain time, the approximation is refined by choosing a new pair of approximating trajectories. The new pair of initial conditions is constructed by taking the state of the previous trajectory that finally turns turbulent (red open circle) and rescaling its amplitude (From Schneider (2007)).

the first step, a standard bisection is performed within the imposed initial solutions, $\mathbf{u}_L = \lambda_L \mathbf{u}'_0$ for the laminar initial condition and $\mathbf{u}_T = \lambda_T \mathbf{u}'_0$ for the turbulent ones. Then, at each bisection step, it is verified if the parameter $\lambda = (\lambda_L + \lambda_T)/2$ corresponds to a solution in the laminar or turbulent basin of attraction. In figure 2.4 a scheme of this bisection method is presented. The bisection is stopped when the distance between $\mathbf{u}_L$ and $\mathbf{u}_T$ is smaller than a threshold ϵ_B:

$$\frac{\|\mathbf{u}_T - \mathbf{u}_L\|}{\|\mathbf{u}_T\| + \|\mathbf{u}_L\|} < \epsilon_B. \tag{2.20}$$

Tolerance as low as $\epsilon_B = 10^{-10}$ can be used to found the solution that lie on the edge of chaos for a long time. In the figure 2.5, the energy traces of trajectories bounding the edge of chaos are shown.

In the second step, the solution found with the bisection is advanced in time until it is on the edge. If during this second phase, the perturbation decays to the laminar state or diverges to the turbulent attractor, it is 'pushed back' into the edge by rescaling its amplitude for initializing the next bisection step. In the third step, new values for λ_L and λ_T are chosen and the edge tracking method is repeated until the initial solution stays in the edge for the chosen target time.

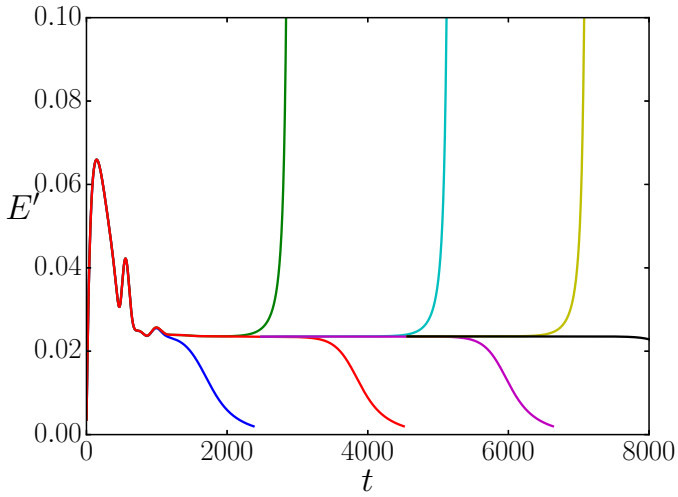

Figure 2.5: Energy traces of trajectories bounding the edge of chaos. The lines show initial conditions that swing up to the turbulent flow and belong to the upper end of the intervals. And also decaying trajectories from the lower end of the interval are presented. The bisection is stopped when the initial relative difference in amplitude of the solution is about 10^{-10}.

2.3.2 Parameter continuation

Continuation methods are used to determine the evolution of a solution of a dynamical system, such as

$$\dot{\mathbf{x}} = \mathbf{f}(\mathbf{x}, \mu), \tag{2.21}$$

subject to the variation of various parameters like the domain size, the Reynolds number etc., denoted by a certain parameter μ.

Let $\mathbf{x} = \mathbf{x}_0$ be the solution of a nonlinear function

$$\mathbf{f}(\mathbf{x}, \mu) = 0, \tag{2.22}$$

when $\mu = \mu_0$.

Then, considering the implicit function theorem, if the Jacobian matrix $\mathcal{J}(\mathbf{x}_0, \mu_0)$ is not singular and the equation (2.22) is satisfied, a solution around the point $(\mathbf{x}_0, \mu_0)$ can be found, such that, for each μ, the system (2.22) presents a unique solution $\mathbf{x}$. This solution can be found by differentiating implicitly the dynamical system (2.21):

$$\mathcal{J}(\mathbf{x}^i, \lambda) \cdot \partial\mathbf{x}^i = -\mathbf{f}(\mathbf{x}^i, \mu) \qquad \text{with} \quad \mathbf{x}^{i+1} = \mathbf{x}^i + \partial\mathbf{x}^i.$$

However, since the Jacobian matrix is singular in the bifurcation points, the implicit function theorem fails for these points, and it is available only away from turning points.
In *Channelflow* code two different continuation methods are implemented: the first is a predictor-corrector method with a quadratic extrapolation step, which may fail around saddle node bifurcations. The second one is an arclength continuation that allows better continuation around saddle nodes and turning points.

2.3.2.1 Quadratic predictor-corrector method

With this method, instead of parametrizing the solution of the nonlinear function by the parameter μ, both the solution $\mathbf{x}$ and the parameter μ are parametrized as a function of an arclength parameter s:

$$\mathbf{f}(\mathbf{x}(s), \mu(s)) = 0.$$

First, it is necessary to advance the solution in arclength parameter space from s_0 to s_1, then the arclength condition is introduced

$$\left\| \frac{\partial \mathbf{x}}{\partial s} \right\|^2 + \left\| \frac{\partial \mu}{\partial s} \right\|^2 = 1,$$

to compute a small increment $ds = \sqrt{\|d\mathbf{x}\|^2 + \|d\mu\|^2}$ along the solution curve. Then, the new arclength parameter is computed $s_{new} = s_0 + ds$.
To use the quadratic predictor, three initial solutions are necessary to start the continuation. These three initial solutions are obtained for three different but close values of the parameter μ. At this point, Neville's algorithm is used for polynomial interpolation, which, with three different initial guesses, gives a unique polynomial of degree two. This polynomial can interpolate or extrapolate the solution along the solution branch. Then, the next point $\mathbf{x}_{new}$ in the solution branch with the corresponding parameter μ_{new} are computed as follows

$$\begin{aligned} \mathbf{x}_{new} &= \frac{\mathbf{x}_0(s_{new} - s_1) - \mathbf{x}_1(s_{new} - s_0)}{s_0 - s_1} \\ \mu_{new} &= \frac{\mu_0(s_{new} - s_1) - \mu_1(s_{new} - s_0)}{s_0 - s_1} \end{aligned} \tag{2.23}$$

Once the predictor step is completed, the correction phase is performed with the Newton-Krylov subspace method. This method does not calculate the tangent vector along the branch and if started

at some distance from the singular point it can easily pass through the singular points to capture other branches.

2.3.2.2 Arclength continuation

The arclength continuation method is based on the pseudo-arclength continuation method (Keller, 1987; Nayfeh & Balachandran, 2008), and as for the previous continuation method, the solution $\mathbf{x}$ and the parameter μ are both function of the arclength parameter s. Then, differentiation of the nonlinear function $\mathbf{f}(\mathbf{x}, \mu) = 0$ with respect of s gives:

$$\frac{\partial \mathbf{f}}{\partial \mathbf{x}} \frac{\partial \mathbf{x}}{\partial s} + \frac{\partial \mathbf{f}}{\partial \mu} \frac{\partial \mu}{\partial s} = 0.$$

Also in this case, it is necessary to introduce a constraint for the arclength parameter as

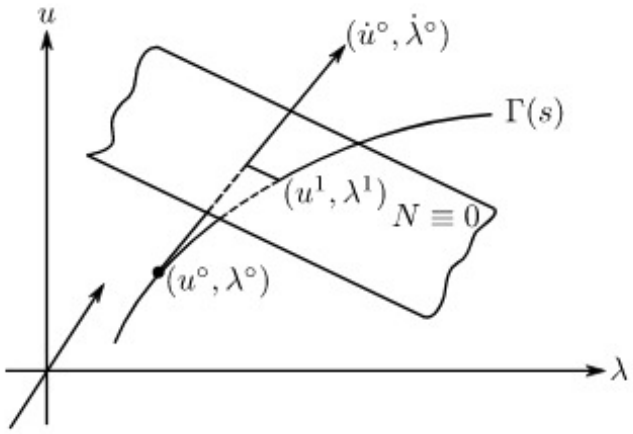

Figure 2.6: Illustration for pseudo-arclength continuation scheme. $\mathcal{N}$ plane intersect the continuation cuve $\Gamma(s)$ in the point (u^1, λ^1) and is perpendicular to the tangent $(\dot{u}^0, \dot{\lambda}^0)$ (From Keller (1987)).

$$\left\| \frac{\partial \mathbf{x}}{\partial s} \right\|^2 + \left\| \frac{\partial \mu}{\partial s} \right\|^2 = 1,$$

which when linearized brings to the equation of a plane

$$\mathcal{N} \equiv (\mathbf{x}(s) - \mathbf{x}(s_0)) \cdot \dot{\mathbf{x}}(s_0) + (\mu(s) - \mu(s_0)) \cdot \dot{\mu}(s_0) - \Delta s = 0.$$

This formulation implies that the $\mathcal{N}$ plane is perpendicular to the tangent $(\dot{\mathbf{x}}(s_0), \dot{\mu}(s_0))$ at a distance Δs from the solution $(\mathbf{x}(s_0), \mu(s_0))$. Moreover, the plane $\mathcal{N}$ intersects the continuation curve $\mathcal{C}(s)$ if it presents a not large curvature and the new arclength parameter does not differ enough to the previous.

In figure 2.6 is reported a sketch of the arclength continuation scheme.

At each iteration, with the Newton's method the following linear system is solved:

$$[h] \begin{pmatrix} \mathbf{f_x} & \mathbf{f}_\mu \\ \dot{\mathbf{x}}(s_0) & \dot{\mu}(s_0) \end{pmatrix} \begin{pmatrix} \Delta\mathbf{x} \\ \Delta\mu \end{pmatrix} = - \begin{pmatrix} \mathbf{f}(\mathbf{x}, \mu) \\ (\mathbf{x}(s) - \mathbf{x}(s_0)) \cdot \dot{\mathbf{x}}(s_0) + (\mu(s) - \mu(s_0)) \cdot \dot{\mu}(s_0) - \Delta s \end{pmatrix}.$$

In this case, the continuation parameter μ is added to the vector of unknowns. Then, when the convergence is reached with Newton's method, the new solution $\mathbf{x}_{new}$, with the corresponding continuation parameter μ_{new} are found on the branch. After $(\mathbf{x}, \mu)$ is determined on the branch, we move on to determine another point on the branch. The step size $\Delta s = \sqrt{\|d\mathbf{x}\|^2 + \|d\mu\|^2}$ can be reduced if the convergence is slow and increased if the convergence is rapid.

This method is found to be the most effective, as it manages to pass smoothly through the singular points.

Chapter 3

Minimal seeds for turbulent bands in channel flow

Contents

As introduced previously, two methodologies are used in the literature to trigger turbulence in the form of laminar-turbulent bands. The first one consists in starting from a statistically-steady turbulent flow in the whole domain and decreasing the Reynolds number to a value at which turbulent bands are observed (Tsukahara *et al.*, 2005; Kashyap *et al.*, 2020). Conversely, the second strategy consists in perturbing the field with a suitable localised perturbation with enough energy to trigger oblique turbulent bands (Duguet *et al.*, 2010; Tao & Xiong, 2013; Xiong *et al.*, 2015). Thus, for this second methodology the amplitude, the shape, and the localization of the perturbation should be carefully chosen.

In this chapter we are looking for the minimal seed able to generate turbulent bands in channel flow, i.e. we seek for the nonlinear optimal perturbation with the minimal initial energy able to trigger turbulence. The methodology to find these perturbations is based on the nonlinear variational optimization coupled with the energy bisection. The nonlinear optimisation is carried out in large domains allowing the creation of laminar-turbulent patterns such as oblique stripes. The kinetic energy is used

as the objective function of the nonlinear optimization, which appears an appropriate choice since many literature studies report peaks of kinetic energy during the development of turbulent bands (Tao *et al.*, 2018).

3.1 Problem formulation

The flow considered is a plane channel flow at Reynolds number $Re = U_c H/\nu$, with U_c being the centreline velocity of the laminar Poiseuille flow, H being the half width of the channel and ν the kinematic viscosity. The Reynolds number is varied by changing the pressure gradient, while the volume flux remains constant, with bulk velocity $U_b = 3/2$. The dynamics of this flow is studied by decomposing the instantaneous velocity field, $\mathbf{u} = [u, v, w]^T$, into the laminar base flow $\mathbf{U} = [U(y), 0, 0]$ and a perturbation $\mathbf{u}' = [u', v', w']^T$. The dynamics of the perturbations of the laminar base flow is computed by solving the perturbative nonlinear incompressible Navier-Stokes equations:

$$\begin{cases} \dfrac{\partial u_i'}{\partial x_i} = 0, \\ \dfrac{\partial u_i'}{\partial t} + u_j' \dfrac{\partial u_i'}{\partial x_j} + u_j' \dfrac{\partial U_i}{\partial x_j} + U_j \dfrac{\partial u_i'}{\partial x_j} = -\dfrac{\partial p'}{\partial x_i} + \dfrac{1}{Re} \dfrac{\partial^2 u_i'}{\partial x_j}, \end{cases} \tag{3.1}$$

with $\mathbf{U} = [U(y), 0, 0]$, $U(y) = 1 - y^2$ being the laminar streamwise velocity profile, p' the pressure perturbation, while x_i is the Cartesian reference frame having components x, y, z, for the streamwise, wall-normal and spanwise directions, respectively. No-slip boundary conditions are imposed at the walls for the three velocity components, while periodicity is fixed in the streamwise and spanwise directions.

In order to find the minimal seed for the considered flow, we first search for the *optimal* perturbation $\mathbf{u}'$ at $t = 0$, providing the maximum value of the objective function at target time T. Following previous works (Cherubini *et al.*, 2010*a*; Pringle & Kerswell, 2010), we choose as objective function the energy gain $G(T) = E(T)/E(0)$, where:

$$E(t) = \frac{1}{2V} \int_V (u'(t)^2 + v'(t)^2 + w'(t)^2) dV \tag{3.2}$$

is the kinetic energy at time t and V is the volume of the computational domain. In order to find the initial perturbation $\mathbf{u}'(0)$ having given initial energy $E(0) = E_0$, providing the largest possible energy $E(T)$ at the target time, an optimization loop is set using the Lagrange multiplier technique (Zuccher

et al. (2004), Pringle & Kerswell (2010), Cherubini *et al.* (2011)). A Lagrangian functional is defined by augmenting the objective function with the following constraints: i) the optimal perturbation $\mathbf{u}'(t)$ must be solution of the Navier-Stokes equations at all times $t \in]0, T[$; ii) it must be divergence free at all times $t \in [0, T]$; and iii) it must have energy norm equal to a given value E_0 at $t = 0$. With these constraints, the Lagrangian functional reads:

$$\begin{aligned}\mathcal{L}(u_k', p', u_k^\dagger, p^\dagger, u_k'(0), u_k'(T), \lambda) = \frac{E(T)}{E(0)} \\ - \int_0^T \int_V u_i^\dagger \left(\frac{\partial u_i'}{\partial t} + \frac{\partial (u_i' u_j')}{\partial x_j} + \frac{\partial (U_i u_j')}{\partial x_j} + \frac{\partial (u_i' U_j)}{\partial x_j} + \frac{\partial p}{\partial x_i} - \frac{1}{Re} \frac{\partial^2 u_i'}{\partial x_j} \right) dV dt \\ - \int_0^T \int_V p^\dagger \frac{\partial u_i'}{\partial x_i} dV dt - E^\dagger \left(\frac{E_0}{E(0)} - 1 \right).\end{aligned} \tag{3.3}$$

with $\mathbf{u}^\dagger$, $p^\dagger$ and $E^\dagger$ being the Lagrangian multipliers (or adjoint variables).

To maximise the augmented functional $\mathcal{L}$ we evaluate its variation with respect to the direct and adjoint variables and set it to zero. The variation of the Lagrangian functional with respect to the direct variables $\mathbf{u}'$, p', provides the following adjoint equations:

$$\begin{cases} \dfrac{\partial u_i^\dagger}{\partial x_i} = 0, \\ \dfrac{\partial u_i^\dagger}{\partial t} - u_j^\dagger \dfrac{\partial u_i'}{\partial x_j} + u_j' \dfrac{\partial u_i^\dagger}{\partial x_j} - u_j^\dagger \dfrac{\partial U_i}{\partial x_j} + U_j \dfrac{\partial u_i^\dagger}{\partial x_j} = -\dfrac{\partial p^\dagger}{\partial x_i} + \dfrac{1}{Re} \dfrac{\partial^2 u_i^\dagger}{\partial x_j}. \end{cases} \tag{3.4}$$

The optimization problem is then solved using a direct-adjoint looping algorithm (as done in previous works by Pringle & Kerswell (2010), Cherubini *et al.* (2010*a*), among others), which consists in integrating iteratively in time the direct and adjoint equations between 0 and T to evaluate the gradient of $\mathcal{L}$ with respect to $\mathbf{u}'(0)$, which is then used to update the initial perturbation using a gradient rotation algorithm (Foures *et al.*, 2013; Farano *et al.*, 2016, 2017). Convergence is attained when the variation of the gain between two successively iterations is smaller then a chosen threshold, $\epsilon = 5 \times 10^{-8}$ (some details about the optimization problem and the direct-adjoint algorithm are reported in the section 2.2).

For computing the minimal seed, the variational optimization is coupled with an energy-bisection procedure. Two different optimizations are initialised with a random divergence-free perturbation for low T, with a value of E_0 sufficiently high (low) to induce transition (relaminarization) at longer times. The energy is bisected and the optimization repeated, using the results of the previous optimisation as initial guess. Energy-bisection is at first carried out for a low ($\mathcal{O}(10)$) target time in order to have a

very rough (but computationally cheap) upper estimate of the initial minimal energy threshold $E_{0_{min}}$. Then, the target time is increased at $\mathcal{O}(100)$ and the energy bisection is repeated, allowing to converge towards $E_{0_{min}}$.

The optimization algorithm is implemented within the open source code $Channelflow$ (channelflow.ch) (Gibson *et al.* (2021)). Both direct and adjoint equations are solved using a Fourier-Chebychev discretization in space and a third-order semi-implicit backward difference scheme for the time integration. An influence matrix method with Chebyshev tau correction was used to enforce no-slip boundary condition at the walls.

The domain size in the streamwise, normal and spanwise directions is $L_x \times L_y \times L_z = 250 \times 2 \times 125$, while the number of grid points in the same directions are $N_x \times N_y \times N_z = 1024 \times 65 \times 1024$. This results in a numerical resolution comparable with those used by Shimizu & Manneville (2019) and Kashyap *et al.* (2020) for the same range of Reynolds numbers. Finally, it should be noticed that the fact that optimizations are performed in a large domain involves challenging computations in terms of memory, especially for the highest considered target time, $T = 150$. In fact, the direct-adjoint algorithm requires storage of the flow field snapshots $\mathbf{u}'$ at each time step, in order to evaluate the term coupling direct and adjoint variables in the adjoint equations. For alleviating the storage requirement, a checkpointing technique is used, similar to that used in Griewank & Walther (2000) and Hinze *et al.* (2006).

3.2 Results

Nonlinear optimizations are performed for four values of $Re = 1000, 1150, 1250, 1568$, chosen in the range of Reynolds numbers for which the plane Poiseuille flow is linearly stable and the turbulent state appears in the form of turbulent-laminar patterns (Tao *et al.* (2018), Kashyap *et al.* (2020)). As reported by Xiong *et al.* (2015), the onset of bands does not lead to sustained turbulence for $Re < 1000$. In contrast, for $Re \geq 1000$, the bands can split, providing a mechanism for turbulence spreading leading to the coexistence of laminar regions with inclined turbulent bands, which persist up to $Re > 3900$, for which only featureless turbulence is present. Figure 3.1 (a) provides the influence of the target time on the optimal energy gain for $Re = 1150$ and given input energy $E_0 = 1.1 \times 10^{-7}$. The energy gain grows with the target time following a quasi exponential trend for $T < 40$ and for $T > 50$, reaching an amplification of three orders of magnitude for $T > 80$. No saturation of the

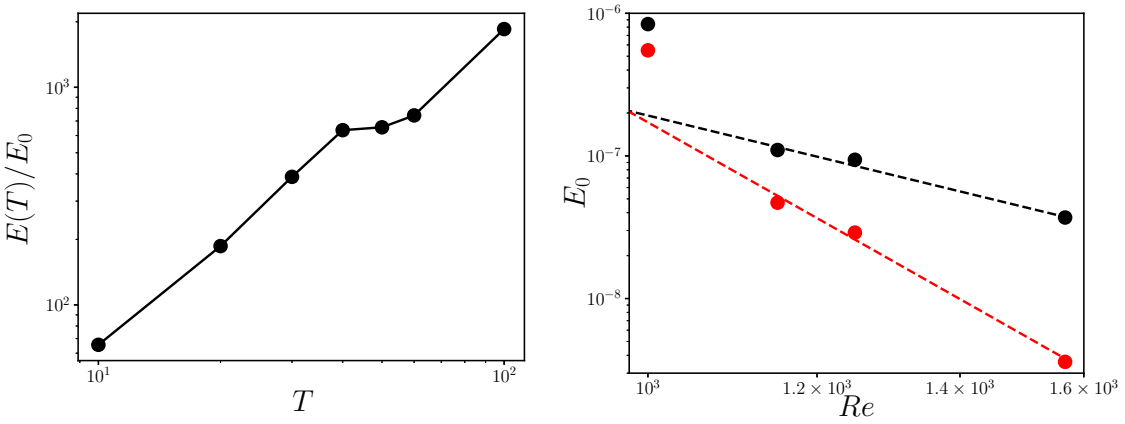

(a) (b)

Figure 3.1: (a) Optimal energy gain versus target time T for $Re = 1150$ and $E_0 = 1.1 \times 10^{-7}$. (b) Minimal energy threshold E_{0min} for transition to turbulence (red dots) and upper estimate obtained for $T = 10$ (black dots). The black and red lines represent the power-law for low ($\mathcal{O}(10)$) and high ($\mathcal{O}(100)$) target times, respectively, for $Re > 1000$.

final energy is observed for $T \leq 100$, since very long (i.e., $\mathcal{O}(10^3)$) times would be needed to fill the entire domain with turbulent bands, as it will be shown in subsection 3.2.3. As mentioned before, the procedure of bisection of the initial energy is at first carried out for $T = 10$, in order to have a computationally cheap upper bound for the computation of E_{0min}, which will be then carried out for $T = 100$ or $T = 150$, depending on the Reynolds number. For $Re < 1568$, the estimate of E_{0min} was obtained for $T = 100$, since we have verified that increasing the target time from $T = 100$ to $T = 150$ leads to slight changes of the minimal energy, namely, from 5.5×10^{-7} to 5.6×10^{-7} for $Re = 1000$. In contrast, at $Re = 1568$ it has been necessary to increase the target time to $T = 150$ to achieve a sufficiently good approximation of the threshold energy for generating bands. Figure 3.1 (b) provides the minimal input energy able to induce transition towards the turbulent bands, E_{0min} (red dots), together with its upper estimate obtained for $T = 10$ (black dots), for the four considered values of the Reynolds number. In the range of Re analysed, we tried to fit the minimal input energy with a power law of the type $E_{0_{min}} \propto Re^{-\gamma}$, but we obtained a satisfactory fit only by restraining the power law to the minimal seeds in the range $Re > 1000$ (red dashed line, obtained for $\gamma \approx 8.5$). A similar behaviour is observed for the upper estimate of $E_{0_{min}}$ obtained for $T = 10$ (black dashed line), although the associated value of γ is much lower. Incidentally, we observe that as expected, larger threshold initial energies are obtained for the lower target time $T = 10$ (black line). The fact that the minimal-seed energy obtained for $Re = 1000$ appears not to be aligned with the fitting line recovered for larger

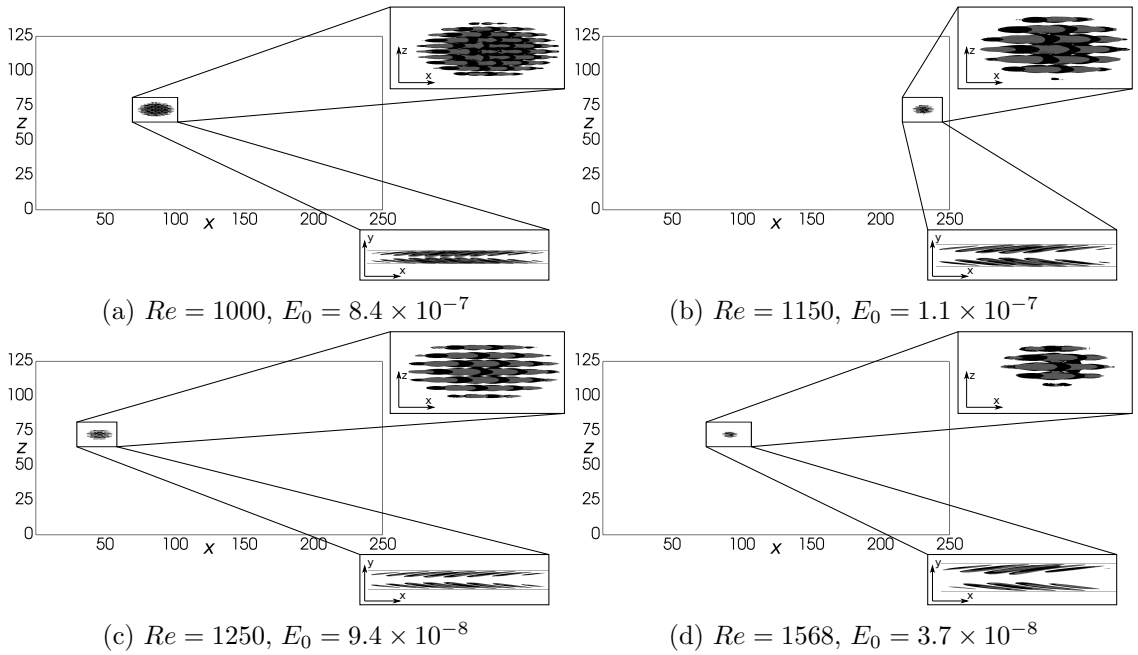

(a) $Re = 1000$, $E_0 = 8.4 \times 10^{-7}$ (b) $Re = 1150$, $E_0 = 1.1 \times 10^{-7}$

(c) $Re = 1250$, $E_0 = 9.4 \times 10^{-8}$ (d) $Re = 1568$, $E_0 = 3.7 \times 10^{-8}$

Figure 3.2: Nonlinear optimal perturbation at time $t = 0$ for different Reynolds numbers with $U_{bulk} = 3/2$ obtained at target time $T = 10$ with the input energy reported in figure 3.1 by the black dots. Isosurface of the streamwise velocity (light grey for positive and black for negative values, $u = \pm 0.003$).

values of Re might have been anticipated. As reported by Xiong *et al.* (2015), $Re = 1000$ is exactly the limit value of the Reynolds number for which band splitting begins to be observed. Thus, at this threshold value of Re the flow dynamics may present a transitional behaviour between two different regimes, not fitting with that observed at larger values of Re. Finally, we note that the exponent of the power law approximating the minimal-energy threshold is much higher than those reported in previous works. For the plane Couette flow, a minimal seed energy varying as $Re^{-2.7}$ was reported by Duguet & Schlatter (2013); for the asymptotic suction boundary layer, a scaling of Re^{-2} was found by Cherubini *et al.* (2015). This discrepancy may be more likely linked to the much larger domain considered in the present study, rather than to the different type of flow.

3.2.1 Nonlinear optimal perturbations

The initial optimal solutions obtained for the target time $T = 10$ at the threshold energy able to trigger turbulence are shown in figure 3.2 for the four Re considered. In all cases, the optimal perturbation is spatially localised in a small region of the domain, with a shape similar to that of a spot, which is composed of alternating positive and negative finite-size streamwise streaks. Despite the fact that spatial

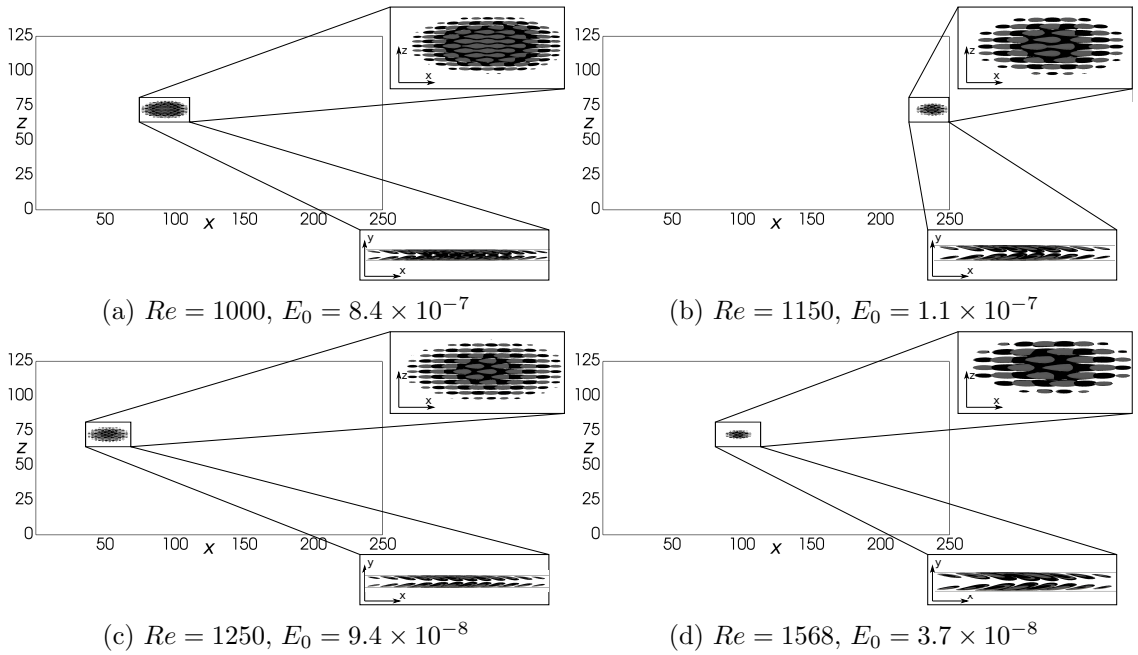

(a) $Re = 1000$, $E_0 = 8.4 \times 10^{-7}$ (b) $Re = 1150$, $E_0 = 1.1 \times 10^{-7}$

(c) $Re = 1250$, $E_0 = 9.4 \times 10^{-8}$ (d) $Re = 1568$, $E_0 = 3.7 \times 10^{-8}$

Figure 3.3: Nonlinear optimal perturbations at time $t = T$ for different Reynolds numbers with $U_{bulk} = 3/2$ obtained at target time $T = 10$ with the input energy reported in figure 3.1 by the black dots. Isosurface of the streamwise velocity (light grey for positive and black for negative values $u = \pm 0.02$).

localization has been already observed in nonlinear optimizations (for instance, see Cherubini *et al.* (2011), Monokrousos *et al.* (2011), Pringle *et al.* (2012)), the structure of this optimal perturbation is rather different from that of previously computed nonlinear optimal perturbations. In contrast, it closely resembles the optimal wave packet recovered by linear optimization and windowing, obtained for the boundary layer flow by Cherubini *et al.* (2010*b*). This is probably due to the low target time and initial energy used for this computations, which partially hinders the development of nonlinear effects. At $t = 0$, all the optimal perturbations shown in figure 3.2 present vortical structures inclined in the opposite direction from the shear (see the $x - y$ planes in the right bottom of each frame). Whereas, at the target time, the perturbations reverse their inclination, pointing in the same direction of the shear flow, as shown in figure 3.3. This streamwise tilting is a common feature of optimal perturbations in shear flows (Cherubini *et al.*, 2010*a*; Pringle & Kerswell, 2010; Duguet & Schlatter, 2013), and suggests that the Orr mechanism is a fundamental mechanism involved in the early stage of transition to turbulence, with characteristic time approximately equal to 10 (Orr, 1907). One can also notice that, for $T = 10$, the shape of the optimal perturbations does not change much while evolving

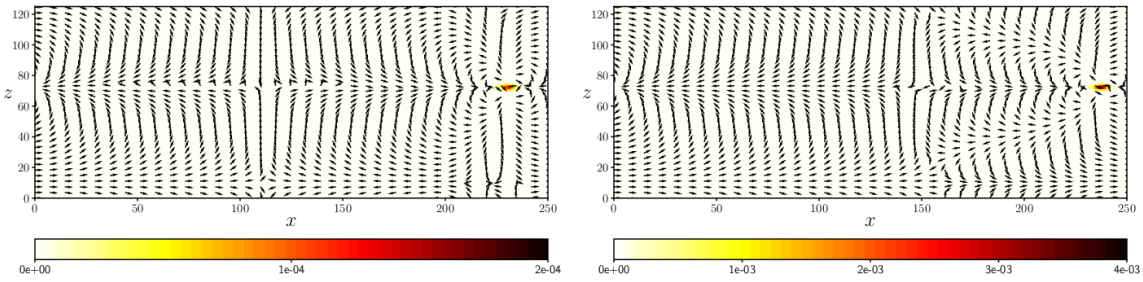

(a) $t = 0$ (b) $t = T$

Figure 3.4: Shaded isocontours of the crossflow energy E_{cf} together with the normalized y-integrated large-scale flow (vectors) characterizing the nonlinear optimal for $Re = 1150$, $E_0 = 1.1 \times 10^{-7}$, $T = 10$: (a) initial optimal solution, (b) optimal solution at the target time.

from $t = 0$ to the target time, as shown in figure 3.3, remaining characterized by alternating positive and negative streaks localised in a spot-like region.

Duguet & Schlatter (2013) show that oblique bands arise as a result of advection of newly nucleated streaks in the direction of a large-scale flow, which is oblique with respect to the streamwise direction. The local orientation of the large-scale flow is thus responsible for the obliqueness of the laminar-turbulent interface of growing incipient spots as well as for maintaining turbulent stripes (Duguet & Schlatter, 2013). To ascertain whether the computed nonlinear optimal perturbations contain the seed for the development of turbulent bands, we compute the large-scale flow related to the optimal disturbances by averaging the instantaneous velocity field in the wall normal direction as $\overline{u_i} = \int_{-1}^{1} u_i dy$. Notice that $\overline{u}$ is zero where the flow is laminar, close to zero where the flow is turbulent, but it is non zero at the laminar-turbulent interfaces, due to a mismatch of the streamwise flow rates across them, linked to the presence of overhang regions. In figure 3.4, we have reported the isocontours of the cross-flow energy $E_{cf} = (1/2)\int(v^2 + w^2)dy$, surrounded by the large-scale field $(\overline{u}, \overline{w})$, for the initial optimal perturbation at $Re = 1150$, $E_0 = 1.1 \times 10^{-7}$. The optimal flow field is characterized by two different scales: a small-scale flow embedded within the spot-like structure and a large-scale flow in the form of large vortices filling the whole domain. The latter is characterised by a streamwise flow entering the spot and a spanwise flow exiting from it, constituting a quadrupolar structure. Quadrupolar large-scale flow around spots or laminar-turbulent bands has been observed in plane Couette flow (Schumacher & Eckhardt (2001); Lagha & Manneville (2007)) and plane Poiseuille flow (Lemoult *et al.*, 2014), due to the shearing of the streamwise velocity and the breaking of the spanwise homogeneity (Wang *et al.*, 2020). Notice that this large-scale flow, which is not associated with the

presence of overhang regions, remains almost unchanged from $t = 0$ to $t = T$ (compare figures 3.4 (a) and (b)).

Increasing the target time to $T = 100$ for $Re = 1150$, while keeping $E_0 = 1.1 \times 10^{-7}$, we obtain the

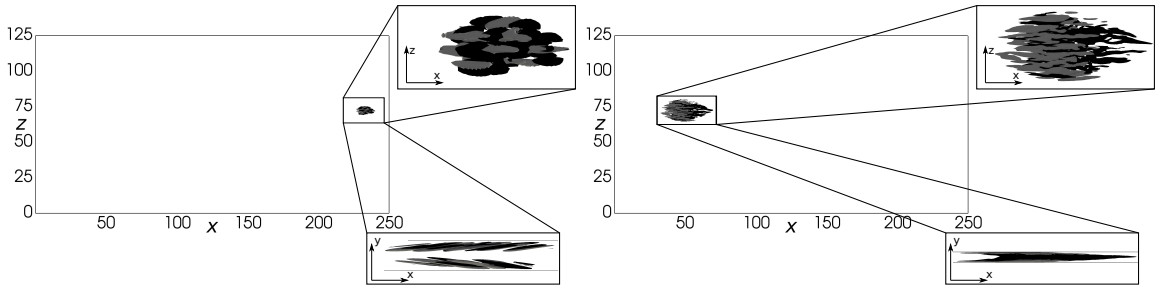

(a) $t = 0$ (b) $t = T$

Figure 3.5: Optimal perturbation for $Re = 1150$, $U_{bulk} = 3/2$, $T = 100$ and $E_0 = 1.1 \times 10^{-7}$ at (a) $t = 0$ and (b) $t = T$: isosurface of the streamwise velocity (light grey for positive and black for negative values, $u = \pm 0.003$ (a) and $u = \pm 0.12$ (b)).

optimal solution shown in figure 3.5 (a), which presents a localised structure similar to that computed for lower target times, despite being not perfectly symmetric and having thicker streaks compared to those at lower target time. The optimal solution at the target time, shown in figure 3.5(b), is very similar to that of a turbulent spot, now clearly presenting an overhang region.

Moreover, it is characterized by a quadrupolar large-scale flow surrounding the spot-like small-scale disturbances (not shown). Starting from this optimal (but yet not minimal) solution, the optimize-and-bisect procedure is carried out at $T = 100$ for $Re = 1150$. The same procedure is carried out for all the considered values of Re, for obtaining the minimal seeds whose energy is reported in figure 3.1 (b).

3.2.2 Minimal seed at different Reynolds

The minimal seed for turbulent bands obtained at $Re = 1150$ for $E_{0_{min}} = 4.7 \times 10^{-8}$ is reported in figure 3.6 (a). Noticeably, it does not present significant differences compared to that at the same target time with a higher input energy, provided in figure 3.5 (a). A three-dimensional visualization, provided in figure 3.7 (b) shows the streamwise and spanwise alternance of finite-size streaks together with spanwise-inclined vortical structures closer to the wall. As shown in figure 3.6 (b-c), these finite-size streaks increase their streamwise length, and the initial wave packet turns at $t = 25$ into four pairs of elongated streamwise streaks. At $t = 50$, some wiggling of the streaks can be recovered in

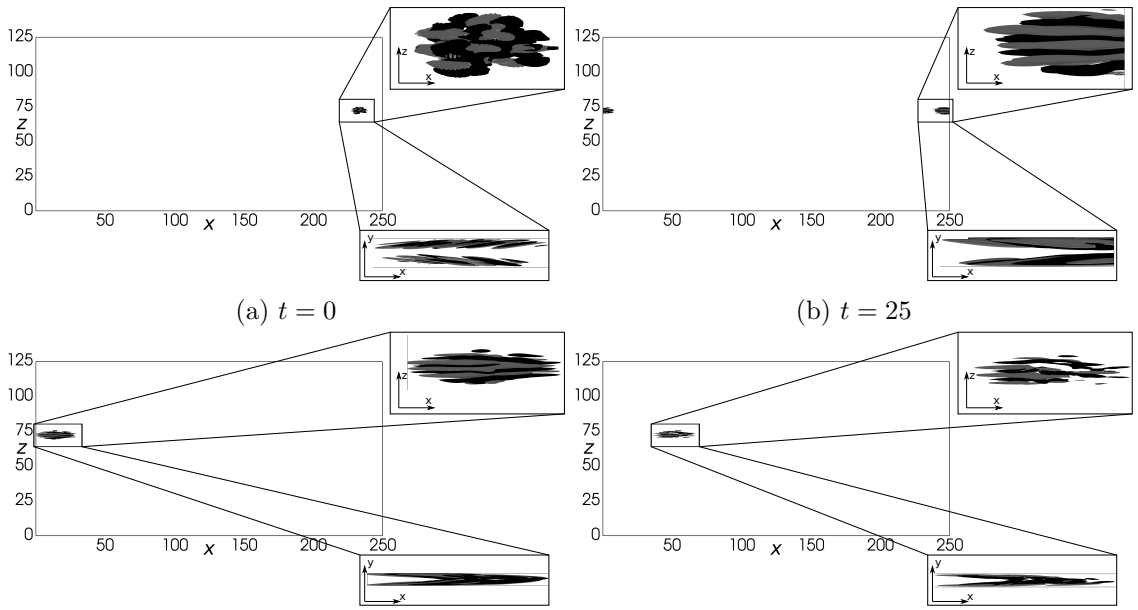

(a) $t = 0$ (b) $t = 25$

(c) $t = 50$ (d) $t = T$

Figure 3.6: Minimal seed for $Re = 1150$, $T = 100$ and $E_0 = 4.7 \times 10^{-8}$ at (a) $t = 0$, (b) $t = 25$, (c) $t = 50$, (d) $t = T$: isosurface of the streamwise velocity (light grey for positive and black for negative values, $u = \pm 0.003$ (a), $u = \pm 0.02$ (b-c) and $u = \pm 0.08$ (d).

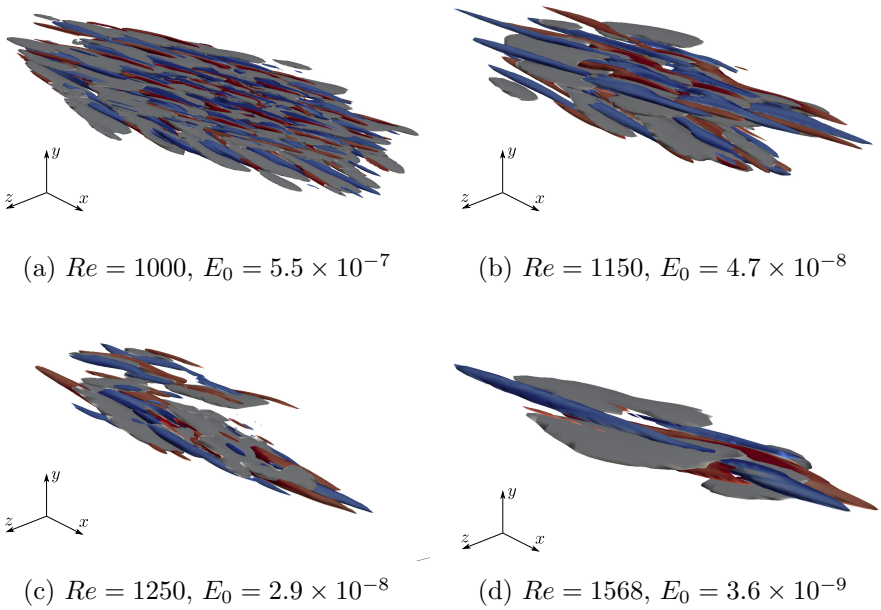

(a) $Re = 1000$, $E_0 = 5.5 \times 10^{-7}$ (b) $Re = 1150$, $E_0 = 4.7 \times 10^{-8}$

(c) $Re = 1250$, $E_0 = 2.9 \times 10^{-8}$ (d) $Re = 1568$, $E_0 = 3.6 \times 10^{-9}$

Figure 3.7: Minimal seed at different Reynolds numbers: isosurface of negative streamwise velocity ($u = -0.0025$, light grey) and Q-criterion ($Q = 0.003$) coloured by the streamwise vorticity (positive red, negative blue).

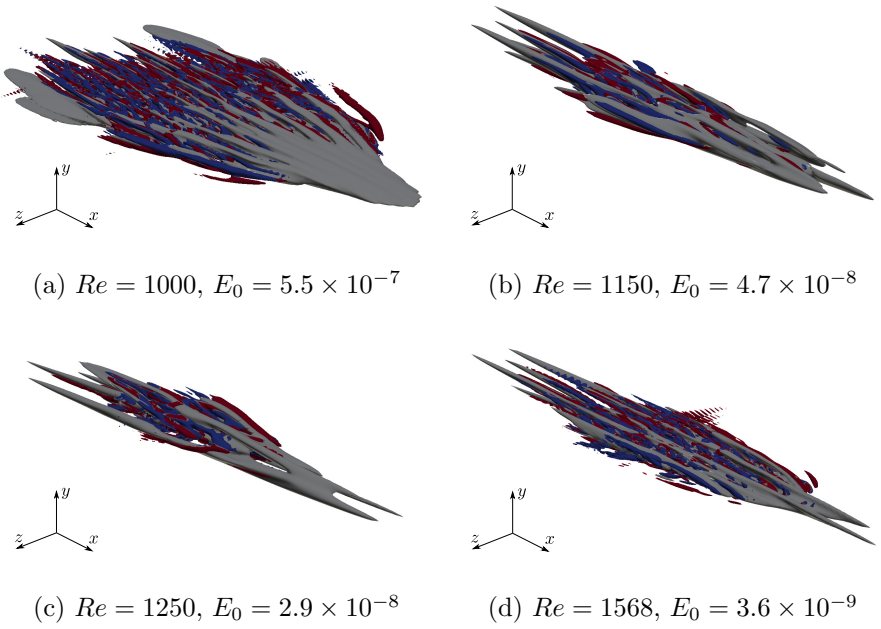

(a) $Re = 1000$, $E_0 = 5.5 \times 10^{-7}$ (b) $Re = 1150$, $E_0 = 4.7 \times 10^{-8}$

(c) $Re = 1250$, $E_0 = 2.9 \times 10^{-8}$ (d) $Re = 1568$, $E_0 = 3.6 \times 10^{-9}$

Figure 3.8: Minimal seed at target time $t = T$ for different Reynolds numbers: isosurface of negative streamwise velocity ($u = -0.03$, light grey) and Q-criterion ($Q = 0.005$) coloured by the streamwise vorticity (positive red, negative blue).

the center of the wave packet, which turns at target time into an arrow-shaped packet (figure 3.6 (d)), as also shown in the three-dimensional view of figure 3.8 (b). Comparing figure 3.5 (b) with figure 3.6(d), one can also notice that, at target time, the minimal perturbation differs from that computed for $E_0 > E_{0min}$, having completely lost symmetry along the z axis. A clear overhang region is present as well, and the structure in the $x - y$ plane recalls that experimentally observed in turbulent spots by Lemoult *et al.* (2013). Moreover, the large-scale flow, shown in figure 3.9, maintains the previously observed quadrupolar structure, presenting large-scale vortices almost symmetric in the spanwise direction. The same large-scale quadrupolar structure surrounding the minimal-energy wakepacket is observed also for the other considered Reynolds numbers (not shown). Whereas, the small-scale minimal perturbations are found to considerably change with the Reynolds numbers, as shown in figure 3.7. In particular, a further localization of the initial wavepacket is observed for increasing Re, leading to a minimal structure at $Re = 1568$ which closely resembles that found for the plane Couette and the asymptotic suction boundary-layer flow in small domains (Duguet & Schlatter, 2013; Rabin *et al.*, 2012; Cherubini *et al.*, 2015). Apart from the spatial localization, the main structures observed within the minimal-seed wavepackets are essentially the same, namely, finite-size

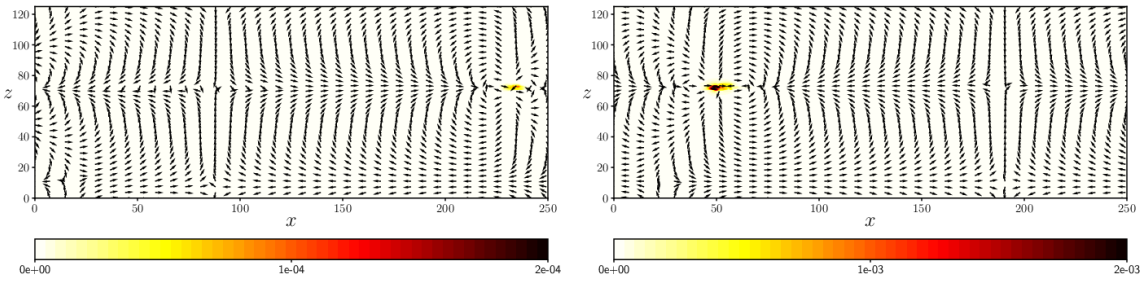

(a) $t = 0$ (b) $t = 0$

Figure 3.9: Isocontours of the crossflow energy E_{cf} with the normalized y-integrated large scale flow (vectors) for $Re = 1150$, $E_0 = 4.7 \times 10^{-8}$, $T = 100$: (a) initial optimal solution, (b) optimal solution at the target time.

streaks flanking upstream-tilted elongated vortices. As a result of the discrepancies recovered at initial time, the minimal seeds obtained at different Re evolve differently in time, presenting an increasing localization for larger values of Re, as provided in figure 3.8. However, all of the wavepackets present an arrow-shaped structure, with the downstream region essentially characterized by low-speed streaks, and the core region filled with small-scale vortices together with some coherent streamwise streaks. Moreover, the large-scale quadrupolar structure observed at $t = 0$ is maintained at target time for all the considered values of Re, as shown in figure 3.9 (b) for $Re = 1150$.

The premultiplied energy spectra of the minimal seed obtained at $Re = 1150$ are reported in figure 3.10 by the coloured contours. The streamwise perturbation energy peaks for $\lambda_z \approx 2.45$ and $\lambda_x \approx 3.78$, whereas the wall-normal and spanwise perturbation energy have largest amplitude at $\lambda_z \approx 1$, $\lambda_x \approx 4$ with a secondary peak for $\lambda_z \approx 2$ and $\lambda_x \approx 25$. The lowest of these wavelengths are close to those reported by Lemoult *et al.* (2014) during the development of turbulent spots at similar Reynolds numbers, and are linked to the finite size of the streaks. Whereas, the largest wavelengths are directly linked to the streamwise and spanwise size of the wavepacket. Very similar spectra are found to characterize the nonlinear optimal perturbations at higher initial energy (solid contours in figure 3.10). The premultiplied energy spectra of the minimal seeds obtained for the other values of Re are reported in figure 3.11 by the shaded contours ($Re = 1000$) and the dashed lines (black for $Re = 1150$, blue for $Re = 1250$, green for $Re = 1568$). As a consequence of the increased spatial localization, the overall distribution of the energy spectra is displaced towards higher values of λ_x, λ_z when Re increases. This effect is coupled with a narrowing and displacement of the spectra towards higher values of y, which is a consequence of an increased localization also in the wall-normal direction.

The primary and secondary peak values, reported in table 3.1 are also considerably influenced by the Reynolds number.

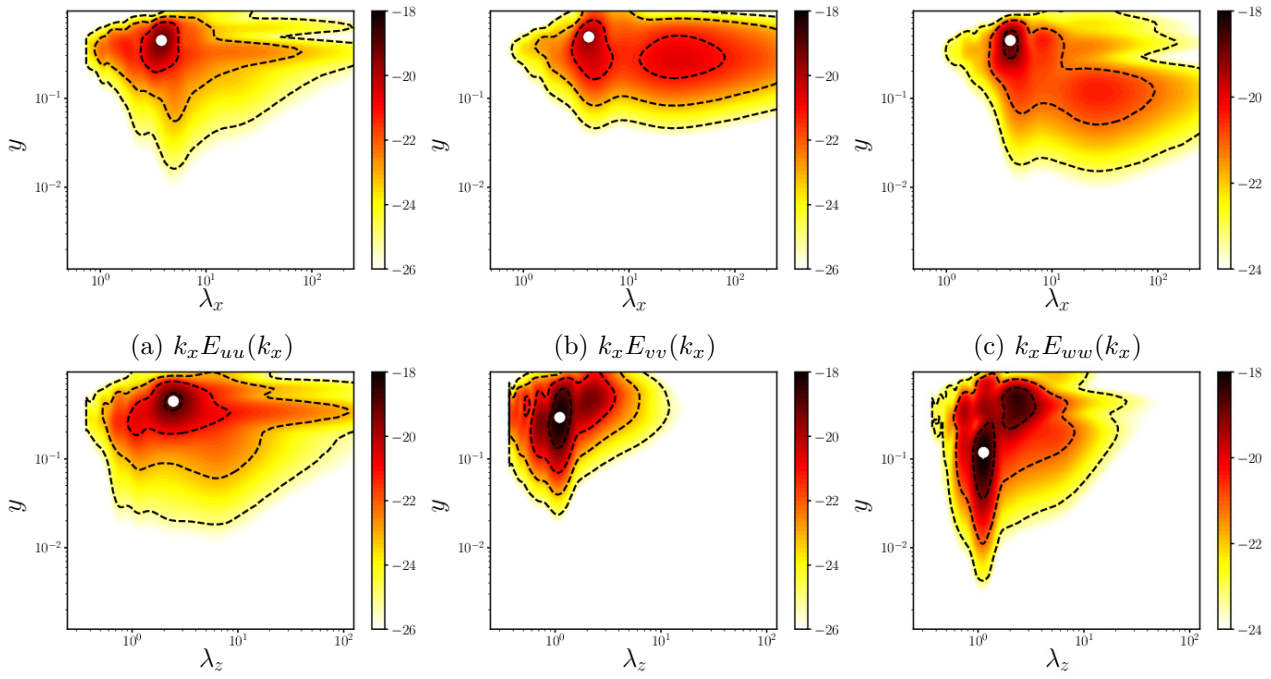

Figure 3.10: Logarithm of the premultiplied spectral energy versus the wall-normal distance y^+ for the initial optimal solution at $Re = 1150$ and $T = 100$ for $E_0 = 1.1 \times 10^{-7}$ (coloured contours) and $E_0 = 4.7 \times 10^{-8}$ (black contours). The white dots indicate the energy peaks.

3.2.3 Minimal seed evolution in time

In this section, we analyse the time evolution of the minimal seeds towards the turbulent bands. In figure 3.12 (a), the time evolution of the kinetic energy obtained from direct numerical simulations initialised with the minimal seeds, is reported. In all cases, the kinetic energy strongly increases in time until saturating towards a statistically constant value. For the lowest considered Reynolds numbers, we observe a rapid initial increase of the kinetic energy, followed by a slow phase of saturation of the energy. Whereas, for larger Re, the initial growth is slower and leads to lower values of the kinetic energy at small time. One can notice once again that at $Re = 1000$ the flow appears to behave rather differently from what observed at larger Reynolds numbers. However, the minimal seeds at larger Re, despite having lower initial energy, tend towards higher values of the kinetic energy at large times, suggesting that for larger Reynolds numbers, turbulence eventually occupies a larger portion of the

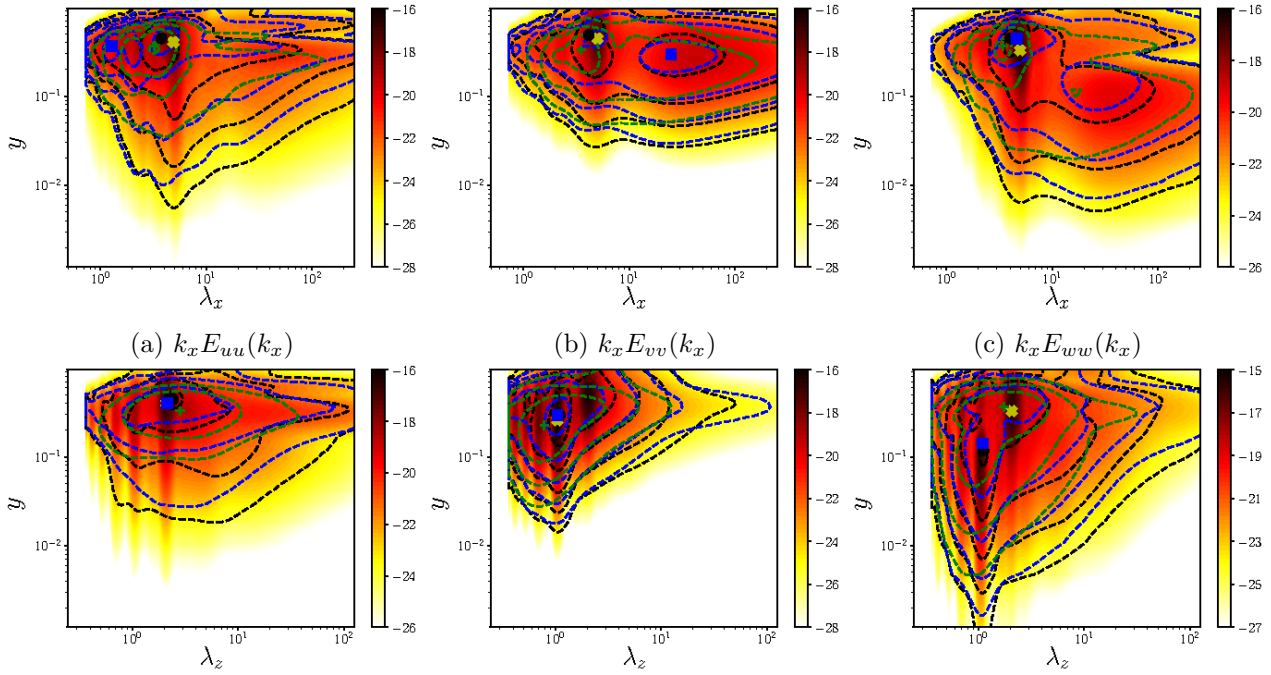

(a) $k_x E_{uu}(k_x)$ (b) $k_x E_{vv}(k_x)$ (c) $k_x E_{ww}(k_x)$

(d) $k_z E_{uu}(k_z)$ (e) $k_z E_{vv}(k_z)$ (f) $k_z E_{ww}(k_z)$

Figure 3.11: Logarithm of the premultiplied spectral energy versus the wall-normal distance y^+ for the initial optimal solution at different Reynolds numbers at $T = 100$: $Re = 1000$ for $E_0 = 5.5 \times 10^{-7}$ (coloured contours), $Re = 1150$ for $E_0 = 4.7 \times 10^{-8}$ (black contours), $Re = 1250$ for $E_0 = 2.9 \times 10^{-8}$ (blue contours) and $Re = 1568$ for $E_0 = 5.8 \times 10^{-9}$ (green contours). The symbols indicate the peaks of the energy, also reported in table 3.1.

Re	$(\lambda_x)_u$	$(\lambda_z)_u$	$(\lambda_x)_v$	$(\lambda_z)_v$	$(\lambda_x)_w$	$(\lambda_z)_w$
1000	4.897 (2.390)	2.117 (3.307)	4.995 (38.45)	1.049 (2.198)	4.995 (36.34)	2.080 (1.042)
1150	3.784 (1.618)	2.449 (1.093)	4.163 (25.56)	1.105 (2.049)	4.028 (25.56)	1.125 (2.218)
1250	1.287 (2.236)	2.153 (2.114)	24.98 (4.991)	1.049 (0.508)	4.625 (24.16)	1.105 (2.639)
1568	3.244 (1.916)	2.838 (1.217)	3.518 (18.75)	0.790 (1.992)	3.6421 (20.12)	1.759 (0.958)

Table 3.1: Streamwise and spanwise wavelengths $\lambda_{x,z}$ associated with the primary and secondary (in brackets) peaks of the premultiplied energy spectra of u, v, w, shown in figure (3.11) for different Reynolds numbers.

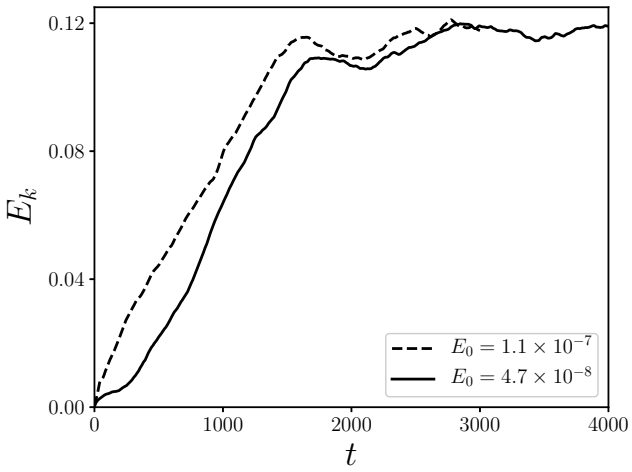

Figure 3.12: Time evolution of the kinetic energy for the minimal seeds obtained for $Re = 1150$ for the two initial energy $E_0 = [1.4 \times 10^{-7}], 4.7 \times 10^{-8}$.

domain.

This can be verified by analysing the time evolution of the crossflow energy and y-averaged flow fields for the minimal seeds at different Reynolds numbers. For $Re = 1150$, figure 3.13 shows that, as previously noticed (see also figure 3.6), the localised minimal solution breaks rapidly its symmetry along the spanwise direction, presenting a clearly asymmetric (but still spatially compact) structure at $t = 500$, as shown in figure 3.13 (b). This asymmetric wavepacket evolves via nucleation of new streaky structures (see Parente *et al.* (2021*b*) concerning the mechanism of creation of the streaks) in the direction of the inclined laminar-turbulent interface, clearly forming a singular turbulent band, as it can be observed for $t = 900$. The newly-formed turbulent band continues growing in an oblique direction with angle $\approx 28°$ until reaching the periodic boundaries, where it interacts with itself ($t = 1500$). This triggers splitting of the previously isolated band ($t = 2500$), which saturates reaching a laminar-turbulent pattern filling the whole domain at $t = 4000$. The same behaviour has been observed by Tao & Xiong (2013) and Xiong *et al.* (2015) by injecting in a plane Poiseuille flow a "seed" of the turbulent bands, similar in shape to the instantaneous field at $t = 500$ in figure 3.13. Analysing the large-scale flow, we can observe the formation of a small recirculation zone upstream of the spot during its evolution. Moreover, when the bands are formed, the large-scale flow is found to turn clockwise around bands with positive angle and anti-clockwise around bands with negative angle. In fact, all the bands are formed in correspondence with the shear layer which divides the different vortices. A rather similar behaviour is observed at $Re = 1000$, as shown in figure 3.14. Despite at

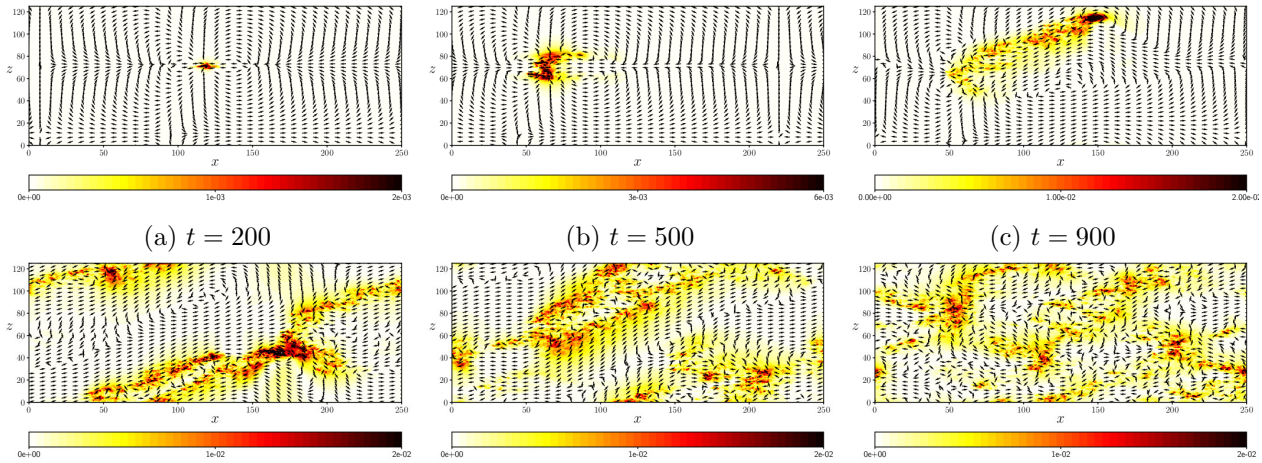

(a) $t = 200$ (b) $t = 500$ (c) $t = 900$

(d) $t = 1500$ (e) $t = 2500$ (f) $t = 4000$

Figure 3.13: Isocontours of the crossflow energy E_{cf} together with the normalized y-integrated large scale flow (vectors) for several instantaneous fields ($Re = 1150$, $E_0 = 4.7 \times 10^{-8}$, $T = 100$).

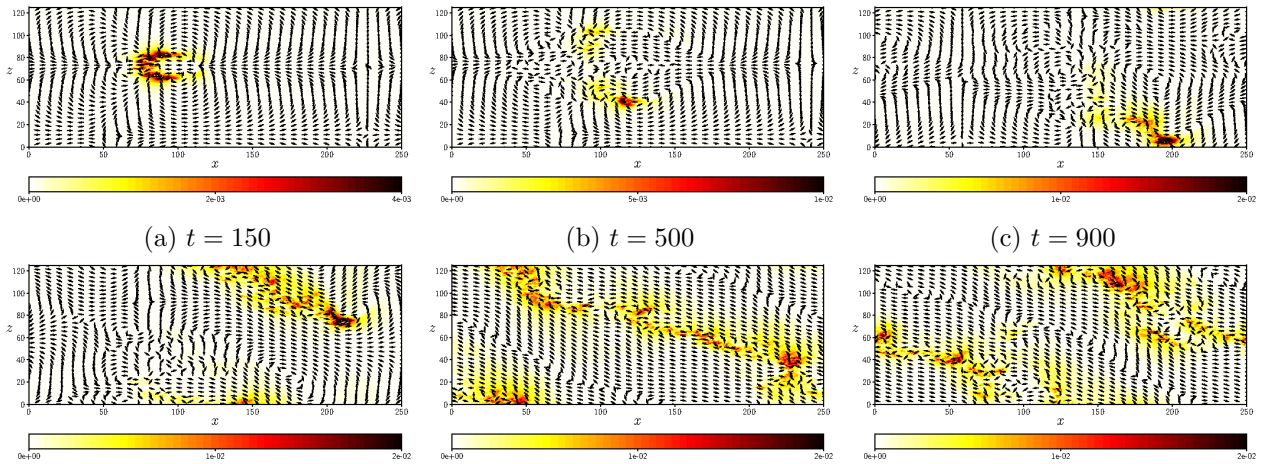

(a) $t = 150$ (b) $t = 500$ (c) $t = 900$

(d) $t = 1500$ (e) $t = 2500$ (f) $t = 3000$

Figure 3.14: Isocontour of the crossflow energy E_{cf} together with the normalized y-integrated large scale flow for several instantaneous fields ($Re = 1000$, $E_0 = 5.5 \times 10^{-7}$, $T = 100$).

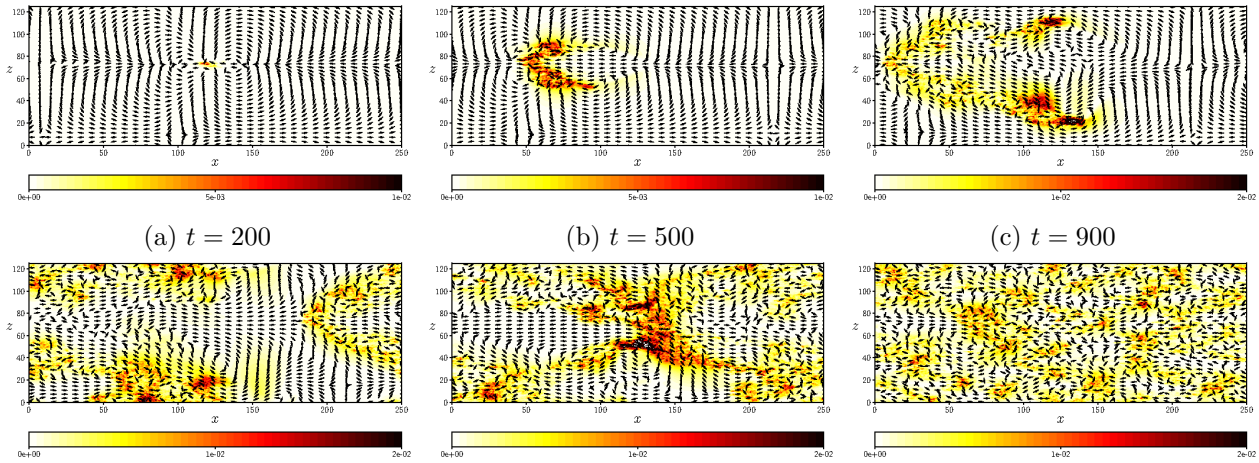

(a) $t = 200$ (b) $t = 500$ (c) $t = 900$

(d) $t = 1200$ (e) $t = 1500$ (f) $t = 3000$

Figure 3.15: Isocontour of the crossflow energy E_{cf} together with the normalized y-integrated large scale flow for several instantaneous fields ($Re = 1250$, $E_0 = 2.9 \times 10^{-8}$, $T = 100$).

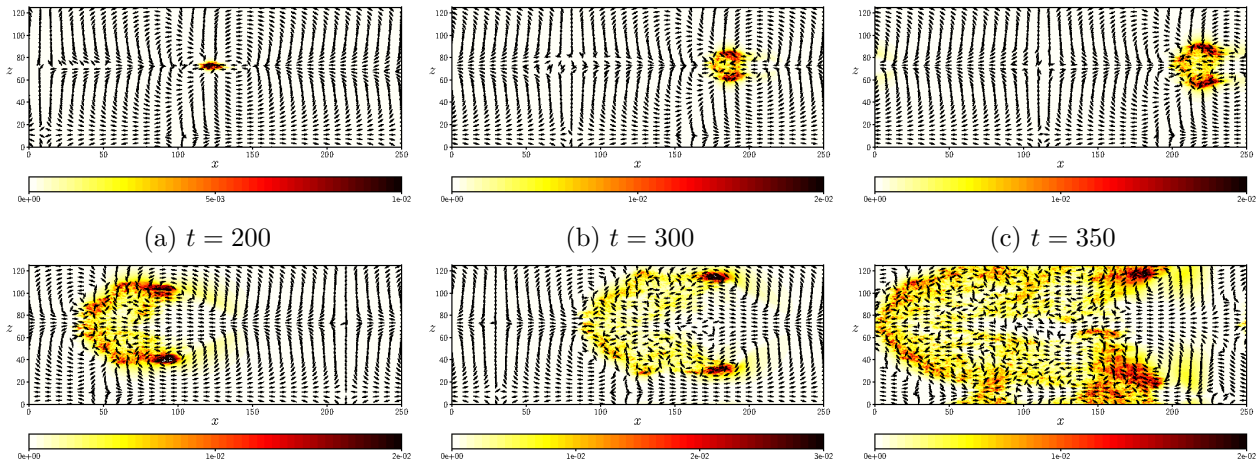

(a) $t = 200$ (b) $t = 300$ (c) $t = 350$

(d) $t = 500$ (e) $t = 600$ (f) $t = 900$

Figure 3.16: Isocontour of the crossflow energy E_{cf} together with the normalized y-integrated large scale flow for several instantaneous fields ($Re = 1568$, $E_0 = 3.6 \times 10^{-9}$, $T = 150$).

small times ($t = 150$) the minimal seed has evolved into an almost symmetric V-shaped spot, one of its two legs weakens in time ($t = 500$) and completely disappears at $t = 900$, evolving into a single band as observed for $Re = 1150$. Whereas, looking at the evolution in time for the cases at higher Reynolds number, the flow presents the same behaviour observed experimentally and numerically when turbulence is triggered by a spot (Carlson *et al.* (1982), Henningson & Kim (1991), Aida *et al.* (2010), Aida *et al.* (2011)). In fact, the localised perturbation initially evolves in the domain forming a turbulent spot (see figure 3.5), turning into a V-shape at $t = 500$, as shown in figure 3.15. At this time, two distinct fronts of the spots can be observed, which evolve in two symmetric bands with angle $\approx \pm 45°$ growing obliquely in the domain, as shown at $t = 900$. At $t = 1200$, they start to interact which each other, forming a spatio-temporally complex final state composed by a coexistence of turbulent and laminar patterns ($t = 3000$). Qualitatively the same behaviour is observed at $Re = 1568$, as shown in figure 3.16, although the spatial spreading of the bands appears to be more rapid than at lower Re, despite the initial energy of the perturbation is lower. Also in these cases, the bands are found to form right in the mixing layer between two large-scale counter-rotating vortices. Notice also that the same quasi-symmetric behaviour can be observed at lower Re, for a larger initial energy. In fact, the nonlinear optimal perturbation computed for $Re = 1150$ and $E_0 = 4.7 \times 10^{-8} > E_{0min}$ evolves in two distinct bands, showing a time evolution corresponding to that of the minimal seed at largest Re (not shown).

An explanation of this behaviour can be attempted by recalling that, in the channel flow, turbulent stripes have a probability of decay that increases with time, and that decreases with the Reynolds number (Paranjape, 2019). Thus, as all minimal seeds present an almost spanwise-symmetric structure, two proto-bands begin to be created at the edges of the large-scale vortices characterising the minimal seed. However, the probability of decay of these bands is higher for low Reynolds number, and increases in time, so when Re is sufficiently low one of these bands rapidly dies out, leading to the development of one isolated band. Increasing Re, the probability of decay of an initial band is lower, while the probability of splitting increases. Thus, both oblique bands originated at the sides of the minimal seed survive longer in time, until they split and interact, rapidly leading to the establishment of a spatio-temporally complex final state. Notice that injecting more initial energy at low value of Re has the same effect of increasing Re. In fact, an optimal perturbation with $E_0 > E_{0min}$ is less spatially localized, and is able to reach a much larger kinetic energy at $T = 100$, leading to more spatially-

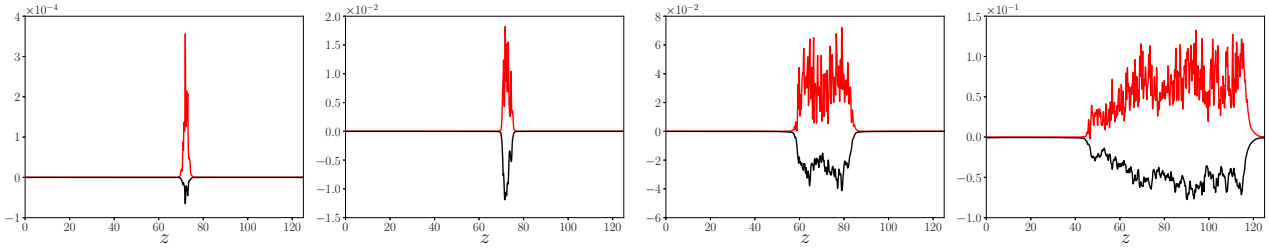

(a) $t = 0$ (b) $t = 100$ (c) $t = 500$ (d) $t = 900$

Figure 3.17: Spanwise distribution of the production (P, red line) and dissipation ($-\epsilon$, black line) terms integrated in $x-y$ planes for different instantaneous fields obtained evolving in time the minimal seed for $Re = 1150$, $E_0 = 4.7 \times 10^{-8}$, $T = 100$.

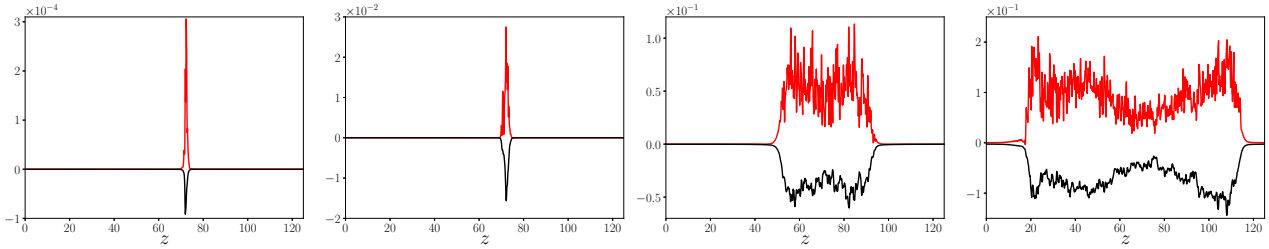

(a) $t = 0$ (b) $t = 100$ (c) $t = 500$ (d) $t = 900$

Figure 3.18: Spanwise distribution of the production (P, red line) and dissipation ($-\epsilon$, black line) terms integrated in $x-y$ planes for different instantaneous fields obtained evolving in time the minimal seed for $Re = 1250$, $E_0 = 2.9 \times 10^{-8}$, $T = 100$.

extended and energetic proto-bands, which allows their sustainment for a longer time.

To corroborate this conjecture, we make use the Reynolds-Orr equation to evaluate the production and dissipation of kinetic energy as, respectively:

$$P = -u_i' u_j' \frac{\partial U_i}{\partial x_j}, \qquad \epsilon = \frac{2}{Re} s_{ij}' s_{ij}' \quad \text{with} \quad s_{ij}' = \frac{1}{2}\left(\frac{\partial u_i'}{\partial x_j} + \frac{\partial u_j'}{\partial x_i}\right), \tag{3.5}$$

where the Einstein summation convention has been used. One can compare the time evolution of the production and dissipation terms, integrated in $x-y$ planes, for the minimal seeds at $Re = 1150$ and $Re = 1250$, provided in figure 3.17 and 3.18. For both Reynolds numbers, at $t = 0$ the production presents one single peak almost in the center of the spot ($z \approx 70$), which is found to exceed dissipation of almost an order of magnitude. Production of kinetic energy leads to a slight increase of the spanwise size of the wavepacket ($t = 100$), together with a further increase of the kinetic-energy production, probably due to the nucleation of new streaks which produce kinetic energy thanks to the lift-up effect. Due to the breakdown of the structures inside the spot, dissipation increases as well, reaching almost the same value than the production term. Notice also that a weak secondary peak begins to be visible

in the production term. At $t = 500$, the spot has strongly increased its size in the spanwise direction, presenting an almost symmetric shape with two peaks at $z \approx 55 - 60$ and $z \approx 80 - 85$. However, at $t = 900$, the evolution of the production and dissipation terms begins to strongly differ between the two considered Reynolds numbers. For $Re = 1250$, the spanwise distribution of the dissipation and production terms remains almost spanwise symmetric, centered at $z \approx 70$, with two distinct laminar-turbulent fronts at $z \approx 20$ and $z \approx 110$ (see figure 3.18). Whereas, for $Re = 1150$, the left-most part of the packet has almost faded away, while the right-most one has expanded up to $z \approx 110$, as shown in figure 3.17. The analysis of the production and dissipation terms clearly indicates that the minimal seed for turbulent bands leads to the generation of two almost symmetric regions of high production and dissipation, which can be seen as two distinct proto-bands. However, when the Reynolds number is lower, the weaker of these two proto-bands rapidly decays, leading to the development of an isolated band. Whereas, at larger Reynolds number, both bands survive for a sufficiently long amount of time to begin interacting between themselves.

3.3 Conclusion

In this Chapter, we have sought for the minimal-energy perturbations generating turbulent bands in plane Poiseuille flow. A nonlinear optimization maximising the kinetic energy at a given target time, coupled with initial energy bisection, has been used. The optimization was performed in very large domains, for a range of Reynolds number for which turbulent bands are sustained and lead to a spatio-temporally complex turbulent-laminar final state, namely $Re = 1000, 1150, 1250, 1568$ (the lowest value representing the threshold Re for which bands splitting and turbulence spreading can be observed).

The influence of the Reynolds number on the minimal energy threshold for generating turbulent bands ($E_{0_{min}}$), is analysed. According to previous works carried out on other shear flows in small domains, the minimal seed has been found to scale with Re following a power-law $E_{0_{min}} \propto Re^{-\gamma}$, although a sufficiently good fit is found only by restraining the analysis to $Re > 1000$. However, the value of γ recovered in the present work (≈ 8.5) is approximately fourth times larger than the values reported in previous works ($\gamma \approx 2.7$ in Duguet *et al.* (2013), $\gamma \approx 2$ in Cherubini *et al.* (2015)), probably due to the much larger size of the considered domain.

For all values of the Reynolds numbers analysed, the minimal-energy perturbation able to generate

turbulent bands is a spatially localised spot-like structure composed of finite-size streaks and elongated vortices. A more marked localization of the minimal seed is found when Re increases. As previously reported for the channel flow in the presence of spatially-localised spots, a large-scale flow having a quadrupolar structure has been found to surround the small-scale localised minimal perturbations. These minimal perturbations have dominant wavelengths ≈ 4 and ≈ 1 in the streamwise and spanwise directions, respectively. Nonlinear optimal perturbations with energy higher than minimal, are characterized by similar shapes and wavenumbers.

The evolution of the minimal seeds towards the turbulent bands has been investigated. For $Re < 1250$, the minimal seeds evolve in time creating an isolated oblique band. Whereas, for $Re \geq 1250$, it gives rise to two distinct bands which grow quasi symmetrically in the spanwise direction. This quasi symmetrical evolution is observed also at lower Re for non-minimal optimal perturbations.

An analysis of the production and dissipation of kinetic energy integrated over the streamwise and wall-normal directions shows that in all cases the initial spot-like perturbation evolves in a quasi symmetric fashion, giving rise to two proto-bands at the edges of the large-scale flow characterizing the minimal seeds. However, since the probability of decay of the bands increases in time and is higher for low Reynolds number, when Re is sufficiently low one of these bands rapidly dies out, leading to the development of one isolated band. Whereas, for larger values of Re, the probability of decay of an initial band is lower, while the probability of splitting increases. Thus, both oblique bands originating at the sides of the minimal seed survive for a longer time, until they split and interact, rapidly leading to the establishment of a spatio-temporally complex final state. Injecting more initial energy at low value of Re has the same effect of increasing Re, since a more spatially-extended disturbance with higher kinetic energy is reached at a small time, leading to longer and more energetic proto-bands, able to be sustained for a longer time.

This work elucidates two (apparently distinct) minimal-energy mechanisms for the generation of turbulent bands in channel flow. It appears that both the initial and the final states are very sensitive to the energy and Reynolds numbers characterising the flow, highlighting the complexity of the laminar-turbulent patterned state and its initial seed. The selection of one of these two mechanisms appears to be affected by the probability of decay of the newly-created stripe, which increases with time but decreases with the Reynolds number. These analyses suggest that the turbulent band formation is a complex phenomenon, very sensitive to the initial flow conditions. The mechanisms involved in the

origin of these bands are still not sufficiently clear, and deserve to be analysed in detail in a simplified configuration. For this reason, in the next chapter, we investigate the energy growth mechanism in a tilted domain allowing the growth of a single inclined band. The goal is to investigate a possible link between linear and nonlinear optimal growth mechanisms in the tilted domain and the origin of turbulent bands in channel flow.

Chapter 4

Linear and nonlinear optimal growth mechanisms for generating turbulent bands

Contents

In the previous chapter, we have sought the perturbations with the minimal energy able to generate turbulent bands; now we search for the main mechanisms at the origin of the turbulent bands and we aim to elucidate the possible link between transient energy growth mechanisms and the generation and sustaining of turbulent bands in channel flow. We search for linear and nonlinear optimal perturbations to unveil the main mechanisms allowing the creation of a turbulent band in a channel flow. To reduce the problem complexity the analysis is restrained to a tilted domain allowing the generation of a single localised turbulent band, as previously done in direct numerical simulations by Tuckerman *et al.* (2014).

A common assumption regarding the origin and growth of the turbulent band is that the oblique streak generation at the head of the turbulent band is responsible for the self-sustaining process of a single turbulent band (Shimizu & Manneville, 2019), and Xiao & Song (2020) confirmed that an inflectional spanwise instability is found at the head of the turbulent band. On the other hand, some authors suggest that a large-scale flow is necessary to sustain the turbulent band (Tao *et al.*, 2018) and is responsible for the turbulent band oblique evolution (Duguet & Schlatter, 2013).

In this part of the thesis work, we will demonstrate that, in order to trigger turbulence in the form of

turbulent bands in a tilted domain, two main elements are needed: a linear energy growth mechanism such as the lift-up for generating large-amplitude flow structures which produce inflection points; large-scale vortices ensuring spatial localisation due to nonlinear effects.

4.1 Problem formulation

For reducing the problem complexity and the computational cost, a tilted domain is considered for analysing oblique turbulent bands in plane Poiseuille flow, as previously done by Barkley & Tuckerman (2005, 2007) for plane Couette flow and by Tuckerman *et al.* (2014) for plane Poiseuille flow. Starting from the classical plane Poiseuille flow, $\mathbf{U}_P = [U_P(y), 0, 0]^T$, with $U_P(y) = 1 - y^2$, defined in the coordinate system $\mathbf{x}' = (x', y', z')^T$, where x' indicates the direction of the flow U_P, the tilted domain is obtained by applying the following change of reference:

$$\hat{\mathbf{e}}_x = cos\theta\hat{\mathbf{e}}_{x'} - sin\theta\hat{\mathbf{e}}_{z'}, \qquad \hat{\mathbf{e}}_y = \hat{\mathbf{e}}_{y'}, \qquad \hat{\mathbf{e}}_z = -sin\theta\hat{\mathbf{e}}_{x'} + cos\theta\hat{\mathbf{e}}_{z'},$$

$\mathbf{x} = (x, y, z)^T$ being the tilted domain coordinate system, and θ being the angle of the new coordinates system, corresponding to the angle of a turbulent band free to evolve in the non-tilted domain.
The dynamics of the turbulent bands in the tilted domain can be described by decomposing the instantaneous field into a perturbation $\mathbf{u}' = [u', v', w']^T$ and a laminar base flow $\mathbf{U} = [U(y), 0, W(y)]^T$, with $U(y) = U_P(y)cos\theta$ and $W(y) = U_P(y)sin\theta$. The perturbation dynamics is governed by the Navier-Stokes equations for incompressible flows, written in a perturbative form with respect to the base flow:

$$\frac{\partial u_i'}{\partial x_i} = 0, \qquad \frac{\partial u_i'}{\partial t} + u_j'\frac{\partial u_i'}{\partial x_j} + u_j'\frac{\partial U_i}{\partial x_j} + U_j\frac{\partial u_i'}{\partial x_j} = -\frac{\partial p'}{\partial x_i} + \frac{1}{Re}\frac{\partial^2 u_i'}{\partial x_j}, \tag{4.1}$$

with p' the pressure perturbation and $Re = U_c h/\nu$ the Reynolds number defined using the centreline velocity of the laminar Poiseuille flow, U_c, the half width of the channel, h, and the kinematic viscosity ν.
In order to find the optimal solution able to trigger turbulent bands in the tilted domain, we have computed linear and nonlinear optimal perturbations (Cherubini *et al.*, 2010*a*; Pringle *et al.*, 2012). In both cases, we choose as objective function the energy gain $G(T) = E(T)/E(0)$, where $E(t) = 1/(2V)\int u_i^2(t)dV$, $E(T)$ and $E(0)$ being the kinetic energy at the chosen target time and at the initial time, respectively. Thus, we search for the initial perturbation $\mathbf{u}'(0)$ providing the largest possible energy at fixed target time with an optimization loop based on the Lagrange multiplier technique

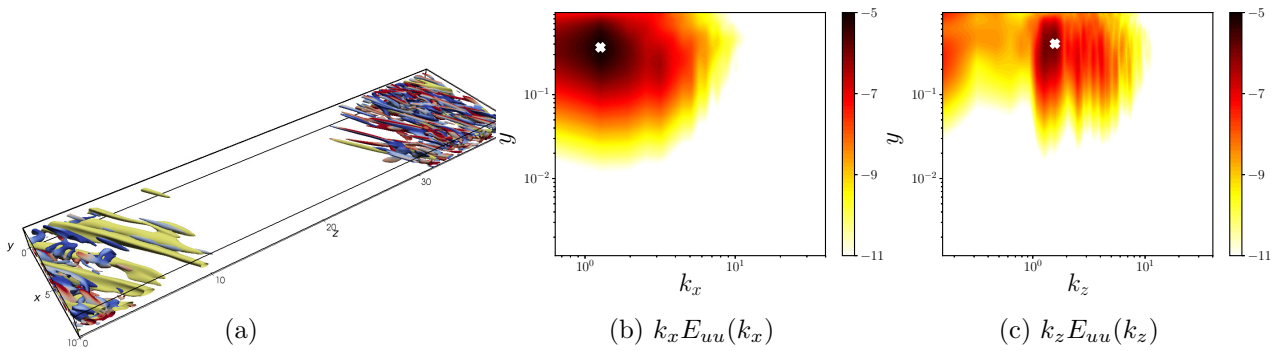

(a) (b) $k_x E_{uu}(k_x)$ (c) $k_z E_{uu}(k_z)$

Figure 4.1: (a) Isosurface of negative streamwise velocity ($u = -0.16$, yellow) and Q-criterion ($Q = 0.05$) coloured by the streamwise vorticity (positive red, negative blue) of a turbulent-laminar pattern at $Re = 1000$ in a domain tilted with $\theta = 35°$. (b-c) Logarithm of the premultiplied spectral energy versus the wall-normal distance y for the instantaneous field in (a). The white 'X' symbols indicate the energy peaks.

(Cherubini *et al.*, 2011). Linear optimization is carried out using an in-house Matlab code, whereas nonlinear optimization is implemented within the open source code *Channelflow* (channelflow.ch) (Gibson *et al.* (2021)).

For all the simulations the volume flux is kept constant imposing the bulk velocity equal to $U_{bulk} = 2/3$. The same domain size and spatial discretization used by Tuckerman *et al.* (2014) is adopted, namely $L_x \times L_y \times L_z = 10 \times 2 \times 40$ discretized on $N_x \times N_y \times N_z = 128 \times 65 \times 512$ grid. All computations are performed at $Re = 1000$, for which Tuckerman *et al.* (2014) have reported a persisting turbulent-laminar patter in the form of a single band. The angle of the tilted domain, θ, is chosen equal to 35° in accordance with that numerically observed at $Re = 1000$ by Kashyap *et al.* (2020) in large domains.

4.2 Results

At first, a Direct Numerical Simulation (DNS) is performed at $Re = 1000$ in the tilted domain. In figure 4.1a, a snapshot of the perturbation field is shown. As previously done by other authors, the DNS is initialised with a Reynolds number for which turbulence occupies the whole domain. Then, the Reynolds number is reduced slowly until $Re = 1000$, reaching the laminar-turbulent pattern shown in figure 4.1a. As already discussed by Tuckerman *et al.* (2014) for a tilted domain with the same size and Reynolds number, the turbulent state appears in the form of one turbulent band. In the instantaneous field, oblique wave-like structures such as alternating low- and high-speed streaks, are observed within the turbulent band and at its head. As expected, these structures present an angle

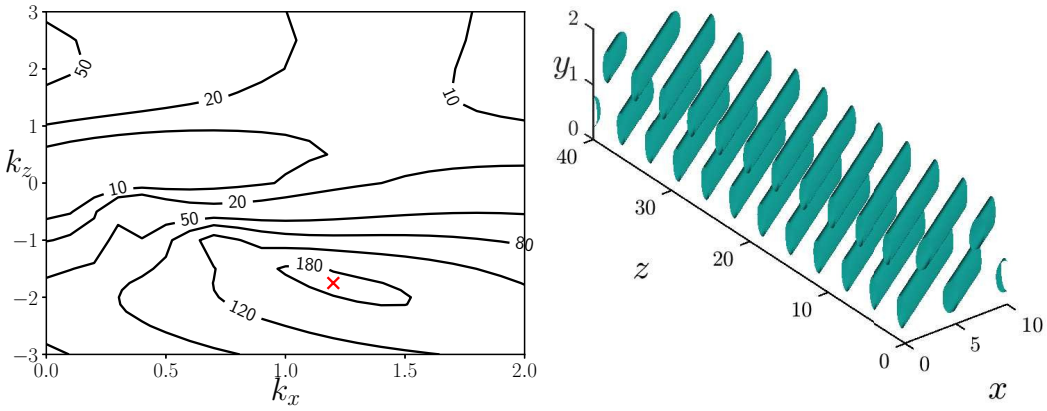

(a) (b)

Figure 4.2: (a) Contours of the optimal gain G as a function of the streamwise (k_x) and spanwise (k_z) wavenumbers, for $Re = 1000$ in the domain tilted with angle $\theta = 35°$. The red cross indicates the optimal growth G_{opt}. (b) Streamwise velocity component of the initial optimal perturbation for $T = T_{opt} = 73.11$, $k_x = 1.2$, $k_z = -1.75$.

with respect to the streamwise direction comparable to that of the base flow, and resemble the streaks observed at the head of a turbulent band in large (non-tilted) domains (Shimizu & Manneville, 2019; Liu *et al.*, 2020). Inspecting the premultiplied energy spectra of the streamwise instantaneous velocity provided in figure 4.1b, 4.1c, we found an energy peak at $k_x \approx \pm 1.27$, $k_z \approx \pm 1.6$. Thus, as discussed above, the flow is dominated by oblique structures with angle $\approx \arctan(k_x/k_z) \approx \pm 38°$.

In order to understand the origin of these oblique structures and the main mechanisms responsible for the generation of a turbulent band, a linear optimization of perturbations in the tilted domain is first performed. Since the base flow varies only in the wall-normal direction, the kinetic energy of the perturbations, constrained by equations (4.1) linearized with respect to the base flow, is optimized using a local approach, where the perturbation is assumed to be sinusoidal in the streamwise and spanwise direction, with given wavenumbers k_x and k_z, respectively. The linear optimization problem was solved at $Re = 1000$ for streamwise and spanwise wavenumbers in the range $0 < k_x < 2$, $-3 < k_z < 3$. In figure 4.2a, is provided the variation of the optimal gain with the spanwise and streamwise wavenumbers. The maximum growth is achieved at the optimal target time $T_{opt} = 74.6$, for $k_x = 1.19$ and $k_z = -1.71$, leading to an optimal gain $G_{opt} = 196.07$. As should be expected, the optimal gain, time and wavenumbers are very close to those found by Reddy & Henningson (1993) for the plane Poiseuille flow, once reported to a tilted domain. Notice also that similar values of streamwise and spanwise wavenumbers are found by Xiao & Song (2020) performing a linear stability analysis around

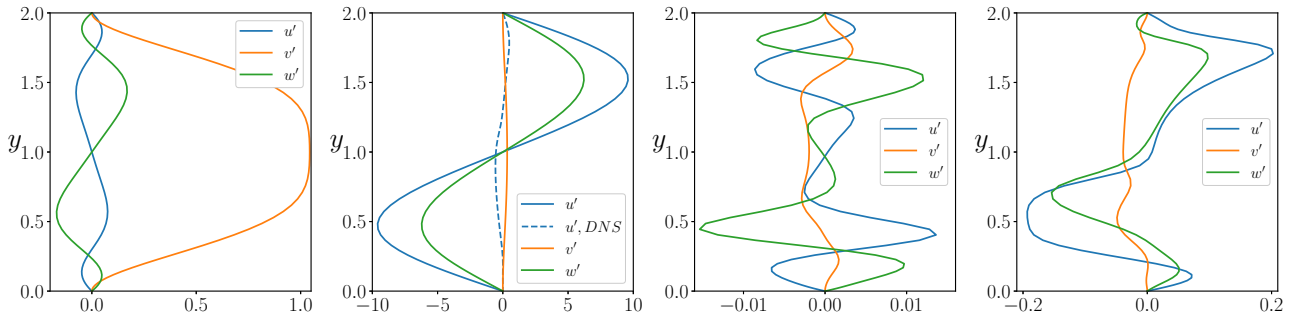

(a) Linear, $t = 0$ (b) Linear, $t = T_{opt}$ (c) Nonlinear, $t = 0$ (d) Nonlinear, $t = T$

Figure 4.3: Velocity profiles of the optimal disturbances (continuous lines). (a-b) Linear optimal for $k_x = 1.19$, $k_z = -1.71$ at (a) $t = 0$ and (b) $T_{opt} = 74.6$. The dashed line represents the streamwise velocity profile recovered at $x = 0$, $z = 10$ by evolving to $t = 5$ by DNS the localized initial optimal perturbation of figure 4.6. (c-d) Nonlinear optimal at the minimal energy able to trigger turbulence, $E_0 = 2.1 \times 10^{-5}$ at (c) $t = 0$ and (b) $T = 10$.

the mean flow of a region at the head of the turbulent band. Moreover, the optimal streamwise and spanwise wavenumbers are very close to the ones for which the premultiplied energy spectra in figure 4.1b, 4.1c peak. Thus, these optimal perturbations can be linked to the oblique waves observed at the head of the turbulent band. As shown in figure 4.2b, the linear optimal perturbation is oblique with angle $\arctan(k_x/k_z) \approx -34.5°$, and modulated in both streamwise and spanwise directions. This had to be expected since the base flow presents a spanwise component, in analogy with the shear flow developing on a swept-wing, whose unstable modes and optimal perturbations are characterised by cross-flow vortices, namely three dimensional oblique vortical perturbations with negative spanwise wavenumber. As shown in figure 4.3a, at $t = 0$ the optimal perturbation presents counter-rotating vortices with a large wall-normal component, which decreases in time towards the target time (see figure 4.3b), while the streamwise and spanwise ones strongly increase creating oblique streaks. The mechanism creating these oblique energetic structures is based on the transport of the wall-normal shear of both streamwise and spanwise component of the base flow, which may be seen as a tilted counterpart of the lift-up effect.

The linear optimal perturbation computed for T_{opt} is then injected onto the laminar flow in the tilted domain with different values of the initial energy $E(0)$, in order to verify whether such a linear transient-growth mechanism could induce transition in the form of turbulent bands. In figure 4.4, the energy evolution in time is reported for the linear optimal perturbations with different initial energies (black lines). The perturbation with unitary energy norm is the only one able to induce the

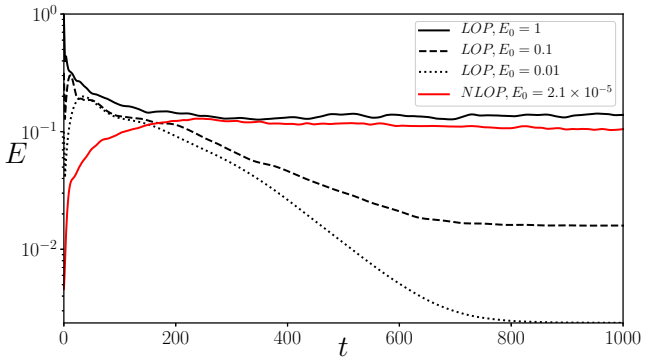

Figure 4.4: Kinetic energy time evolution for the linear optimal perturbation with $E_0 = 0.01.0.1, 1$ (black lines) and for the nonlinear one (red line) for $E_0 = 2.1 \times 10^{-5}$.

formation of the turbulent band, while the others lead to relaminarisation. However, it is observed that turbulence is at first triggered in the whole domain and successively localises in a band. This is mostly probably due to the fact that the linear optimal disturbance is not spatially localized but occupies the whole domain, which also explains the large amount of energy needed for triggering turbulence by means of this optimal mechanism. To provide spatial localization of the optimal perturbation, aiming at triggering the turbulent band, we extended the optimization to the fully nonlinear equations, which usually provide a consistent spatial localization (Kerswell, 2018; Cherubini *et al.*, 2010*a*; Farano *et al.*, 2015). Notice that the nonlinear optimization is performed in a fully three-dimensional framework, without any hypothesis on the perturbation wavenumbers.

Nonlinear optimization has been performed in the tilted domain for several initial energies and target time $T = 10$, which is close to the characteristic eddy turnover time of structures in the buffer layer, for which optimal streaks having the typical spanwise spacing of approximately 100 wall units were recovered by Butler & Farrell (1993). For this target time, the nonlinear optimal perturbation triggers localised turbulence already for $E_0 \geq 2.1 \times 10^{-5}$. The nonlinear optimal perturbation at the minimal input energy able to trigger turbulence is shown in figure 4.5 (a-b). As expected from previous works (Cherubini *et al.*, 2011; Monokrousos *et al.*, 2011; Pringle *et al.*, 2012), it is localised in the longitudinal direction. Furthermore, it presents remarkable similarities with the edge state found by Paranjape *et al.* (2020) in a tilted domain for $Re = 760$. In figure 4.5a the isocontours of the wall-normal perturbation are reported, together with the normalised y-integrated large-scale flow $\overline{u_i} = \int_{-1}^{1} u_i dy$. One can observe a small-scale flow within a localised region, where the turbulent band will be generated, together with two larger-scale vortices surrounding this region, having opposite direction upstream and downstream

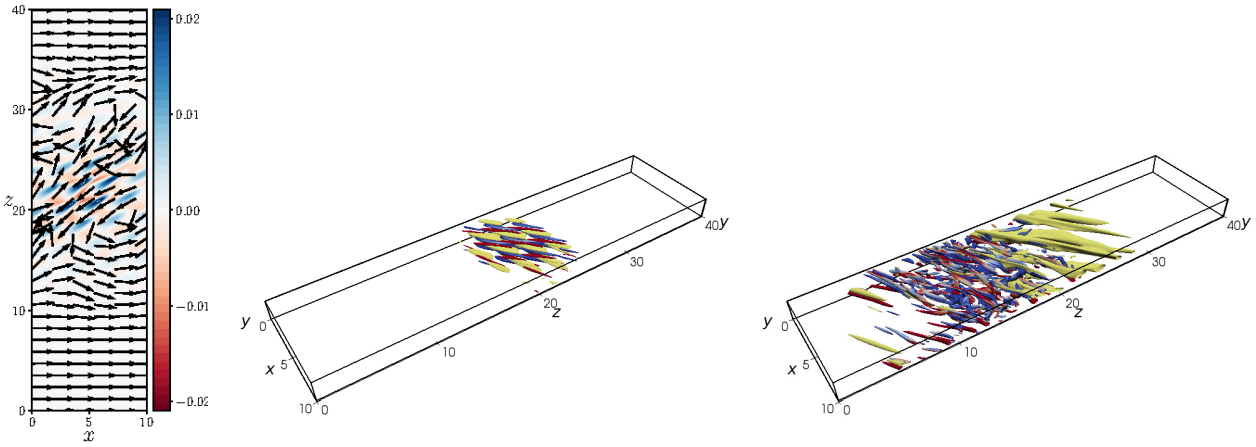

(a) 2D, $t = 0$ (b) 3D, $t = 0$ (c) 3D, $t = 600$

Figure 4.5: Nonlinear optimal perturbation for $Re = 1000$, $E_0 = 2.1 \times 10^{-5}$, $T = 10$. (a) Shaded isocontours of the wall-normal perturbation and vectors of the y-integrated flow in the $y = 0.25$ plane at $t = 0$. (b-c) Isosurface of negative streamwise velocity (yellow) and Q-criterion coloured by the streamwise vorticity (positive red, negative blue) for (b) $t = 0$, $u = -0.01$, $Q = 0.02$; (c) $t = 600$, $u = -0.16$, $Q = 0.05$.

of the localised perturbation. A large-scale vortical flow surrounding the region developing into a turbulent spot has been previously reported by several authors in both tilted and non-tilted domains. The three-dimensional visualization in figure 4.5b shows that the small-scale flow is constituted by oblique streaks flanked by counter-rotating vortices. The streaks are aligned with the base flow, presenting an angle of approximately 35° with respect to the streamwise direction, in accordance with the angle of the linear optimal perturbation. As expected, this localised optimal perturbation evolves in time towards a turbulent band, as shown in figure 4.5c. Notice that the nonlinear optimal perturbation induces transition for an initial energy five orders of magnitude lower than that of the linear optimal one; this cannot be exclusively due to its spatial localisation. In fact, the wall-normal velocity profiles provided in figure 4.3c present strong differences with respect to their linear counterpart shown in figure 4.3a. In particular, as typically observed in nonlinear optimal perturbations (Cherubini *et al.*, 2011), the streamwise velocity component is now of the same order of magnitude than the other ones, and the wall-normal component strongly changes. At target time (figure 4.3d) deformed streaks are obtained, presenting inflection points which might be linked to the inflectional instability discussed in Song & Xiao (2020).

To isolate the effect of spatial localisation from the strong changes in the velocity profiles induced by the nonlinear effects, we enforced localisation in the z direction on the three-dimensional linear

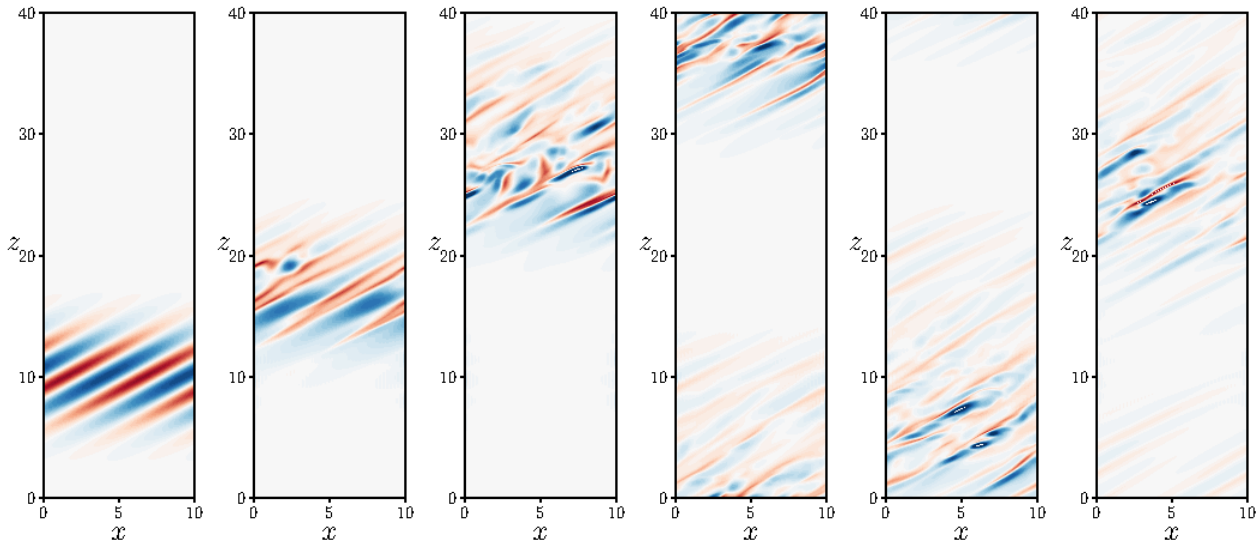

(a) $t = 0$ (b) $t = 20$ (c) $t = 50$ (d) $t = 80$ (e) $t = 100$ (f) $t = 150$

Figure 4.6: Time evolution of the localised linear optimal perturbation at different times: shaded contours of the wall-normal velocity at $y = 0.25$.

optimal solution shown in figure 4.2b. This is achieved by multiplying the velocity components for a normal distribution having the form:

$$f(z) = e^{-\frac{1}{2}\frac{(z-z_0)^2}{\sigma^2}},$$

where $z_0 = 10$ represents the value at which the perturbation should be centered, and $\sigma = 2.5$ is its standard deviation.

This localised perturbation is injected in the DNS with different initial energies. Its time evolution for the minimal initial energy able to induce turbulent bands, i.e., $E_0 = 3.3 \times 10^{-3}$, is reported in figure 4.6. At first, the oblique streaks increase their amplitude ($t = 20$) and start to saturate nonlinearly, until secondary instability arises ($t = 50$) and triggers turbulence in a localised zone within the laminar flow ($t = 80 - 100$). At $t = 150$, the flow presents the same configuration shown in figure 4.1 for a turbulent band generated by decreasing the Reynolds number starting from a fully turbulent velocity field. Notably, inflection points similar to those observed in figure 4.3d, are observed at small time in the velocity profiles (see the dashed line on figure 4.3b). Thus, it appears that for triggering a turbulent band in the tilted domain, starting from a rather weak perturbation, two main elements are needed: small-scale oblique streaks aligned with the baseflow, that saturate creating inflection points, and a large-scale vortical flow ensuring spatial localisation in the z direction. The transition at the

small-scale is due to the classical lift-up mechanism, followed by secondary instability of the saturated streaks, which triggers the self-sustained cycle supporting turbulence (Hamilton *et al.*, 1995; Waleffe, 1997). However, in the absence of a large-scale flow ensuring localisation and maintaining the band, these mechanisms are not sufficient to generate localised turbulence. Of course the initial phase of growth due to the lift-up mechanism can be skipped by directly feeding the flow with inflection points, as done by Song & Xiao (2020), but at the cost of a larger amplitude disturbance, which can be more difficult and expensive to obtain in an experimental setup.

Finally, we should verify whether this artificially-localised perturbation able to optimally produce streaks, can generate turbulent bands also in large, non-tilted domains, where no angle is imposed a priori. Thus, we have reported the artificially-localised linear optimal perturbation computed in the tilted domain, in a very large (non-tilted) domain of size $L_{x'} \times L_{y'} \times L_{z'} = 250 \times 2 \times 125$, and let it evolve freely by a DNS.

As shown in figure 4.7, despite the fact that at $t = 0$ a large-scale flow is present only in the vicinity of the perturbation, at $t = 100$ a clear quadrupolar large-scale vortical structure, filling the whole domain, is observed. Notice that, as discussed in Wang *et al.* (2020), a quadrupolar structure arises in the presence of a negative spanwise vorticity generated near the walls inside a spot, as a consequence of the shearing of the streamwise velocity and the breaking of the spanwise homogeneity. New streaky structures, generated by the self-sustained process triggered by the optimal counter-rotating vortices and streaks, are then created following the shear layer between two of the previously observed large-scale vortices ($t = 300$), finally creating a clear turbulent band ($t = 800$). Despite not being optimal for this large, non-tilted domain, this perturbation is able to generate a large-scale flow that promotes the formation of small-scale streaks in an oblique direction, consequently inducing the band formation. The optimization of perturbations in this large non-tilted domain is beyond the scope of the present work, and is treated in detail in Parente *et al.* (2021*a*), where the minimal-energy optimal perturbations able to generate turbulent bands are computed and discussed for different values of Re.

4.3 Conclusion

In this chapter, we have investigated the energy growth mechanisms involved in the laminar-turbulent transition in the form of turbulent bands using linear and nonlinear optimization. We have considered a plane Poiseuille flow at $Re = 1000$ in a tilted domain with angle $\theta = 35°$ that ex-

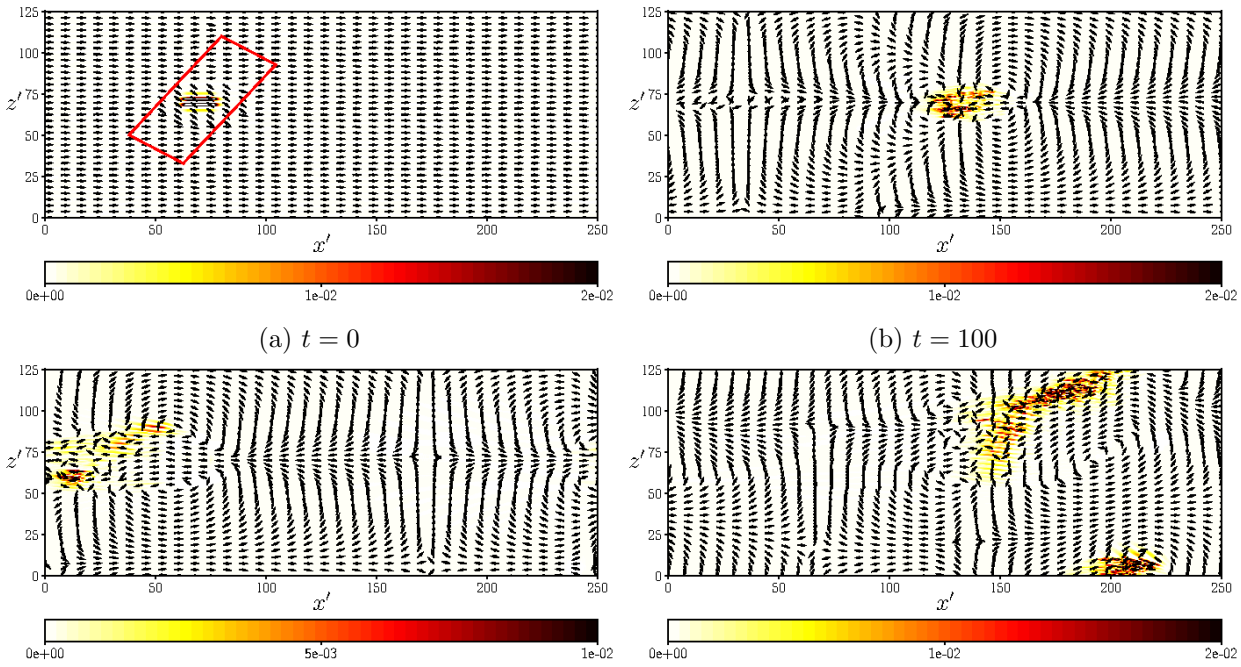

(a) $t = 0$ (b) $t = 100$

(c) $t = 300$ (d) $t = 800$

Figure 4.7: Time evolution of the localised linear optimal perturbation reported in a large domain: contours of the wall-normal velocity and vectors of the large-scale flow $(\overline{u}, \overline{w})$.

hibits a single turbulent band. Linear optimizations have reported that the optimal perturbation is three-dimensional and aligned with the oblique baseflow, in the form of low- and high-speed streaks modulated in the streamwise and spanwise directions with $k_x = 1.2$ and $k_z = -1.75$. Similar wavenumbers are found at the same Reynolds number by direct numerical simulation and by linear stability analysis at the head of the turbulent band, where an angle comparable to that of the optimal streaks is observed.

However, the linear optimal perturbation needs a very large initial energy to trigger turbulence, which spreads in the whole domain. Using nonlinear optimization, a localized turbulent band is triggered for an initial energy five orders of magnitude weaker, $E_0 = 2.1 \times 10^{-5}$. The nonlinear optimal perturbation is characterised by a localised small-scale flow and a large-scale flow surrounding it. The small-scale flow is composed of oblique counter-rotating vortices and streaks with an angle comparable to that found via linear optimization, which develops inflection points at the target time.

To isolate the influence of large-scale flow and localization from that of the small-scale structures, we have constructed a localized perturbation by artificially confining the linear optimal to a localized re-

gion in the spanwise direction and injected it on the laminar flow both in the tilted and in a non-tilted, very large domain. In both domains, a turbulent band is created.

These results suggest that transition to a turbulent band might arise due to the optimal lift-up mechanism when coupled with a large-scale vortical flow intimately linked to the spatial localisation of the disturbance. This energy growth mechanism provides high-amplitude streaks developing inflection points when saturating nonlinearly, but since the optimal streaks are aligned with the base flow, they cannot generate a turbulent band by themselves. However, the large-scale flow generated by the spatial localisation of the perturbation provides the preferential direction of spreading of the streaks generated by the lift-up mechanism and is thus necessary to trigger turbulence in the form of turbulent bands.

Chapter 5

Nonlinear optimal perturbations in turbulent channel flow

Contents

In the previous Chapter, we have shown that nonlinear optimal perturbations are able to provide the main mechanisms leading to the formation of turbulent bands in plane Poiseuille flow. When considering fully-developed (non-patterned) turbulent flows, nonlinear optimal perturbations might provide crucial information about the interaction of energetic structures at different scales, and the related mechanisms of energy exchange and production, as previously shown by Farano *et al.* (2017, 2018). Using the perturbative Reynolds-Averaged Navier-Stokes equations (PRANS), Farano *et al.* (2017, 2018) have found nonlinear optimal perturbations characterised by hairpin vortices originated by the breakup of the near-wall streaks for low values of friction Reynolds number. While, at slightly higher friction Reynolds numbers, the nonlinear optimal perturbation mostly consists in large-scale and small-scale streaks. Moreover, these nonlinear optimal perturbations may reproduce high-energetic events, such as ejections and sweeps, recurrently observed in wall-bounded turbulent flows (Farano *et al.*, 2017). Following these works, with the aim of characterising the turbulent motions at even higher Reynolds number, we extend in this Chapter the nonlinear optimization problem used in the previous Chapters to the perturbative Reynolds-Averaged Navier-Stokes (PRANS) equations (eq (2.3)). Performing nonlinear turbulent optimizations at short target times (typical of the eddy turnover time

of small-scale coherent structures), Farano *et al.* (2017, 2018) have found that the optimal solutions presents the characteristic of the wall motion. In contrast, when the optimizations are carried out for a time scale associated with the eddy turnover time of large-scale motions, the nonlinear optimal perturbations appear to be characterized by large-scale structures. In particular, for low friction Reynolds number, the nonlinear optimal perturbation is represented by hairpin vortices originated by the breakup of the near-wall streaks; whereas, at higher friction Reynolds number, large-scale streaks are observed. In this chapter, we have reproduced the results reported by Farano *et al.* (2017) at $Re_\tau = 180$ and we have further analysed the influence of the target time on the nonlinear optimal perturbation.

5.1 Problem formulation

The flow considered is a fully turbulent channel flow at $Re_\tau = 180$. The dynamics of this flow is studied by using the Reynolds decomposition, i.e. decomposing the instantaneous velocity field, $\mathbf{u} = [u, v, w]^T$, into the mean flow $\overline{\mathbf{U}} = [\overline{U}(y), 0, 0]$ and a fluctuation $= [\tilde{u}, \tilde{v}, \tilde{w}]^T$. The dynamics of the fluctuation of the mean turbulent flow is computed by solving the perturbative Reynolds-Averaged Navier-Stokes (PRANS) equations:

$$\begin{cases} \nabla \cdot \tilde{\mathbf{u}} = 0 \\ \dfrac{\partial \tilde{\mathbf{u}}}{\partial t} = -(\tilde{\mathbf{u}} \cdot \nabla)\tilde{\mathbf{u}} - (\tilde{\mathbf{u}} \cdot \nabla)\overline{\mathbf{U}} - (\overline{\mathbf{U}} \cdot \nabla)\tilde{\mathbf{u}} - \tilde{\nabla} p + \dfrac{1}{Re}\nabla^2 \tilde{\mathbf{u}} + \nabla \cdot \overline{\tilde{\mathbf{u}}\tilde{\mathbf{u}}}, \end{cases} \tag{5.1}$$

where the mean flow and the Reynolds stress tensor $\overline{\tilde{\mathbf{u}}\tilde{\mathbf{u}}}$ are approximated with an analytical expression for mean flow and Reynolds stress tensor given by the PRANS equations, reported in the section 2.1.2. The aim of this chapter is to find the nonlinear optimal perturbation in turbulent channel, i.e. we search for the initial perturbation $\tilde{\mathbf{u}}(0)$ that provides the maximum value of the objective function at the chosen target time T. The chosen objective function is the energy gain $G(T) = E(T)/E(0)$, where:

$$E(t) = \frac{1}{2}\int_V (u'(t)^2 + v'(t)^2 + w'(t)^2) dV \tag{5.2}$$

is the kinetic energy at time t and V is the volume of the computational domain. In order to find the initial perturbation $\tilde{\mathbf{u}}(0)$ having given initial energy $E(0) = E_0$, providing the largest possible energy $E(T)$ at the target time, an optimization loop is set using the Lagrange multiplier technique. The Lagrangian functional is defined imposing the following constraints: i) the optimal perturbation $\tilde{\mathbf{u}}(t)$

must be solution of the perturbative Reynolds-Averaged Navier-Stokes equations at all times $t \in]0, T[$; ii) it must be divergence free at all times $t \in [0, T]$; and iii) it must have energy norm equal to a given value E_0 at $t = 0$. With these constraints, the Lagrangian functional reads:

$$\mathcal{L}(\tilde{u}_k, \tilde{p}, u_k^\dagger, p^\dagger, \tilde{u}_k(0), \tilde{u}_k(T), \lambda) = \frac{E(T)}{E(0)} - \int_0^T \int_V u_i^\dagger \left(\frac{\partial \tilde{u}_i}{\partial t} + \frac{\partial(\tilde{u}_i \tilde{u}_j)}{\partial x_j} + \frac{\partial(\overline{U}_i \tilde{u}_j)}{\partial x_j} + \frac{\partial(\tilde{u}_i \overline{U}_j)}{\partial x_j} + \frac{\partial \tilde{p}}{\partial x_i} - \frac{1}{Re} \frac{\partial^2 \tilde{u}_i}{\partial x_j} - \frac{\partial \overline{\tilde{u}_i \tilde{u}_i}}{\partial x_j} \right) dV dt - \int_0^T \int_V p^\dagger \frac{\partial \tilde{u}_i}{\partial x_i} dV dt - E^\dagger \left(\frac{E_0}{E(0)} - 1 \right). \tag{5.3}$$

with $\mathbf{u}^\dagger$, $p^\dagger$ and $E^\dagger$ being the Lagrangian multipliers (or adjoint variables). To maximise the augmented functional $\mathcal{L}$ we evaluate its variation with respect to the direct and adjoint variables and nullify it. The variation of the Lagrangian functional with respect to the direct variables $\mathbf{u}'$, p', provides the same adjoint equations found for the laminar flow 2.12d and 2.12e. The optimization problem is then solved using a direct-adjoint looping algorithm explained in section 2.2.

First, we have reproduced the results reported by Farano *et al.* (2017) at $Re_\tau = 180$ for two target times: $T = 8.16$ corresponding to one eddy turnover time evaluated in the buffer layer (inner optimization time $T_{in}^+ = 80$) and $T = 31.12$, corresponding to one eddy turnover time at the center of the channel (outer optimization time T_{out}^+). Secondly, the optimization procedure is performed at different target time to analyse the influence of the time on the structures of the nonlinear optimal perturbation.

The optimization problem is performed maximising the kinetic energy with fixed input energy equal to $E_0 = 10^{-2}$. The domain size in the streamwise, wall-normal and spanwise directions is $L_x \times L_y \times L_z = 4\pi \times 2 \times 2\pi$, while the number of grid points in the same directions are $N_x \times N_y \times N_z = 192 \times 129 \times 160$. This results in a numerical resolution comparable with those used by Kim *et al.* (1987). Further, the computations are performed at $Re = 3300$ and at constant flow rate with bulk velocity $U_b = 0.8485$, which results in the friction Reynolds number $Re_\tau = 180$.

5.2 Results

In figure 5.1, the initial optimal perturbation obtained for the outer target time $T_{out}^+ = 305$ is shown together with its evolution. As in the reference work (Farano *et al.*, 2017), the initial optimal perturbation presents localised patches of streamwise velocity perturbation in the outer region and

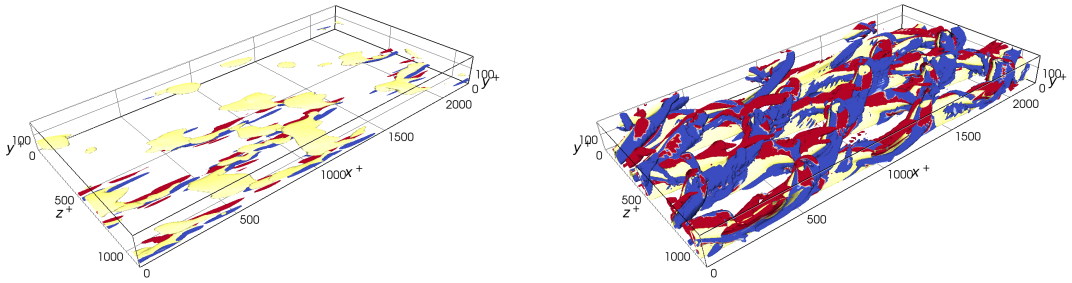

(a) $t^+ = 0$ (b) $t^+ = T^+_{out}$

Figure 5.1: Shape of the optimal perturbation for $T^+_{out} = 305$ and $E_0 = 10^{-2}$ at (a) $t^+ = 0$ and (b) $t^+ = T^+_{out}$. Isosurfaces of negative streamwise velocity (yellow, (a) $u = -0.016$, (b) $u = -0.3$). and Q-criterion coloured by the value of the streamwise velocity (positive blue, negative red).

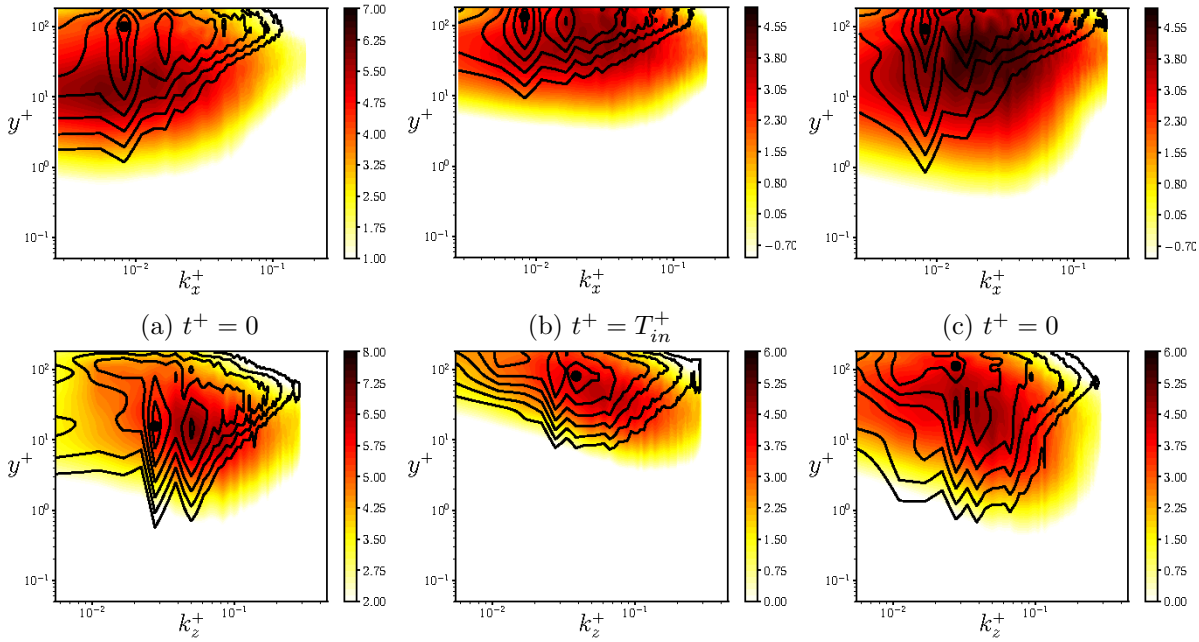

(a) $t^+ = 0$ (b) $t^+ = T^+_{in}$ (c) $t^+ = 0$

(d) $t^+ = T^+_{in}$ (e) $t^+ = T^+_{in}$ (f) $t^+ = T^+_{in}$

Figure 5.2: Logarithm of the premultiplied power energy spectrum versus the wall-normal distance y^+ for the DNS (shaded contours) and the outer optimal solution (black isolines) at target time $T = T^+_{out} = 305$. The black dots indicate the maximum values for the outer peak.

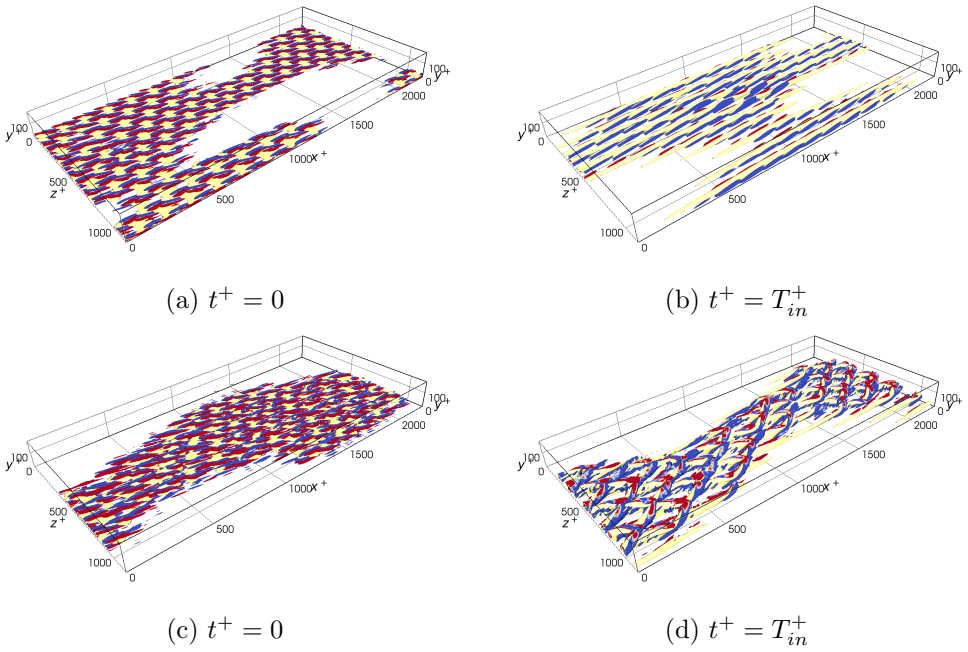

(a) $t^+ = 0$ (b) $t^+ = T_{in}^+$

(c) $t^+ = 0$ (d) $t^+ = T_{in}^+$

Figure 5.3: Shape of the optimal perturbation for $T_{in}^+ = 80$ and $E_0 = 10^{-2}$ at (a-c) $t^+ = 0$ and (b-d) $t^+ = T_{in}^+$. Isosurfaces of negative streamwise velocity (yellow, (a-c) $u = -0.025$, (b-d) $u = -0.18$) and Q-criterion coloured by the value of the streamwise velocity (positive blue, negative red).

streamwise vortices at the wall. At target time, the perturbation presents a much more complex structure composed of highly oscillating streamwise streaks and packets of hairpin vortices, which originate from the merging of the streamwise vortical structures flanking two neighboring low-speed streaks.
To investigate the size and the main wavelengths characterising this optimal perturbation, the streamwise and spanwise premultiplied energy density spectra for the nonlinear optimal solution at $T = T_{out}^+$ are reported in figure 5.2 and compared to the same spectra extracted from the DNS. The black dots mark the peak values of the energy density spectra for the outer optimal structures. The shape of the outer optimal energy spectra is very close to that of the DNS and presents peaks at a large wavelength in streamwise and spanwise directions. This indicates that the optimal perturbation computed for the outer target time is representative of the turbulent motions.

Searching for the optimal solution at the inner time and perturbing with different initial conditions, we have found two nonlinear optimal perturbations (see figure 5.3) with a very close energy gain listed in table 5.1. Both optimizations are stopped when the residual value fall below 5×10^{-7}. The solution in figure 5.3a is similar to those reported by Farano *et al.* (2017) and is found initialising the optimization procedure with an optimal perturbation at lower target time ($T \approx 2$). While the

	T	G_{opt}
Solution 5.3(a)	8.16	59.75
Solution 5.3(c)	8.16	59.10

Table 5.1: Energy gain values for the two solutions shown in figure 5.3.

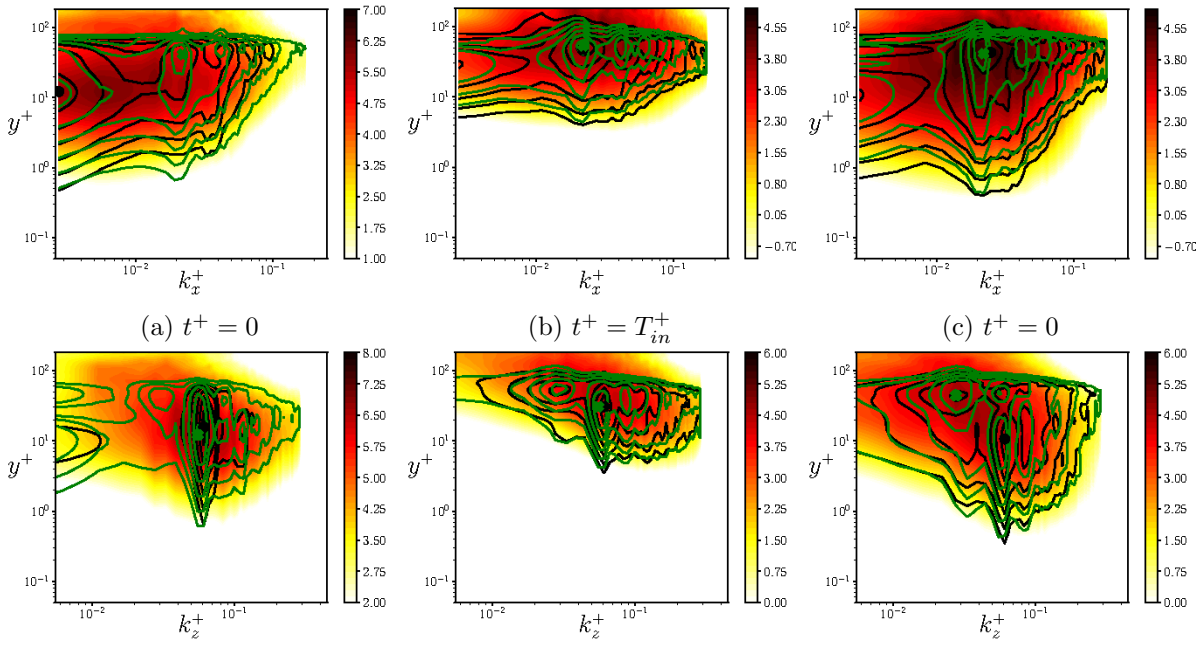

(a) $t^+ = 0$ (b) $t^+ = T_{in}^+$ (c) $t^+ = 0$

(d) $t^+ = T_{in}^+$ (e) $t^+ = T_{in}^+$ (f) $t^+ = T_{in}^+$

Figure 5.4: Logarithm of the premultiplied power energy spectrum versus the wall-normal distance y^+ for the DNS (shaded contours), the inner optimal solution with wall vortices (black isolines) and the inner optimal solution with hairpin vortices (green isolines) at target time $T = T_{in}^+ = 80$. The dot and 'X' symbols indicate the maximum values for the inner peak.

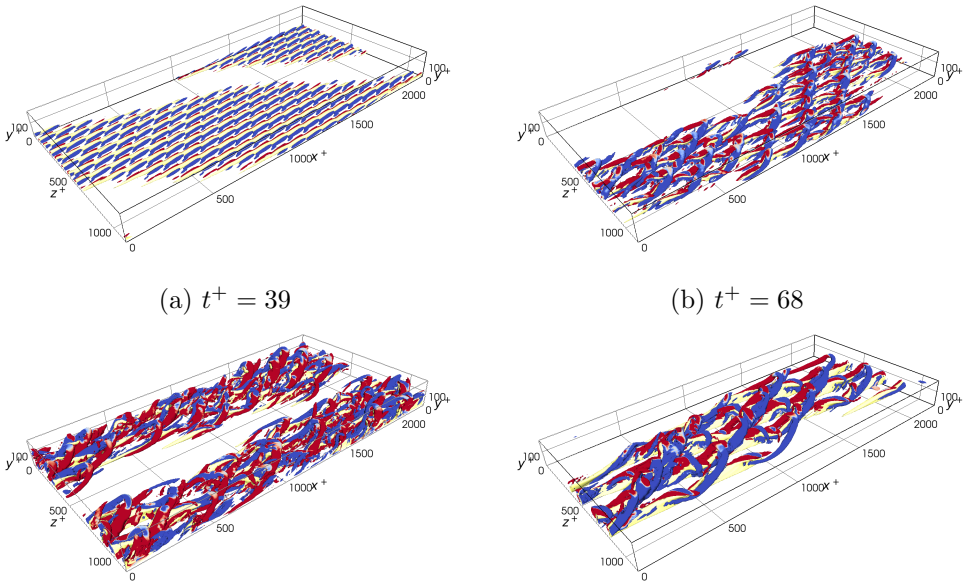

(a) $t^+ = 39$ (b) $t^+ = 68$

(c) $t^+ = 147$ (d) $t^+ = 196$

Figure 5.5: Shape of the optimal perturbation at different target time and $E_0 = 10^{-2}$. Isosurfaces of negative streamwise velocity (yellow) and Q-criterion coloured by the value of the streamwise velocity (positive blue, negative red).

solution in figure 5.3c is found initialising with different random solutions. This behaviour is linked to the nonlinear nature of the Navier-Stokes equations, that results in a nonconvex optimization problem for which multiple solutions, such as local maxima associated to very similar values of the gain, may emerge.

The initial optimal fluctuations in figure 5.3a and 5.3c present a similar shape with localised region of streamwise velocity flunked by inclined streamwise vortices, and at the target time, both solutions present modulated streaks with a spanwise wavelength of $\lambda_z \approx 100$. However, much more differences are identified in the streamwise vortices, in fact, the optimal perturbation in figure 5.3b presents inclined positive and negative streamwise vortices; whereas, the other perturbation presents packets of hairpin vortices.

Comparing the two optimal perturbations in terms of energy density, the recovered spectra appear to be similar (see figure 5.4). They present an energy peak at $\lambda_z = 110$ close to the wall, reproducing the typical spanwise streaks spacing (Kline *et al.*, 1967). Concerning the streamwise wavelength, a peak is identified at $\lambda \approx 270$. It is worth noticing that comparing, the spectra of the optimal perturbations computed for the two target times, the peaks move to higher values of y^+, indicating that the struc-

tures move to the center of the channel when the target time increases.

In order to analyse the influence of the target time on the nonlinear optimal solutions, we have performed the nonlinear optimal perturbations for four target times $T^+ = [39, 68, 147, 196]$. Figure 5.5 shows the optimal solutions at these target times. The optimal perturbations have similar characteristics to those presented previously. In particular, for the low target time ($T^+ = 39$) the optimal perturbation presents a shape similar to the optimal perturbation in figure 5.3a, i.e. low velocity streaks at the wall flanked by alternating vortices. Instead, for high target times $T^+ > 68$, highly modulated streaks with hairpin vortices are observed, which move towards the center of the channel when the target time increases.

5.3 Conclusion

The nonlinear optimal perturbations in turbulent channel at $Re_\tau = 180$ were investigated. In the first part, the results found by Farano *et al.* (2017) are reproduced and then, the analysis is extended to different target times. In particular, at this friction Reynolds number, two shapes of nonlinear optimal perturbation are identified: one with low velocity streaks at the wall flanked by oblique alternating vortices, and the other characterised by highly oscillating low velocity streaks with packets of hairpin vortices. Moreover, varying the target time, we have identified that the first solution presents a high "probability" to emerge at low target time; whereas, the latter is found for high target times. For an intermediate range of target time, both solutions may emerge. Further analysis needs to be performed initialising with different initial conditions and it is necessary to extend this analysis at higher friction Reynolds number to confirm this behaviour. However, despite the fact that the objective was to investigate the turbulent motions a high friction Reynolds numbers via nonlinear optimal perturbations, due to the multiple solutions found and the strong influence of the initial condition, we have chosen to follow a different approach, and try to characterise the turbulence coherent motion searching for statistically-steady coherent solutions. In the next chapter, we present a "new" mathematical framework to seek invariant solutions of the mean turbulent flow at high friction Reynolds number, without any filtering of small-scale structures.

Chapter 6

Continuing invariant solutions towards the turbulent channel flow

Contents

As introduced previously, the chaotic saddle which sustains turbulence consists of a variety of invariant solutions. However, to derive low-order models able to describe a fully developed three-dimensional turbulent flow, a large number of these solutions is necessary. The investigation of these solutions is usually carried out by searching for invariant solutions of the Navier-Stokes equations using Direct Numerical Simulations (DNS), but at high Reynolds numbers, the search of such invariant solutions becomes difficult, due to the multiple bifurcations that these solutions undergo.

Recently, in order to compute invariant solutions in turbulent Couette flow, Rawat *et al.* (2015) extended the research of invariant solutions to over-damped Large-Eddy Simulations (LES) with the Smagorinsky model. This approach was subsequently used by Hwang *et al.* (2016*b*) to search invariant solutions characterised by large- and very large-scale motions at high friction Reynolds number up to $Re_\tau = 1000$ in turbulent channel flow. This is done by controlling the strength of the filter with the Smagorinsky constant to quench the small-scale motion. This approach is well suited for investigating the self-sustained nature of coherent large-scale motion, as was first done for the channel Hwang & Cossu (2010*b*, 2011) and Couette Rawat *et al.* (2015, 2016) flows at relatively low Reynolds numbers and for the channel and asymptotic suction boundary layer flow at large friction Reynolds numbers

Hwang *et al.* (2016*b*); Azimi *et al.* (2020). However, this overfiltered approach does not help in investigating the nature of the energy transfer between coherent structures of different scales. Despite the fact that the motion at large scales can be sustained even when the wall cycle is quenched, in high-Reynolds-number turbulent flows multiple and non-trivial interactions exist between coherent structures at different scales Cimarelli *et al.* (2016); Cho *et al.* (2018). The understanding of these energetic bonds connecting structures of different scales in turbulent flows can be achieved by the computation of statistically-invariant coherent states which characterise the multiple-scale, coherent part of the motion around the turbulent mean flow, without any filtering of small-scale structures.
Towards this aim, in this chapter is provided a new mathematical framework for the computation of statistically invariant equilibria, travelling waves, or (relative) periodic orbits characterising the motion of turbulent fluctuations around the mean flow. This is achieved by seeking statistically invariant coherent solutions of the unsteady Reynolds-averaged Navier-Stokes (PRANS) equations written in a perturbative form with respect to the turbulent mean flow, using a suitable approximation of the Reynolds stress tensor. Unlike the classical invariant solutions of the Navier-Stokes equations, these solutions are sustained only in the presence of the Reynolds stress tensor, and are representative of the statistically coherent motion of turbulence. This set of equations has been found to be efficient for characterising extreme events having an energy spectrum very similar to that of the fully turbulent flow Farano *et al.* (2017, 2018). These solutions are found by setting up a continuation procedure of known solutions of the perturbative Navier-Stokes equations, based on the continuous increase of the turbulent eddy viscosity towards its turbulent value. For small friction Reynolds number and/or domain size, the statistically invariant motion is almost identical to the corresponding invariant solution of the Navier-Stokes equations. In contrast, for sufficiently large friction Reynolds numbers and/or domain size, it considerably departs from the starting invariant solution of the Navier-Stokes equations, presenting spatial structures such as streaks and streamwise vortices, main wavelengths, and scaling very close to those characterising both large- and small-scale motion of turbulent channel flows.

6.1 Problem formulation

The incompressible flow in a channel is governed by the Navier-Stokes equations, which describe the dynamics of the instantaneous state variables $\mathbf{q} = [\mathbf{u}, p]^T$, where $\mathbf{u}(\mathbf{x}, t)$ is the velocity field and $p(\mathbf{x}, t)$ is the pressure. When studying the flow dynamics in the vicinity of the laminar state, the state

variables can be decomposed as a sum of the laminar base flow $\mathbf{Q} = [U, 0, 0, P]^T$ and a perturbation $\mathbf{q}' = [u', v', w', p']$, leading to the Perturbative Navier-Stokes (PNS) equations:

$$\begin{cases} \nabla \cdot \mathbf{u}' = 0 \\ \dfrac{\partial \mathbf{u}'}{\partial t} = -(\mathbf{u}' \cdot \nabla)\mathbf{u}' - (\mathbf{u}' \cdot \nabla)\mathbf{U} - (\mathbf{U} \cdot \nabla)\mathbf{u}' - \nabla p' + \dfrac{1}{Re}\nabla^2 \mathbf{u}', \end{cases} \tag{6.1}$$

where $Re = \frac{3U_b}{2}\frac{h}{\nu}$ is the Reynolds number, defined on the basis of the bulk velocity $U_b = \int_{-1}^{1} U(y)dy$ (where $\frac{3U_b}{2}$ corresponds to the value at the centerline of the parabolic laminar flow with mean velocity U_b) , the half channel height h and the kinematic viscosity ν. Several invariant solutions of these equations, such as (relative) equilibria or periodic orbits, have been computed in the past decades (Nagata, 1990; Waleffe, 1998; Kawahara & Kida, 2001; Waleffe, 2001; Faisst & Eckhardt, 2003; Hof *et al.*, 2004; Wedin & Kerswell, 2004; Eckhardt *et al.*, 2007; Duguet *et al.*, 2008; Gibson *et al.*, 2009; Schneider *et al.*, 2010; Willis *et al.*, 2013; Deguchi *et al.*, 2013; Gibson & Brand, 2014; Zammert & Eckhardt, 2014; Park & Graham, 2015; Barnett *et al.*, 2017; Budanur *et al.*, 2017).

Conversely, when studying the dynamics of coherent structures characterising the turbulent flow, it can be appropriate to move the point of view to the vicinity of the turbulent mean flow. This is achieved by using a Reynolds decomposition approach similar to that used by Eitel-Amor *et al.* (2015) and Farano *et al.* (2017), where the flow vector is expressed as the sum of a mean flow $\overline{\mathbf{Q}} = [\overline{\mathbf{U}}, P]^T = [\overline{U}, 0, 0, \overline{P}]^T$ (where $\overline{\bullet}$ denotes long-time and space averaging along the streamwise and spanwise directions) and a fluctuation $\tilde{\mathbf{q}} = [\tilde{\mathbf{u}}, \tilde{p}]^T$, comprising the coherent and incoherent part of the perturbations of the mean flow. Time- and space- averaging along the wall-parallel directions the Navier-Stokes equations, and subtracting these averaged equations from the Navier-Stokes equations leads to the Perturbative Reynolds-Averaged Navier-Stokes (PRANS) equations, which describe in a statistical way the nonlinear evolution of fluctuations of the mean turbulent flow as:

$$\begin{cases} \nabla \cdot \tilde{\mathbf{u}} = 0 \\ \dfrac{\partial \tilde{\mathbf{u}}}{\partial t} = -(\tilde{\mathbf{u}} \cdot \nabla)\tilde{\mathbf{u}} - (\tilde{\mathbf{u}} \cdot \nabla)\overline{\mathbf{U}} - (\overline{\mathbf{U}} \cdot \nabla)\tilde{\mathbf{u}} - \tilde{\nabla} p + \dfrac{1}{Re}\nabla^2 \tilde{\mathbf{u}} + \nabla \cdot \overline{\tilde{\mathbf{u}}\tilde{\mathbf{u}}}, \end{cases} \tag{6.2}$$

where the term $\overline{\tilde{\mathbf{u}}\tilde{\mathbf{u}}}$ is the Reynolds stress tensor τ. The mean velocity profile and the Reynolds stress tensor are approximated with the analytical expression reported in section 2.1.2.

In this section, statistically invariant travelling wave solutions of the PRANS equations are sought by continuation of known invariant solutions of the PNS equations. In particular, the homotopy

procedure introduced in section 2.1.2.1 is used for continuously passing from equations (2.2) to (2.3), which have an almost identical structure, except for the steady flow used as reference and for the presence of the Reynolds stress tensor. Since these quantities depend directly on the turbulent eddy viscosity, the continuation is performed by continuously increasing this quantity from zero to its characteristic turbulent value expressed by the Cess model (Cess, 1958). Thus, statistically invariant travelling waves are obtained by continuing the ϵ parameter from travelling wave solutions of equations (2.2) using the equations 2.8. Furthermore, the continuation from the PNS to the PRANS equations is performed enforcing a constant volume flux and consequently fixing the bulk velocity $U_b = \int_{-1}^{1} U(y)dy$. Thus, while ϵ increases from 0 to 1, the friction Reynolds number grows from the laminar (Re_τ^L) towards the turbulent (Re_τ^T).

The analytical formulation presented in section 2.1.2 is validated for $Re_\tau = 180$ and $Re_\tau = 590$ comparing with the DNS (see appendix C). The results obtained are computed in this range of Reynolds numbers, for which turbulence is fully developed (not spatially patterned) and both the mean flow and the Reynolds stress are accurately described by the chosen analytical approximation.

6.2 Results

As a first attempt at validating the approach, we take as a starting point for the continuation procedure the traveling wave solution $TW2$ obtained by Gibson & Brand (2014) in a small domain at low Reynolds number. This invariant solution of the NS equations is computed at $Re = 2300$ in a domain of extension $2\pi \times 2 \times \pi$, with $32 \times 97 \times 64$ points in the streamwise (x), wall-normal (y) and spanwise (z) direction, respectively. As shown in figure 6.1 (a), the $TW2$ solution is continued with respect to the Reynolds number up to $Re = 3800$, which is sufficiently high to display featureless (not patterned) turbulence. As shown in figure 6.2 (a), the $TW2$ solution at this value of Re consists of two layers of counter-rotating vortices and slightly modulated streaks along the lower wall, and one layer of counter-rotating vortices along the upper wall (not shown). This solution is continued to the PRANS formulation by increasing the eddy viscosity as explained in section (2.1.2.1). Continuation is performed at fixed Reynolds number $Re = 3800$, enforcing a constant volume flux with bulk velocity $U_b = 0.522$. The variation of the streamwise velocity norm during this continuation procedure is shown in figure 6.1 (b). After an initial drop, the streamwise velocity norm increases with ϵ, reaching for $\epsilon = 1$ a value about 60% larger than the initial value. Moreover, when $\epsilon = 1$, the friction Reynolds

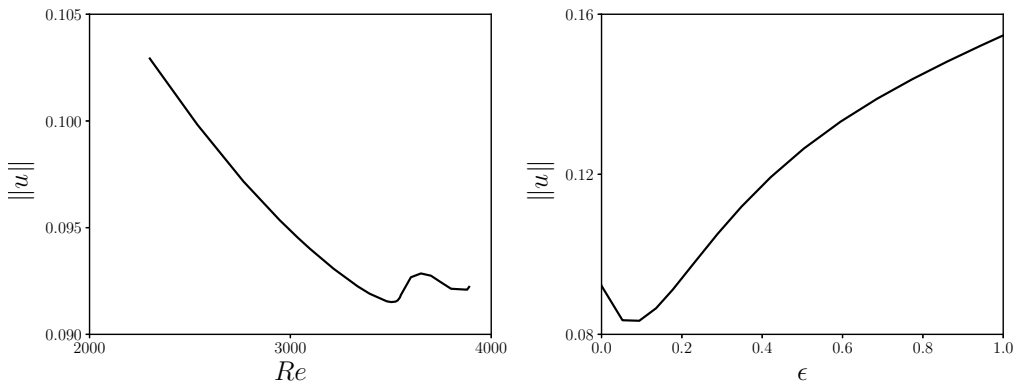

(a) (b)

Figure 6.1: Continuation diagram of the streamwise velocity norm of $TW2$ with respect to Re (left) for $\epsilon = 0$, and with respect to ϵ for $Re = 3800$ (right).

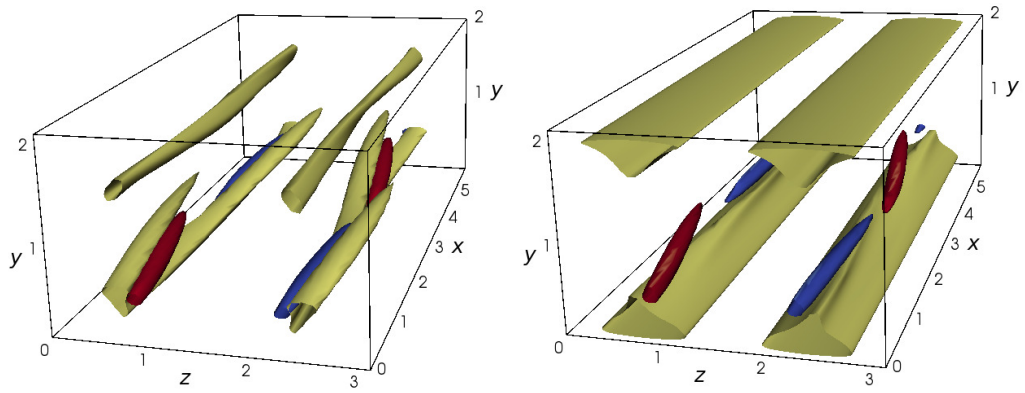

(a) $\epsilon = 0$ (b) $\epsilon = 1$

Figure 6.2: Invariant $TW2$ solution for $\epsilon = 0$ (a) and $\epsilon = 1$ (b) for $Re = 3800$: isosurfaces of negative streamwise velocity ((a) $u' = -0.11$, (b) $\tilde{u} = -0.15$, yellow) and Q-criterion ($Q = 0.1$) coloured by the streamwise vorticity (red for positive, blue for negative).

number reaches $Re_\tau = 134.521$, and the statistically invariant solution $TW2_T$, shown in figure 6.2 (b), is obtained. Notice that this friction Reynolds number is rather low for a fully developed turbulent flow, we thus expect the solution to slightly change when continued towards the PRANS framework. Comparing this statistically steady solution with the starting travelling wave, one can observe that the quasi-streamwise vortices (blue and red isosurfaces) are almost unchanged, while strong differences can be noticed on the velocity streaks, which are less fragmented, more streamwise-aligned and shifted towards the wall.

This shift of the streaks towards the wall can presumably be due to the wall-normal variation of the eddy viscosity used in the PRANS equations. As discussed in Hwang (2016), since in the near-wall

region and lower part of the logarithmic region, the eddy viscosity grows linearly with y, coherent structures are allowed to reach larger amplitudes, so they protrude towards the wall. In contrast, they weaken in the upper part of the logarithmic region and outer region, due to the large value of ν_t. Moreover, the streaks considerably increase their size in the spanwise direction, and show a peculiar triangular shape. This peculiar shape compares very well with the streaky mean flow obtained by optimally forcing a turbulent channel flow, while the vortical structures recall closely the most energetic DMD mode recovered on top of this streaky flow by de Giovanetti *et al.* (2017). The streaks reach down towards the wall, where they are almost streamwise aligned, while they present some wiggles close to the streamwise vortices. Moreover, their structures becomes almost identical on the two walls, despite the fact that in the upper wall much weaker vortices are found (not shown).

These unexpected differences with respect to the starting TW2 solution might arise from the fact

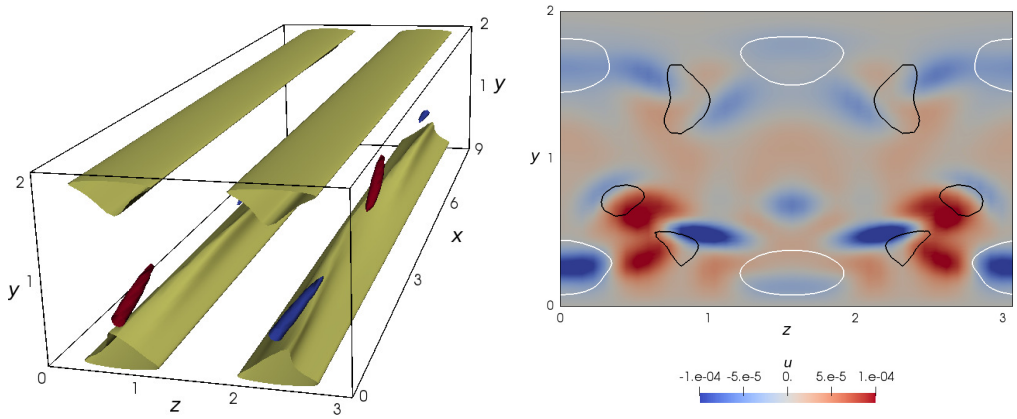

(a) $\tilde{u}$ (b) $u_{TW2_T} - u_{TW2}$

Figure 6.3: (a) Stastically steady travelling wave solution $TW2_T$, for $Re = 3800$ and $L_x = 9.544$: isosurfaces of negative streamwise velocity ($\tilde{u} = -0.15$, yellow) and Q-criterion ($Q = 0.08$) coloured by the streamwise vorticity (red for positive, blue for negative). (b) Difference of the instantaneous flow fields of $TW2$ and $TW2_T$ (shaded contours) and streamwise velocity perturbation associated to the traveling wave solution $TW2$ (black line for negative, white line for positive) for $Re = 3800$ and $L_x = 9.544$.

that, when continuing the PNS equations (2.2) towards the PRANS ones (2.3), invariant perturbations of the laminar base flow transform into statistically-coherent fluctuations of the mean flow. Thus, the observed structural change of the travelling wave solution can be simply due to the change of reference from the base to the mean flow, rather than to an intrinsic modification of the coherent motion. An answer to this important point can be found by directly comparing the instantaneous flow fields of

$TW2$ and $TW2_T$, obtained by summing up the perturbations (fluctuations) provided in the left (right) frame of figure 6.2 to the base (mean) flow, respectively. The difference between these two flow fields is found to be of $\mathcal{O}(10^{-4})$, three orders of magnitude smaller than the perturbation maximum amplitude, thus validating our procedure at such a low friction Reynolds, for which the dynamics of fluctuations of the mean flow should not strongly differ from that of perturbations of the base flow after a mere change of reference.

Once our approach has been validated, we attempt to increase the friction Reynolds number for reach values typical of fully turbulent flows. First, we tried to continue the $TW2_T$ solution further in Re, but the convergence of higher-Re solutions was very slow and time-consuming. Conjecturing that the domain might be too small for capture statistically-steady coherent structures typical of higher-Reynolds number flows, we have continued $TW2_T$ in the streamwise direction up to $L_x = 9.54$, while keeping U_{bulk} fixed. This solution, provided in figure 6.3 (a), is very similar to that previously shown, showing coherent, large-scale streaks with smaller vortices on top of them. One can again notice the strong resemblance of this solution with the main energetic structures found in a forced DNS of turbulent channel flow by de Giovanetti *et al.* (2017). However, this solution is again characterized by a rather low $Re_\tau = 134.5$, thus the difference between the relative instantaneous flow fields, shown in figure 6.3 (b), is again very small. This TW is then continued in Reynolds number up to $Re = 5945$, corresponding to $Re_\tau = 199.0$, which is only slightly higher than that characterising the $TW2_T$ solution at $Re = 3800$. Further continuation of this invariant solution of the PRANS equation with respect to Re was again very slow and time-consuming.

Motivated by these results, we have chosen a new starting point of the continuation procedure,

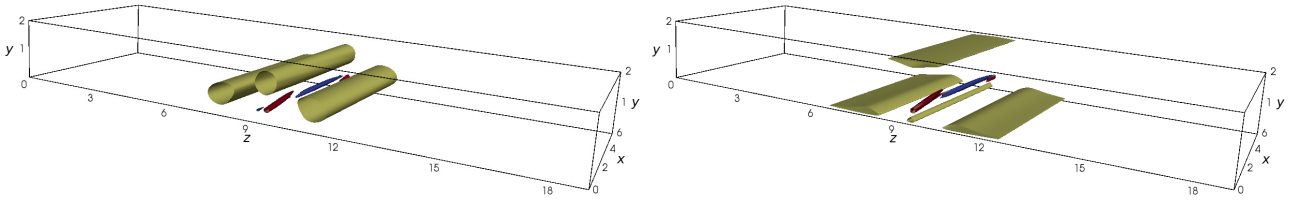

(a) $\epsilon = 0$, $Re_\tau = 99.5$ (b) $\epsilon = 1$, $Re_\tau = 210.0$

Figure 6.4: Traveling wave solution $TW2-1$ for $\epsilon = 0$ (a) and $\epsilon = 1$ (b) for $Re = 3300$ and $U_{bulk} = 1$: isosurfaces of negative streamwise velocity (yellow for (a) $u' = -0.25$, (b) $\tilde{u} = -0.46$) and Q-criterion ($Q = 0.1$) coloured by the streamwise vorticity (red for positive, blue for negative).

namely, a spanwise-localized travelling wave solution called $TW2-1$ (Gibson & Brand, 2014), whose

similarity to flow structures characterizing the near-wall cycle has been reported in the literature. This travelling wave solution, which has been obtained by continuation of $TW2$ after windowing on a larger spanwise domain (Gibson & Brand, 2014), is similar in structure to $TW2$, although though it is mostly concentrated towards one wall. We have first obtained the $TW2-1$ solution at $Re = 3300$ in the domain of size $2\pi \times 2 \times 6\pi$, with $32 \times 97 \times 324$ points in the streamwise, wall-normal and spanwise direction, respectively. The $TW2-1$ solution is continued at first with respect to the bulk velocity, up to $U_{bulk} = 1$, in order to increase its friction Reynolds number. The resulting travelling wave is shown in figure 6.4 (a) for $Re = 3300$. This spanwise-localized solution consists of slightly modulated streaks flanked by streamwise-inclined vortices, which are weaker on the upper wall, where only one streak pair is observed, and stronger on the bottom wall, where two pairs of streaks are recovered.

This $TW2-1$ solution is then continued to the PRANS equations varying the parameter ϵ from 0 to

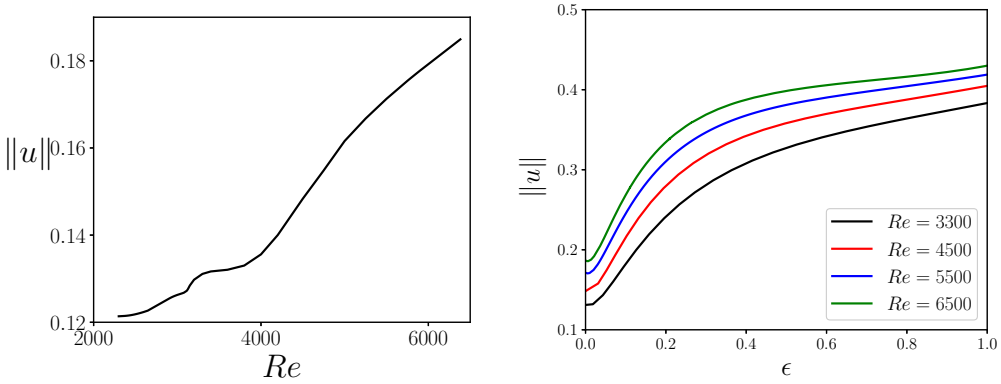

Figure 6.5: Continuation diagram for the traveling wave solution $TW2-1$ versus Re for $U_{bulk} = 1$: norm of the streamwise velocity (left) and of the wall-normal velocity (right).

1, at fixed $Re = 3300$ and $U_{bulk} = 1$. Figure 6.4 (b) provides this solution at $Re = 3300$, corresponding to $Re_\tau = 210$. The lateral streaks on the bottom wall and that on the upper wall considerably increase their size in the spanwise direction, reaching a width which appears to be close to that typical of Large Scale Motion, $\lambda_z \approx 1.5h$ (Lee *et al.*, 2014). For reach higher values of Re_τ, continuation with respect to Re of $TW2-1$ is performed, keeping U_{bulk} fixed. The variation of the norm of the streamwise velocity of $TW2-1$ during the Re-continuation is found in figure 6.5 (a), showing a continuous increase of this quantity, while the wall-normal velocity considerably decreases with Re (not shown). Several solutions at increasing values of Re have been then continued in ϵ towards the PRANS framework, as shown in figure 6.5 (b). The left column of figure 6.6 provides the $TW2-1_T$ solutions at different values

of the Reynolds number up to 6500 (corresponding to $Re_\tau = 380.03$). The whole structure of the travelling wave remains similar to that recovered at $Re = 3300$, although the streaks become stronger while the counter-rotating vortices slightly weaken. More importantly, as shown in the right column of figure 6.6, the difference between the instantaneous flow fields of the corresponding TW solutions of the PNS and PRANS equations consistently increases, now reaching the same order of magnitude of the perturbation itself. This means that the structural modifications of $TW2-1_T$ with respect to $TW2-1$ at high Re_τ do not depend only on the change of reference from the laminar base flow to the mean turbulent flow, but on an intrinsic difference in the coherent disturbances dynamics. The right column of figure 6.6 shows a cross-section of the low- and high-speed streaks of TW2-1 (black and white curves) at different Reynolds numbers, together with the difference between the instantaneous flow fields of $TW2-1$ and $TW2-1_T$ at the same values of Re (shaded contours). One can notice that the largest modifications are observed on the lateral low-speed streaks, which increase their spanwise size and move towards the wall, and on the high-speed ones at the wall, which appear to change their spanwise size too (not shown). However, while the streamwise velocity is modified in a large part of the domain, the counter-rotating vortices change exclusively in a very narrow zone between the low- and high-speed streaks. The result of these modifications is a consistent increase of the spanwise size of most of the streaks, which reach a length comparable to the channel half-height, typical of Large Scale Motion (del Alamo & Jiménez, 2003; Hwang, 2015; Lee *et al.*, 2014). A smaller-size streak is observed as well, with spanwise size $\mathcal{O}(100)$ (in inner units), close to that typical of wall streaks. However, this smaller-scale coherent structure does not appear directly linked to the wall cycle, since, as shown in figure 6.7 (a), its streamwise-averaged velocity profile extracted at $z = 9$ and scaled with respect to the inner units, appears not to be independent of Re_τ, as one would expect for wall-cycle related structures. In particular, its peak scales approximately with $Re_\tau^{1/2}$, as one would expect for large-scale structures (Hwang, 2016). It is worth noticing that the same scaling with respect to Re_τ characterises the lateral large-scale streaks, whose inner-scaled velocity profiles are shown in figure 6.8(a). However, comparing figures 6.7 (b) and 6.8 (b), one can also notice that, while the lateral streaks present a robust outer scaling, confirming their large-scale nature, for the small-scale central streak the velocity profiles at different Re_τ do not collapse at large values of y. Thus, the small-scale central streak cannot be related directly with the wall cycle, but neither can the large-scale structures, probably being linked to the secondary motion induced by the vortical structures placed at the center

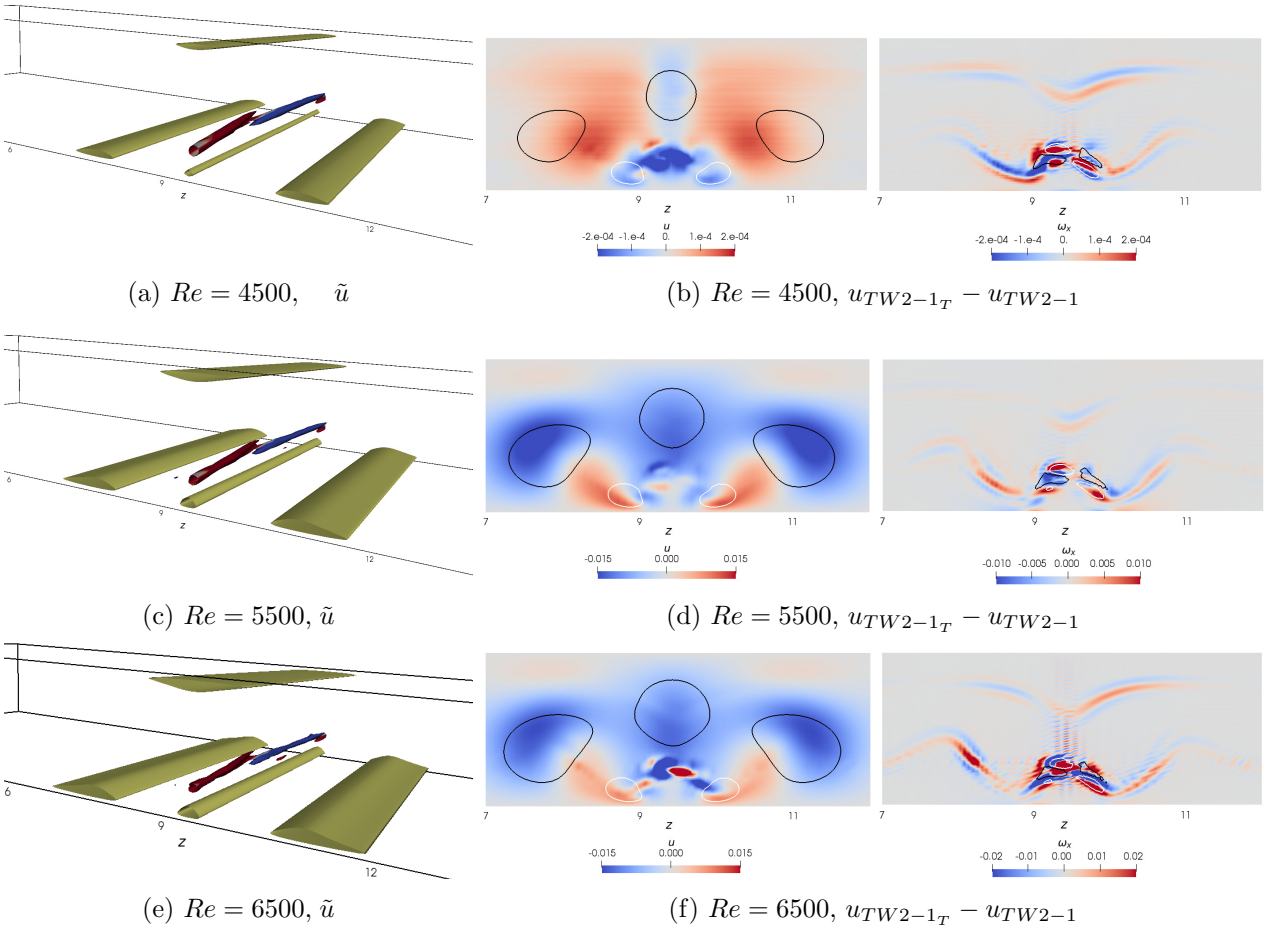

(a) $Re = 4500, \quad \tilde{u}$

(b) $Re = 4500$, $u_{TW2-1_T} - u_{TW2-1}$

(c) $Re = 5500$, $\tilde{u}$

(d) $Re = 5500$, $u_{TW2-1_T} - u_{TW2-1}$

(e) $Re = 6500$, $\tilde{u}$

(f) $Re = 6500$, $u_{TW2-1_T} - u_{TW2-1}$

Figure 6.6: (Left) Traveling wave solution $TW2 - 1_T$ at different Reynolds numbers: isosurfaces of negative streamwise velocity ($\tilde{u} = -0.55$, yellow) and Q-criterion ($Q = 0.1$) coloured by the streamwise vorticity (positive red, negative blue). (Right) Solid velocity and vorticity contours associated to the traveling wave solution $TW2 - 1$ obtained with $\epsilon = 0$ (black line for negative, white line for positive), and difference between the two instantaneous solutions $u_{TW2-1_T} - u_{TW2-1}$ (shaded contours for the streamwise velocity and vorticity, see legend).

of the domain.

These counter rotating vortices located in the region between the large-scale streaks, reaching much

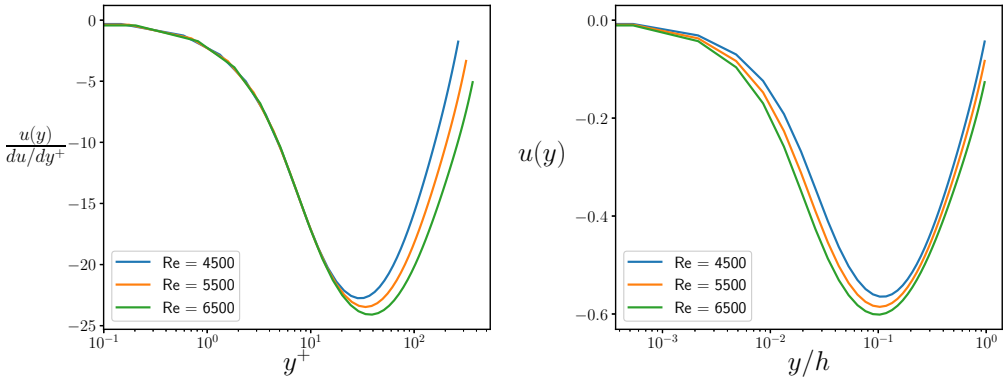

(a) (b)

Figure 6.7: Streamwise-averaged velocity profile of the $TW2-1_T$ extracted at the z location where the central small-scale streak present their maximum value, scaled in inner (left) and outer (right) units.

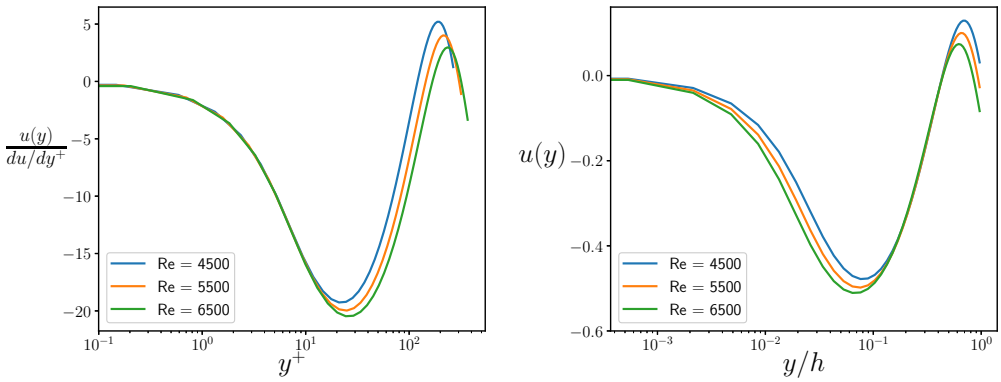

(a) (b)

Figure 6.8: Streamwise-averaged velocity profile of the $TW2-1_T$ extracted at the z location where the lateral large-scale streaks present their maximum value, scaled in inner and outer units.

higher distances from the wall, similar to the typical vortical structures recovered in large-scale motion (also called bulges).

A quantitative analysis of the main spanwise wavelengths of $TW2-1_T$ has been carried out by computing the premultiplied energy spectra of the streamwise, wall-normal and spanwise velocities of this solution at $Re = 4500$ (corresponding to $Re_\tau = 275.47$), which are shown in figure 6.9 (a), (b), (c), respectively. Concerning the streamwise velocity, the lowest-wavenumber peak ($k_z^+ = 0.00127$, or

$k_z = 0.35$ in outer units) corresponds to the size of the TW envelope, since it is close to the spanwise domain size. Two other peaks are recovered for $k_z^+ = 0.0065$ and $k_z^+ = 0.0155$, corresponding to wavelengths $\lambda_z = 3.5$ and $\lambda_z = 1.47$ in outer units, respectively, which lie in the range of the typical spanwise size of Large-Scale Motion (reported to be $\lambda_z = 1 - 3$ in outer units). A higher-frequency, weaker peak is found for $k_z^+ = 0.047$, corresponding to $\lambda_z^+ = 135$, which is rather close to the typical spanwise size of wall-streaks. In contrast, the wall-normal and spanwise spectra are both characterized by one peak only, at $k_z^+ = 0.048$ (corresponding to $\lambda_z^+ = 130.08$) and $k_z^+ = 0.026$ ($\lambda_z^+ = 235.32$), respectively. Notice that these wavelengths are much lower than the dominant ones of the streamwise velocity spectra, being closer to those typical of the wall cycle. Very similar spectra are recovered at $Re = 5500$ and $Re = 6500$ (corresponding to $Re_\tau = 328.35$ and $Re_\tau = 380.03$, respectively), indicating that the structure of $TW2 - 1_T$ remains robust when the Reynolds number increases. Moreover, it is interesting to evaluate the scaling of the relevant structures of these solutions with respect to those of the single self-sustaining attached eddy (Hwang, 2015), which is composed of a long streaky motion reaching the near-wall region, self-similar along $y = 0.1\lambda_z$ and a shorter vortical structure carrying all the velocity components, self-similar along $y = 0.5 - 0.7\lambda_z$. A very similar scaling is found in the $TW2 - 1_T$ solution, with the two dominant peaks in the streamwise velocity spectrum having $y \approx 0.1 - 0.15\lambda_z$ while a scaling of $y \approx 0.58\lambda_z$, $y \approx \lambda_z$ is found in the spanwise and wall-normal spectra, respectively. The statistically steady solution presented here, composed of large streaky structures and short vortical ones carrying all velocity components, is thus similar in shape and wavelengths to the self-sustaining structures of the attached eddy theory (Hwang, 2015). However, in this solution, large- and small-scale structures are not torn apart, but tied together in a non trivial way, representing one potential first brick for the development of a low-order model of turbulence dynamics.

6.3 Conclusion

A new mathematical framework for characterising the coherent motion of turbulent fluctuations around the mean flow in a turbulent channel was proposed, using a statistical point of view. In particular, we search for statistically invariant coherent solutions of the unsteady Reynolds-averaged Navier-Stokes equations written in a perturbative form with respect to the turbulent mean flow, using a suitable approximation of the Reynolds stress tensor. To do so, we set up a continuation procedure

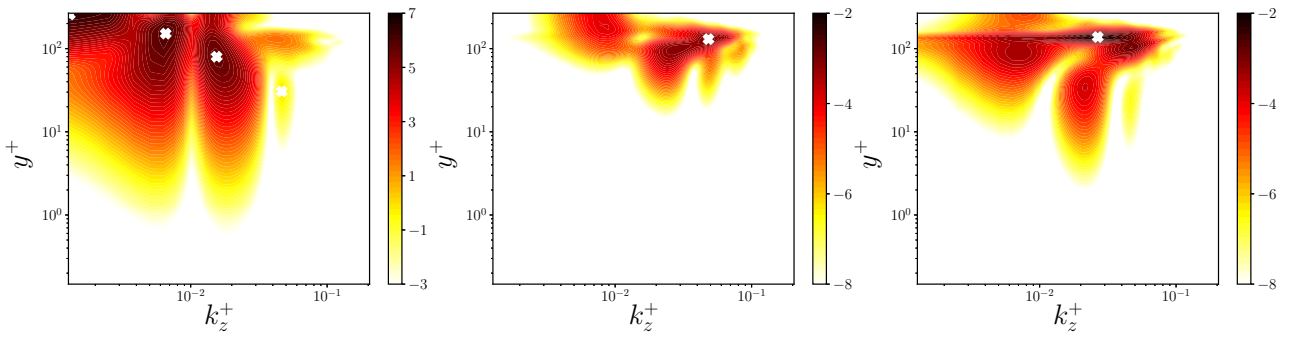

(a) $k_z E_{uu}(k_z)$ (b) $k_z E_{vv}(k_z)$ (c) $k_z E_{ww}(k_z)$

Figure 6.9: Premultiplied one-dimensional spanwise spectra of the streamwise (left), wall-normal (middle) and spanwise velocity (right) of $TW2-1_T$ at $Re=4500$.

of known invariant solutions of the perturbative Navier-Stokes equations, based on the continuous increase of the eddy viscosity towards its turbulent value. The recovered solutions are sustained only in the presence of the Reynolds stress, thus being representative of the coherent motion of turbulent flows.

The travelling wave $TW2$ has been first used as a starting point of the continuation procedure and continued to the turbulent framework up to friction Reynolds number $Re_\tau \approx 134.52$. Although structural changes are found in the solution when regards to instantaneous quantities the statistically invariant motion turns out to be only marginally different from the corresponding invariant solution of the Navier-Stokes equations. This was expected since turbulence is not fully sustained at such low values of the friction Reynolds number so that the dynamics of statistically coherent motion of fully turbulent flows remains close to that of transient turbulence and transition. However, by taking the spanwise-localized solution $TW2-1$ as a new starting point, and continuing it to the statistically turbulent framework at sufficiently large friction Reynolds number ($Re_\tau \approx 380.03$), the statistically invariant motion considerably departs from the starting solution. This solution is characterized by large-scale and small-scale streaks reaching the wall, accompanied by rather small vortical structures further from the wall. These structures, as well as the main wavelengths and scaling of this statistically invariant solution, are very close to those typical of the coherent motion in turbulent channel flows. In particular, the dominant wavelengths of the streamwise velocity premultiplied energy spectrum correspond to the typical spanwise size of large-scale structures ($1.5-3.5$ times the half channel height) and are characterized by a scaling $y \approx 0.1-0.15\lambda_z$, consistent with the attached eddy hypothesis. In contrast, spanwise lengths typical of the wall cycle and a scaling of $y \approx 0.58\lambda_z$, $y \approx \lambda_z$ are found in the

spanwise and wall-normal spectra, respectively. Thus, the statistically steady solution presented here, constituted by large streaky structures and short vortical ones carrying all velocity components, is similar in shape and wavelengths to the self-sustaining structures of the attached eddy theory Hwang (2015), although composed of large- and small-scale structures tied together in a non trivial way. This statistically-invariant solution may potentially represent one brick for the development of a low-order model of turbulence dynamics.

It should be remarked that the comparison of the main wavelengths and scaling of this statistically

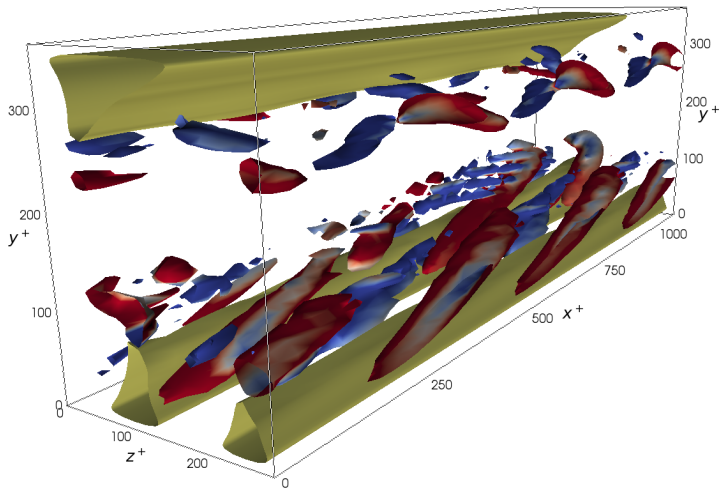

Figure 6.10: Traveling wave solution obtained starting from the optimal solution obtained ad $Re_\tau = 180$ with the initial energy $E_0 = 10^{-2}$ at the target time $T = 10$. Isosurfaces of negative streamwise velocity (yellow) an Q-criterion coloured by the streamwise vorticity.

invariant solution with those of the attached eddy has been limited to the spanwise direction since the present solution has been obtained in a rather small streamwise domain. Future work will aim at continuing this or other solutions towards larger streamwise domains, as well as towards much higher friction Reynolds numbers. Moreover, new statistically invariant solutions might be obtained using as a starting point filtered snapshots of the turbulent flows, instead of continuing known invariant solutions of the Navier-Stokes equations. In particular, the turbulent nonlinear optimal perturbations computed in Chapter 5, might be used as a starting point for this search, since they are solutions of the same set of equations, and characterising energetic coherent structures within the turbulent flow. In the context of the NS equations, Olvera & Kerswell (2017) have demonstrated that nonlinear optimal perturbations might be a good starting point for the search of invariant solutions, and this

might be true also for the PRANS equations. Thus, we have attempted this search using the optimal perturbation computed for $Re_\tau = 180$ at the target time $T = 10$ and with an initial energy $E_0 = 10^{-2}$. As one can see in figure 6.10, the flow exhibits a shape similar to the statistically-invariant solutions previously shown. In particular, low velocity streaks are localised near the wall, while vortical structures migrate toward the center of the channel. This indicates a possible strategy for computing invariant solutions at high friction Reynolds number, while avoiding the computationally expensive continuation of known solutions of the NS equations.

Finally, statistically-periodic solutions can be recovered as well, providing relevant information about the temporal dynamics of the coherent part of the fluctuations in the considered statistical framework. This might be a considerable step forward towards the development of reduced-order models of turbulent flows.

Chapter 7

Conclusion and perspectives

Contents

7.1 Conclusion

In this thesis, we have studied the dynamics of a plane channel flow; in particular, the first part of this work was devoted to the subcritical transition; whereas, in the second part, the coherent structures characterising the fully-developed turbulence are investigated.

In the first part, an analysis of turbulent bands located in the laminar channel flow is carried out, searching for the main mechanisms involved in the origin and growth of these turbulent bands. In chapter 3, the analysis is performed in a large domain, while in chapter 4 the complexity of the problem is reduced by using a much smaller tilted domain.

In chapter 3, for the first time, the minimal seed able to trigger turbulence in the form of a laminar-turbulent pattern in a large-sized channel flow, has been investigated. This structure has a spot-like shape with a quadrupolar large-scale flow surrounding it. The relation between the minimal input energy able to trigger turbulence and the Reynolds number was investigated and a scaling law of the type $Re^{-\gamma}$, with $\gamma \approx 8.5$ (fourth times that found in the literature) was found. Looking at the minimal perturbation evolution in time, two different minimal-energy paths for the generation of turbulent bands have been observed, depending on the Reynolds number: for $Re > 1200$ the spot evolves symmetrically in two bands, whereas, for $Re < 1200$ only one band is created. An analysis of

the production and dissipation of kinetic energy shows that in both cases, two proto-bands are initially created at the edges of the large-scale flow surrounding the minimal seeds. Since the probability of decay of the bands increases in time and is higher for low Reynolds number, when Re is sufficiently low one of these bands rapidly dies out, leading to the development of one isolated band. In contrast, for larger values of Re, both oblique bands originated at the sides of the minimal seed survive for a longer time, until they split and interact, rapidly leading to the establishment of a spatio-temporally complex final state.

The early mechanisms of formation of these proto-bands are further investigated by restraining the investigation to a much smaller, tilted domain. Performing linear optimization in such a small tilted domain at $Re = 1000$, in which only one turbulent band is observed, a three-dimensional optimal structure characterised by streaks aligned with the tilted baseflow was found. In particular, these streaks are similar to those observed at the head of turbulent bands and present streamwise and spanwise wavenumbers very close to those found in the energy spectra of a DNS performed in the same domain. However, we have found that transition to a turbulent band arises due to this optimal lift-up mechanism only when coupled with a large-scale vortical flow linked to the spatial localisation of the disturbance. Thus, a nonlinear mechanism is necessary to generate a large-scale flow that provides the preferential spreading direction of the streaks generated by the lift-up mechanism.

In order to investigate the coherent structures usually observed in turbulent flows and characterise the turbulent motion, in chapter 5, we have extended the nonlinear optimisation to turbulent channel flow. However, due to the nonconvex form of the nonlinear Navier-Stokes equations multiple solutions are found for a given set of initial conditions and target times. Thus, we have chosen to follow a different approach, and try to characterise the turbulence coherent motion searching for statistically-steady coherent solutions. For this reason, in chapter 6, we have proposed a 'new' mathematical framework for seeking travelling-wave solutions characterising the motion of turbulent fluctuations around the mean flow. This was achieved by searching for statistically-invariant coherent solutions of the unsteady perturbative Reynolds-averaged Navier-Stokes (PRANS) equations written in a perturbative form with respect to a suitable analytical approximation of the turbulent mean flow and the Reynolds stress tensor. Moreover, in chapter 6, a homotopy method has been proposed to continue invariant solutions of the perturbative Navier-Stokes (PNS) equations to the PRANS equation via the continuous increase of the turbulent eddy viscosity towards its turbulent value. At small friction Reynolds numbers,

slight differences have been found between the invariant solutions found using the PNS equations and the statistically invariant solutions. Whereas, for larger friction Reynolds numbers and domain size, major differences have been identified. Furthermore, the statistically-invariant solutions of the PRANS equations are characterized by streaks and streamwise vortices with wavelengths and scaling close to those found for small- and large-scale structures in turbulent channel flow.

7.2 Perspectives

The results produced in this work of thesis are not entirely conclusive. They nonetheless provide several insights and raise numerous questions that need an answer about transitional flows and fully turbulent flows, such as:

1. The minimal input energy able to trigger turbulence in large channel flow scales with the Reynolds number with a power-law, but as already highlighted in chapter 3 the power-law exponent is four times larger than the value reported in the literature; we have suggested that this discrepancy can be linked to the much larger domain size considered. To clarify this point, it is necessary to investigate the scaling of the minimal input energy with the Reynolds number searching for the *minimal seed* in plane channel flow with a small domain size comparable to those used in the literature for other flows.

2. In this work, the seed for the turbulent bands is found via nonlinear optimization; thus, this method can be extended to other flows in the range of Reynolds numbers in which the localised turbulence is observed, as for turbulent bands in plane Couette flow or turbulent puffs in pipe flow. Furthermore, in the chapter 4, we have investigated the main mechanism involved in the origin and evolution of turbulent bands, however many questions remain unanswered, for instance the reason why the turbulent bands evolve with a particular angle that changes with the Reynolds number.

3. Since the laminar-turbulent pattern is also observed in channel flow with a thermal stratification or with a magnetic field, the analysis performed in the chapter 3 and 4 may be extended to identify the influence of the temperature or the magnetic field on the optimal perturbation and the main mechanisms involved in the origin of turbulent bands.

4. In chapter 5, starting from the works of Farano *et al.* (2017, 2018), we have searched for nonlinear optimal fluctuations around the mean flow at different target times and, we have observed that increasing the target time more and more large-scale structures appear. Moreover, the nonlinear optimization can be extended to high friction Reynolds number to investigate for very large-scale motions, which appear when there is enough spatial separation between the inner and the outer regions.

5. In chapter 5, at $Re_\tau = 180$ two main nonlinear optimal perturbations are found, one with structures close to the wall and the second with structures that move to the center of the channel. The former is found mostly for very low target time, whereas the latter for higher ones. Moreover, there is an intermediate range of target times in which both optimal solutions can be found, according to the initial condition. Then, a further analysis at different friction Reynolds numbers needs to be carried out to confirm this behaviour. Moreover, the characteristics and the role in the dynamics of these nonlinear optimal perturbation worth to be investigated.

6. The solutions reported in chapter 6 are found from invariant solutions known in the literature, which are solutions of the NS equations, thus require a lengthy continuation towards the PRANS framework. On the other hand, coherent structures that are solutions of the PRANS equations, might be used for initialising the search for statistically invariant solutions. In particular, the nonlinear optimal perturbations shown in chapter 5 may be used as a starting point to collect other statistically invariant solutions directly in the PRANS equation. This has been attempted with success at $Re_\tau = 180$, and current works are attempting at computing nonlinear optimal perturbations at higher values of Re_τ, which can be used as starting point for the search of statistically-invariant solutions.

7. In this thesis, we have searched only for travelling-wave solutions of the PRANS equations. Statistically-periodic solutions of this set of equations may provide relevant information about the temporal dynamics of the coherent part of the fluctuations in the considered statistical framework. This might be a considerable step forward towards the development of reduced-order models of turbulent flows. However, the extension to the periodic orbit implies some considerations on the chosen mean flow averaged in time, thus more theoretical work must be done before trying to compute them.

Appendix A

Optimization problem validation

A.1 Test cases

In this section, the validation of the direct-adjoint algorithm is presented via some results for nonlinear optimal perturbations in plane Poiseuille flow.

A.1.1 Nonlinear optimal perturbations in Poiseuille flow

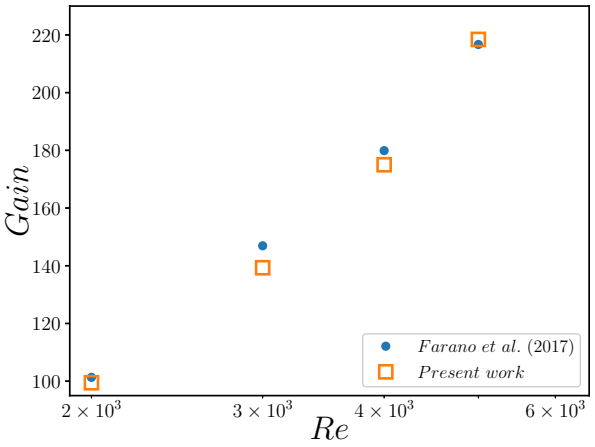

Figure A.1: Energy gain comparison with the reference work (Farano *et al.*, 2015).

The nonlinear optimal perturbation is computed for plane Poiseuille flow, comparing the results to those obtained by Farano *et al.* (2015). The optimizations are performed for four subcritical Reynolds numbers ($Re = 2000, 3000, 4000, 5000$) for the target time $T = 10$, the characteristic time of the Orr mechanism (Orr, 1907). The simulations are performed in a domain with dimensions 2π, 2 and π in the streamwise, wall-normal and spanwise directions, respectively.

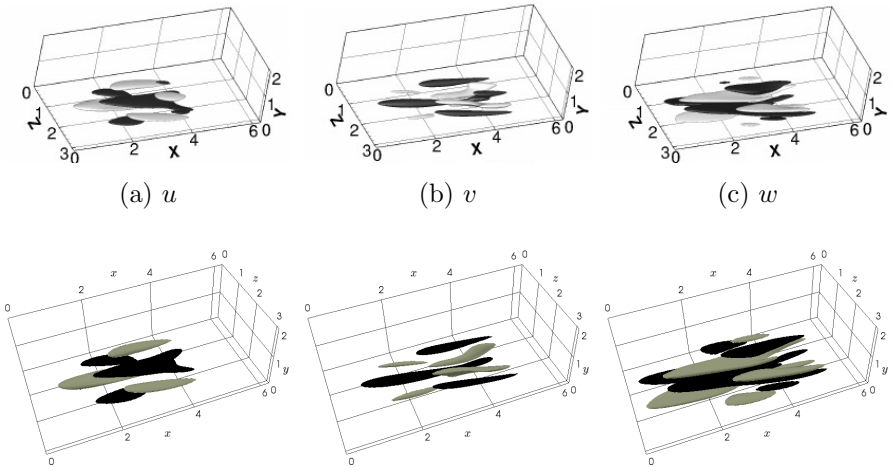

(a) u (b) v (c) w

(d) u (e) v (f) w

Figure A.2: Isosurfaces of the three velocity components (light grey for positive and black for negative values, $u, v, w = \pm 0.01$) of the nonlinear optimal perturbation for $T_{opt} = 10$, $E_0 = 1 \times 10^{-5}$ and $Re = 2000$. (Top) Farano *et al.* (2015) results. (Bottom) Present work results.

The chosen objective function is the kinetic energy:

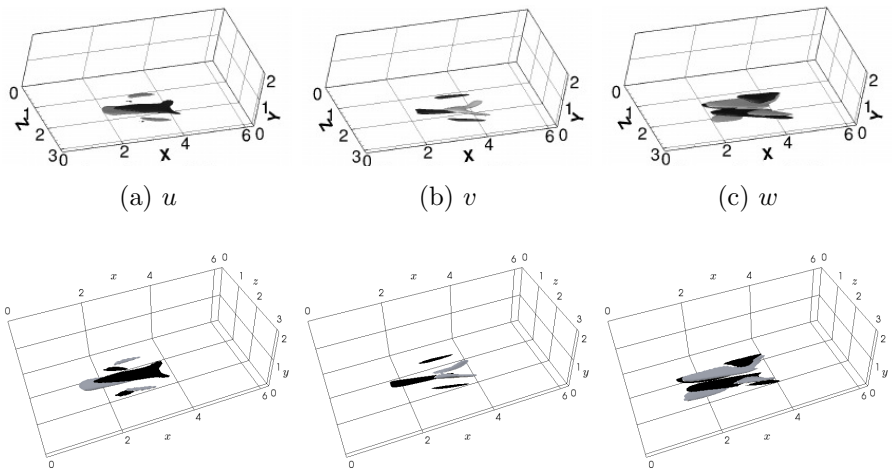

(a) u (b) v (c) w

(d) u (e) v (f) w

Figure A.3: Isosurfaces of the three velocity components (light grey for positive and black for negative values, $u, v, w = \pm 0.01$) of the nonlinear optimal perturbation for $T_{opt} = 10$, $E_0 = 2 \times 10^{-6}$ and $Re = 4000$. (Top) Farano *et al.* (2015) results. (Bottom) Present work results.

$$E(t) = \frac{1}{2V} \int_V (u^2 + v^2 + w^2) dV.$$

The values of the input energy E_0 are those reported by Farano *et al.* (2015) in figure 1(a).

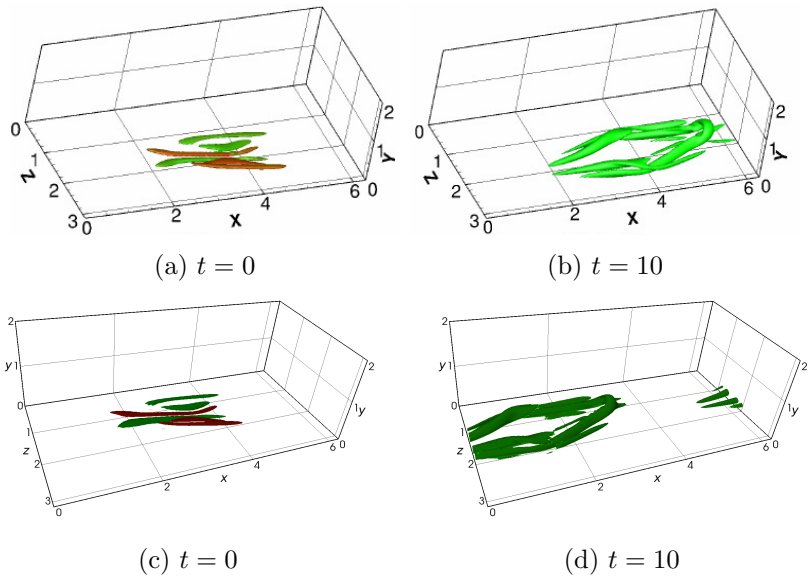

(a) $t = 0$ (b) $t = 10$

(c) $t = 0$ (d) $t = 10$

Figure A.4: Isosurfaces of the Q-criterion coloured with the streamwise vorticity of the nonlinear optimal perturbation for $T_{opt} = 10$, $E_0 = 2 \times 10^{-6}$ and $Re = 4000$. (Top) Farano *et al.* (2015) results. (Bottom) Present work results.

The energy gain at the target time for all the considered Reynolds is reported in figure A.1. Notably, it is found a good agreement with the reference results.

In figures A.2 and A.3 are shown the optimal perturbations found for $Re = 2000$ with $E_0 = 1 \times 10^{-5}$ and for $Re = 4000$ with $E_0 = 2 \times 10^{-6}$, respectively; these solutions present a similarly shape with different amplitude, higher for the case at $Re = 2000$. A good agreement with the results reported in literature is shown.

It is worth noticing that compared to linear optimal perturbations many differences are found: in particular, these solutions are strongly localised in the domain and are characterised by a smaller wavelength in the spanwise direction. Furthermore, at small target time, symmetry in the spanwise direction is observed, unlike other flows as plane Couette flow. Notably, in figure A.2 and A.3 the symmetry of the streamwise and wall-normal velocity components is observable, whereas the spanwise velocity component is antisymmetric.

The nonlinear optimal perturbation for $Re = 4000$ and $E_0 = 2 \times 10^{-6}$ is shown in figure A.4 at $t = 0$ and at the target time, represented with the Q-criterion coloured with the streamwise vorticity. The optimal perturbation presents a localised shape in the form of three thin tubes of counter-rotating vorticity alternated in the spanwise direction. When these structures evolve in time, an interaction of

the inner vortices coupled with tilting in the streamwise direction leads to the formation of a hairpin vortex at target time $t = 10$.

Appendix B

Derivation of the mean turbulent velocity equation

In this appendix, the derivation of the mean turbulent velocity analytical expression (2.4) proposed by Reynolds & Tiederman (1967) are reported.

Being the channel turbulent flow statistically stationary and homogeneous along the streamwise x and spanwise z directions, the momentum equations from the perturbative Navier-Stokes equations of the mean turbulent flow (2.2) along x-axis and y-axis are reduced to:

$$\frac{d\overline{u'v'}}{dy} = -\frac{\partial P}{\partial x} + \frac{1}{Re}\frac{d^2\overline{U}}{dy^2} \tag{B.1}$$

$$\frac{d\overline{v'^2}}{dy} = -\frac{dP}{dy}. \tag{B.2}$$

Integrating the equation (B.2) along the y-axis, it is found that the streamwise pressure gradient is independent from the normal direction y, i.e. it is constant across the flow. Then, the equation (B.1) becomes:

$$\frac{dP}{dx} = \frac{1}{Re}\frac{d}{dy}\left[\frac{d\overline{U}}{dy}\left(-\frac{dy}{d\overline{U}}Re\overline{u'v'} + 1\right)\right]. \tag{B.3}$$

Then, from the Prandtl's mixing length model:

$$\overline{u'v'} = -\nu_t\frac{d\overline{U}}{dy},$$

and considering that the normalised total eddy viscosity can be expressed with $\nu_T^+ = \nu_T/nu = (\nu + \nu_t)/\nu$:

$$\frac{dy}{d\overline{U}}Re\overline{u'v'} = \nu_T^+ - 1.$$

In this way, the equation (B.2) reads:

$$\frac{dP}{dx} = \frac{1}{Re}\frac{d}{dy}\left(\frac{d\overline{U}}{dy}\nu_T^+\right),$$

and integrating along y-axis:

$$\frac{dP}{dx}y = \frac{\nu_T^+}{Re}\frac{d\overline{U}}{dy}.$$

And finally, considering that $\overline{U} = \overline{U}^+ Re_\tau/Re$ and the pressure gradient $dP/dx = (Re_\tau/Re)^2$, the mean turbulent velocity profile equation is obtained:

$$\frac{d\overline{U}^+}{dy} = \frac{Re_\tau y}{\nu_T^+}. \tag{B.4}$$

Appendix C

Validation of the mean turbulent flow formulation

In this appendix, the validation of the analytical formulation introduced in the section 6.1 for the mean turbulent flow and the Reynolds stress tensor, is presented.
The validation is performed for two friction Reynolds number, such as $Re_\tau = (180, 590)$. The results obtained for $Re_\tau = 180$ are compared with those obtained by Kim *et al.* (1987) and for $Re_\tau = 590$ are compared with the results obtained by Moser *et al.* (1999).
The results of the direct numerical simulation performed in *Channelflow* and the analytical profiles are obtained at fixed Reynolds number $Re = 3300$ and enforcing the constant volume flux with the bulk velocity $U_b = 0.8485$ for $Re_\tau = 180$ and at fixed $Re = 12450$ and $U_b = 0.8632$ for $Re_\tau = 590$.
In figure C.1 and in figure C.2, the mean turbulent flow and the Reynolds stress validation are reported for $Re_\tau = 180$ (top frames) and for $Re_\tau = 590$ (bottom frames), respectively. In these figures, we show the mean turbulent flow and the Reynolds stress obtained with the DNS carried out in *Channelflow*, the analytical solutions obtained from the equations presented in the section 6.1.
Furthermore, the mean velocity and the Reynolds stress profiles obtained with the perturbative RANS equations forced with the analytical statistics (left frames) and with the statistics obtained with the direct numerical simulation (right frames), are shown.

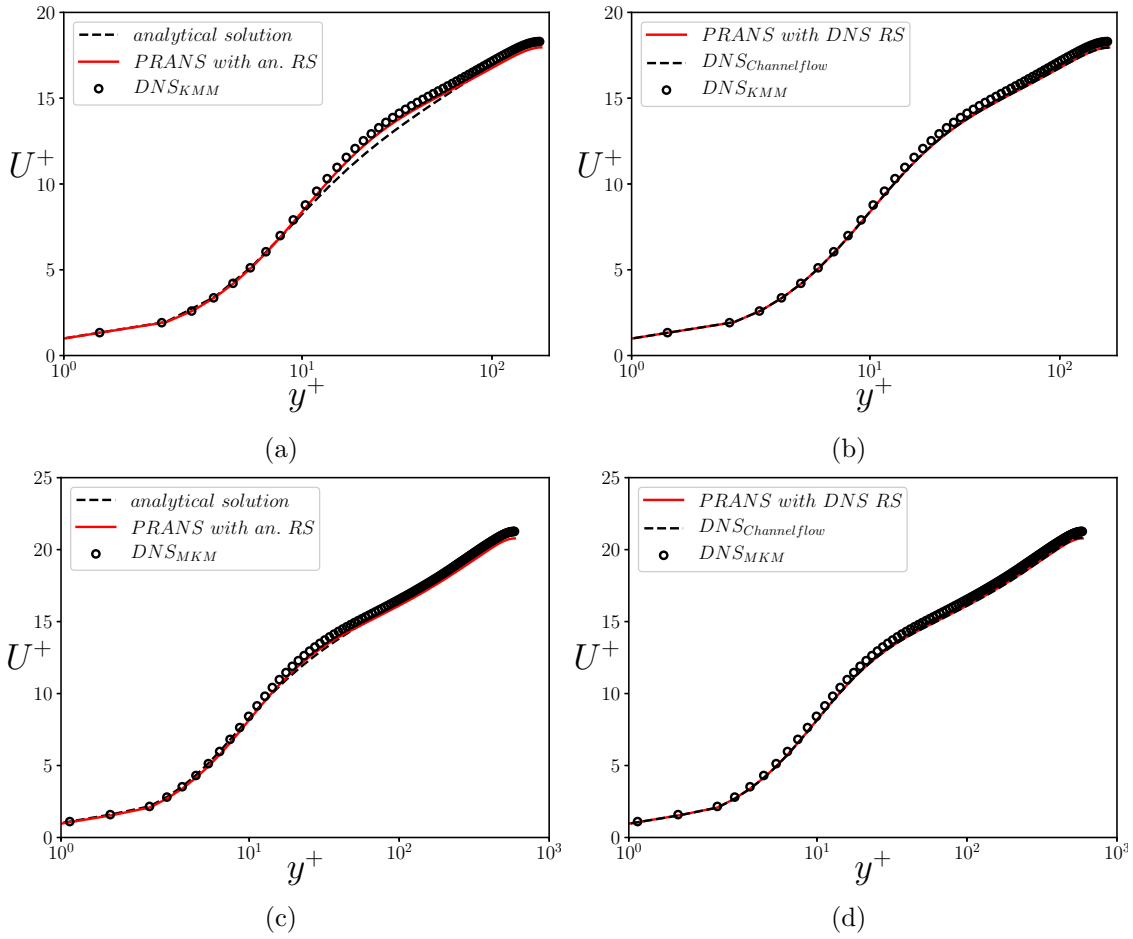

Figure C.1: (a-c) Mean velocity profile obtained with the PRANS equations (red solid line) with the analytical mean velocity profile (black dashed line) compared with literature results (black dots). (b-d) Mean velocity profile obtained with the PRANS equations (red solid line) with the mean velocity profile obtained by DNS (black dashed line) compared with literature results (black dots). Top and bottom frames correspond to $Re_\tau = 180$ (reference case Kim *et al.* (1987)) and $Re_\tau = 590$ (reference case Moser *et al.* (1999)), respectively.

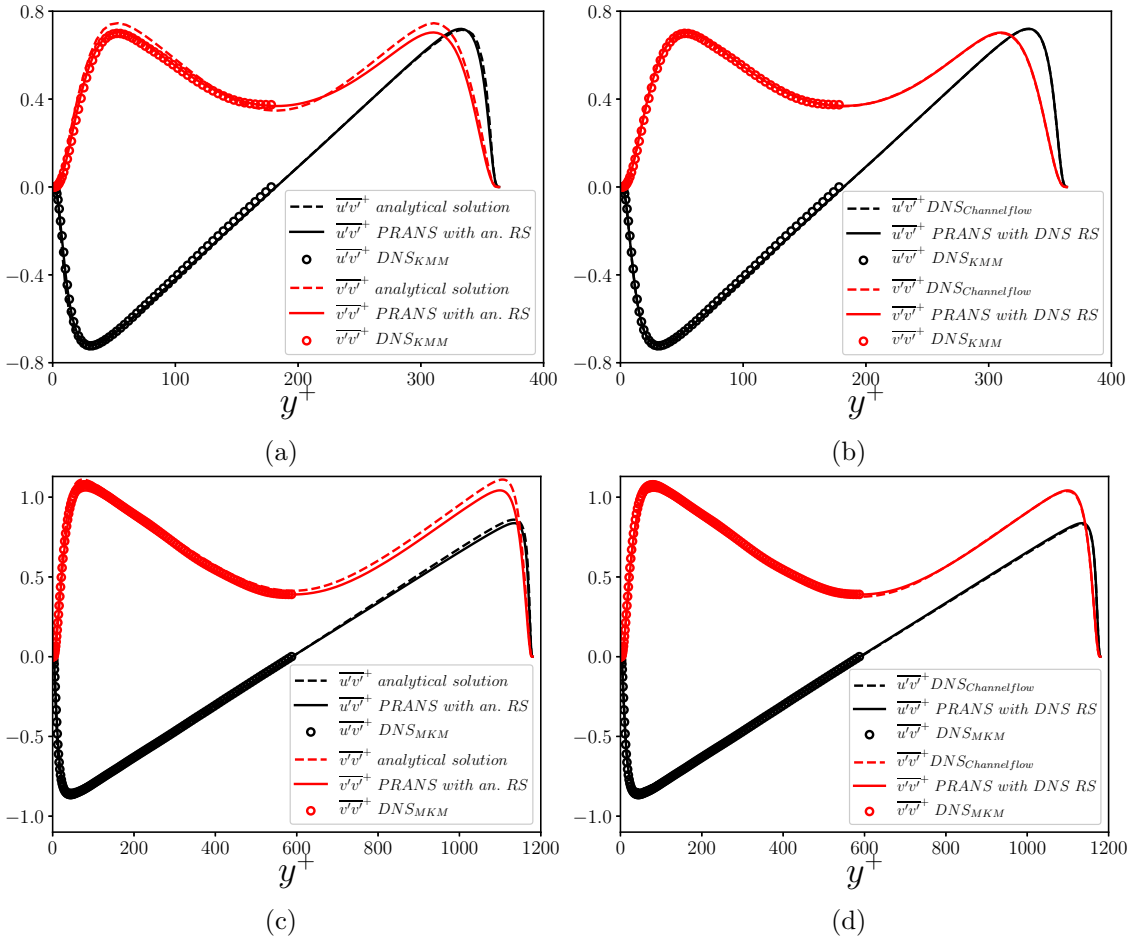

Figure C.2: (a-c) Reynolds stress profile obtained with the PRANS equations (red solid line) with the analytical Reynolds stress profile (black dashed line) compared with literature results (black dots). (b-d) Reynolds stress profile obtained with the PRANS equations (red solid line) with the Reynolds stress profile obtained by DNS (black dashed line) compared with literature results (black dots). Top and bottom frames correspond to $Re_\tau = 180$ (reference case Kim *et al.* (1987)) and $Re_\tau = 590$ (reference case Moser *et al.* (1999)), respectively.

Appendix D

Test cases for the continuation method

D.1 Test cases

As a first step, to understand how the edge-tracking technique and the continuation method work, the periodic orbit and the travelling waves found in the channel flow by Rawat *et al.* (2014, 2016) are searched.

D.1.1 Relative periodic orbit solution

In the previous edge-tracking section 2.3.1 it is reported that to find an edge state a suitable initial guess sufficiently close to the edge is necessary. As introduced by Waleffe (2003) the flow can be artificially forced by streamwise vortices which induce unstable streamwise streaks at a critical forcing amplitude. This is an opportune perturbation when looking for an edge state since it is a lower-branch solution, often characterized by streaky structures.
Following the procedure adopted by Rawat *et al.* (2014), the edge-tracking is performed perturbing the laminar Poiseuille flow with a pair of streamwise uniform counter-rotating vortices of amplitude A_1 and a sinuous perturbation of the spanwise velocity with amplitude A_2:

$$\mathbf{u}_0 = A_1 \left\{ 0, \frac{\partial \psi_0}{\partial z}, -\frac{\partial \psi_0}{\partial y} \right\} + A_2 \left\{ 0, 0, \omega_{sin} \right\}, \tag{D.1}$$

where $\psi_0(y,z) = (1-y^2)sin(\pi y)sin\left(2\pi z/L_z\right)$ is the stream-function associated to streamwise uniform vortices, and $\omega_{sin}(x,y) = (1-y^2)sin\left(2\pi z/L_z\right)$ represents the sinuous perturbation.
In addition, the bisection is performed enforcing the mid-plane reflection symmetry $(u, v, w(x, y, z) = u, -v, w(x, -y, z))$ and the amplitude of the counter rotating vortices A_1 is chosen as the bifurcation

parameter, with $A_2/A_1 = 1/10$ fixed.

The Reynolds number is fixed at 3000, imposing a constant volume flux during the simulations. The results are obtained with $32 \times 65 \times 32$ points in the streamwise, wall-normal, and spanwise directions, respectively and it is chosen a periodic domain of streamwise and spanwise direction with $L_x = 2\pi$ and $L_z = 2.416$. Following Waleffe (2003), this domain size is chosen because is possible to find the nonlinear traveling wave at the lowest Reynolds number.

In figure D.1 the comparison between the edge tracking performed in this work and that performed

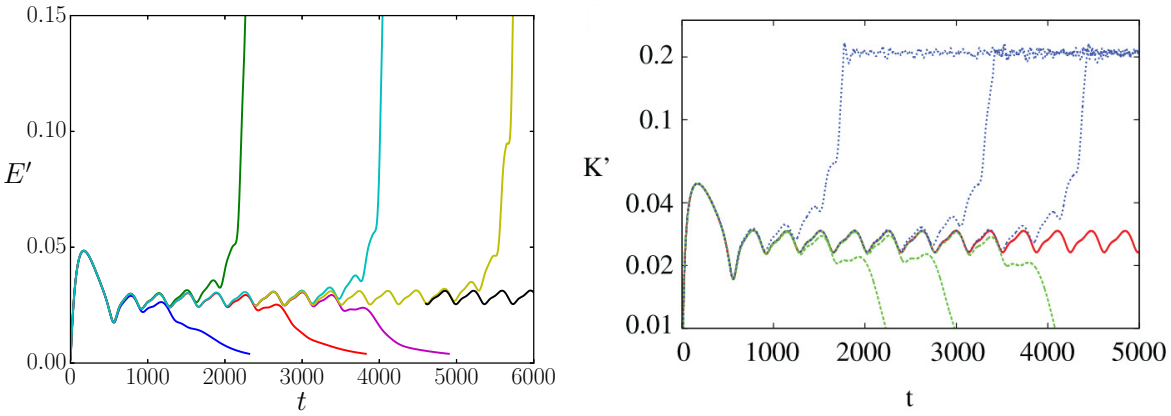

Figure D.1: Kinetic energy traces for different initial conditions: there are initial conditions that grow to reach the turbulent basin of attraction and other initial conditions that decay to the laminar solution. (Left) Edge tracking performed in the present work. (Right) Edge tracking performed by Rawat *et al.* (2014).

by Rawat *et al.* (2014) is reported. The calculations performed in this work present a good agreement with those of the reference, and both the calculations end up in a relative periodic orbit.

The relative periodic orbit compared with that of Rawat *et al.* (2014) is reported in figure D.2 in the plane $\|v'\| - \|u'\|$, where: $\|u'\| = \frac{1}{V}\int_V u' dV$ is the streamwise perturbation velocity norm and it is representative of the amplitude of streamwise streaks. While, $\|v'\| = \frac{1}{V}\int_V v' dV$ is the wall-normal perturbation velocity norm, that represents the amplitude of the quasi-streamwise vortices.

Following the counter-clocking rotation of the relative periodic orbit (see figure D.2) and starting from a point on the lower-right of the orbit, where the amplitude of the vortices is maximum and that of the streaks is at the minimum, we can find the main mechanisms that occur during the periodic orbit. In the first part of the cycle, the lift-up mechanism is the main mechanism that characterises the dynamics of the flow, because the amplitude of the vortices decays and the amplitude of the streaks

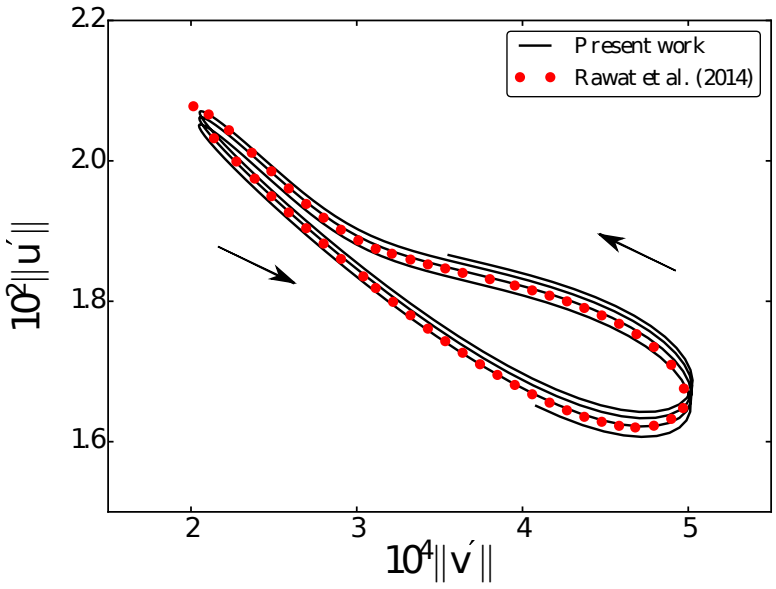

Figure D.2: Relative periodic orbit visualization in the $\|u'\|$-$\|v'\|$ plane, with $\|u'\|$ the norm of the streamwise perturbation velocity and $\|v'\|$ the norm of the wall-normal perturbation velocity.

increases. Then, when the streaks reach their maximum amplitude, they are subject to a breakdown in which their amplitude decays fast, and the vortices are regenerated. Notably, the breakdown of the streaks is faster with respect to the growth of the streamwise velocity norm, i.e. the formation of the streak. This process is the well known self-sustained process, which describes the interaction between streaks and quasi streamwise vortices (Hamilton *et al.*, 1995; Waleffe, 1997).

D.1.2 Traveling wave solution

In the previous section, the relative periodic orbit solution is computed with the perturbative Navier-Stokes equations of the laminar Poiseuille flow (2.2), presenting a good agreement with the results found by Rawat *et al.* (2014).

In this section, the edge state found by Rawat *et al.* (2016) in the form of travelling wave is computed. A converged traveling wave is found using the same initial condition used in the previous section for the relative periodic orbit with the Reynolds number $Re = 2000$, imposing a constant volume flux during the simulation and with a periodic domain of streamwise size $L_x = 2\pi$. The spanwise size is fixed at $L_z = 3.55$ because in the work of Rawat *et al.* (2016) with this dimension the edge tracking algorithm converges to a traveling wave solution and not on a relative periodic orbit.

Furthermore, they have found that continuing the relative periodic orbit and increasing the spanwise

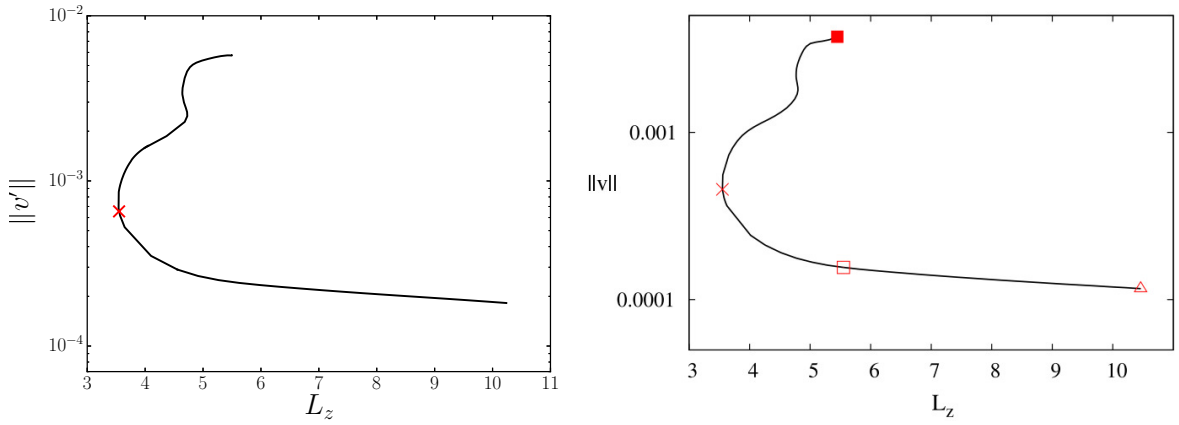

(a) (b)

Figure D.3: Continuation diagram for traveling wave solutions in respect of the spanwise domain size L_z. The red $\times$ symbol represents the saddle-node bifurcation, where the upper and lower branch start. Comparison of the present work validation (left) with Rawat *et al.* (2016) (right).

dimension, this relative periodic orbit is bifurcating into an upper and a lower branch of traveling waves via a saddle-node bifurcation at $L_z = 3.55$. In figure D.3 the bifurcation diagram is reported representing with a red $\times$ the bifurcation point. As for the previous case, the mid-plane reflection symmetry is imposed and the solution is found with $32 \times 65 \times 32$ points in the streamwise, wall-normal and spanwise directions, respectively.

In figure D.4, the traveling wave at the bifurcation point with $L_z = 3.55$ is reported. This edge-state solution is a lower branch solution and it is characterised, as is well know, by a low-speed streak (green surface in figure) surrounded by a pair of quasi streamwise vortices (red and blue surfaces corresponding to the positive and negative streamwise vorticity, respectively). Moreover, the converged traveling wave solution presents the shift and reflect symmetry

$$\{u, v, w\}(x, y, z) = \{u, v, -w\} \left(x + \frac{L_x}{2}, y, -z \right),$$

not enforced on the initial condition, for which was enforced only the midplane reflection symmetry.

The root mean square profiles of the three velocity component of the traveling wave found are computed and are compared with those found by Rawat *et al.* (2016). In figure D.5 it is shown the good agreement between our results and reference ones.

Following the paper of Rawat *et al.* (2016), the edge state found is continued increasing the spanwise domain size L_z, as it can be seen in figure D.3, and the two branches of traveling waves are found.

The comparison between the upper and lower branch solutions at fixed spanwise size $L_z = 4.5$ is

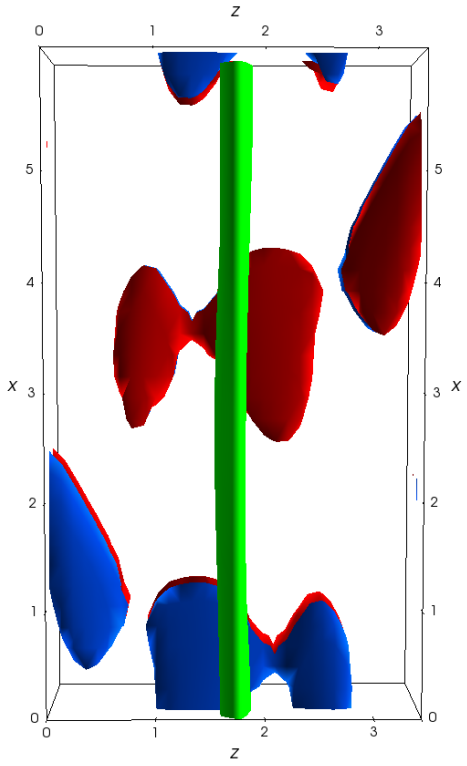

Figure D.4: Flow field associated to the traveling wave solution corresponding to the edge state al $L_z = 3.55$ (red $\times$ symbol in figure D.3). The green iso-surfaces represents $u^+ = -2$, while red and blue surfaces represent the positive and negative streamwise vorticity at $\omega_x = \pm 0.7\max(\omega_x)$.

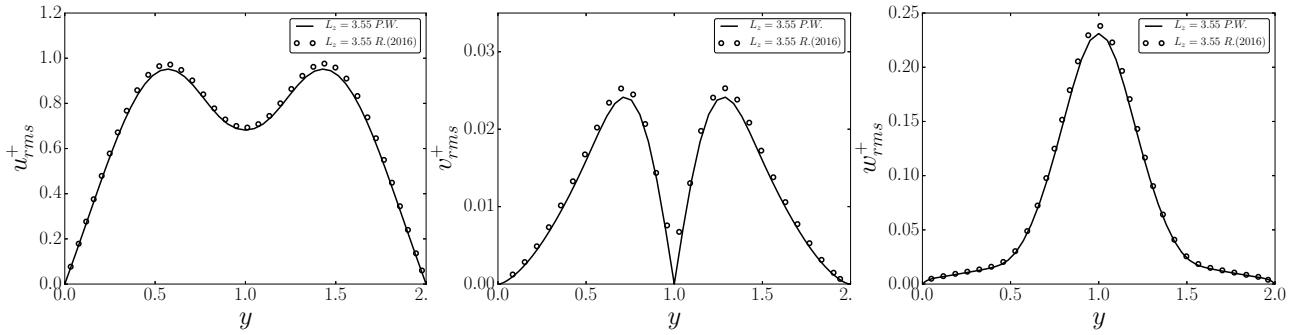

(a) (b) (c)

Figure D.5: Root mean square profiles of the three velocity components of the traveling wave at the saddle node with $Lz = 3.55$ and $Re = 2000$.

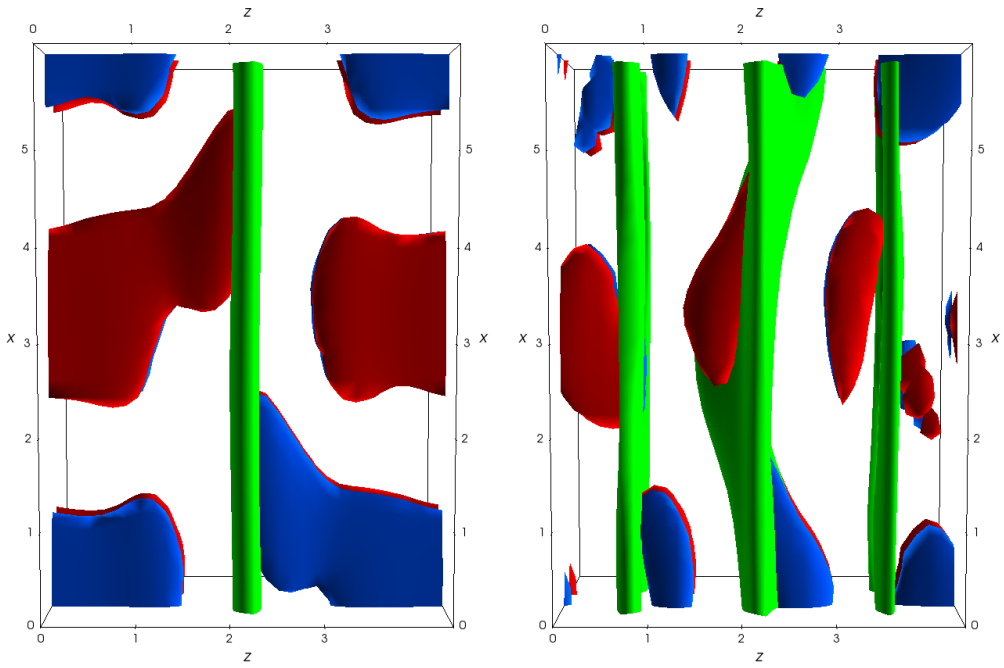

(a) (b)

Figure D.6: Flow field associated to the traveling wave solution at $L_z = 4.5$ corresponding to a lower branch solution (left) and an upper branch solution (right). The green isosurfaces represent $u^+ = -2$, while red and blue surfaces represent the positive and negative streamwise vorticity at $\omega_x = \pm 0.7\text{max}(\omega_x)$.

shown in figure D.6. As one can see, the lower branch solution is characterised by a shape similar to those of the edge state. The solution is defined by only one low-velocity streaky structure always localised in the middle of the spanwise direction and consequently, the solution presents an increased unperturbed domain region when increasing the domain spanwise size L_z. Conversely, the upper branch solution at the same spanwise domain size presents three low-speed streaky structures flanked each by a pair of streamwise vortices.

D.1.3 Turbulent eddy viscosity continuation

The lower branch and the upper branch solutions found in the previous section are continued to the Perturbative Reynold-Averaged Navier-Stokes equations (2.3) increasing the turbulent eddy viscosity as explained in section 2.1.2.1.

The results are obtained at fixed Reynolds number $Re = 2000$ and enforcing the constant volume flux with the bulk velocity $U_b = 2/3$; when the fully turbulent flow is reached the friction Reynolds number is $Re_{\tau T} = 95.025$. Further, the solutions are found in the domain of extension $2\pi \times 2 \times 4.5$, with $32 \times 65 \times 32$ points in the streamwise, wall-normal and spanwise direction, respectively. Moreover, in the continuation is imposed the symmetry that characterises the traveling wave solution, i.e. the shift and reflect symmetry.

The solutions obtained for $\epsilon = 1$, computed with the turbulent eddy viscosity of the fully developed turbulent flow, are shown in figure D.7. Comparing these solutions with those found around the laminar Poiseuille baseflow, it is notable that the perturbations around the mean flow present the same quasi streamwise vortices. As far as the low velocity streaks, in this case, the lower branch solution presents only one streaky structure, instead, the upper branch solution is characterised by an increased number of streaks. Furthermore, it is notable that the low velocity streaks present a changed shape. They are more diffused since the viscosity is increased adding the turbulent eddy viscosity term, and they have moved towards the walls because increasing the turbulent viscosity the mean flow is increasingly distorted.

D.1.4 Travelling wave solution at $Re_\tau = 180$

In this section, a travelling-wave solution found initialising with an optimal perturbation found at Re_τ with $Re = 3300$ and $U_{bulk} = 0.848484$ is shown.

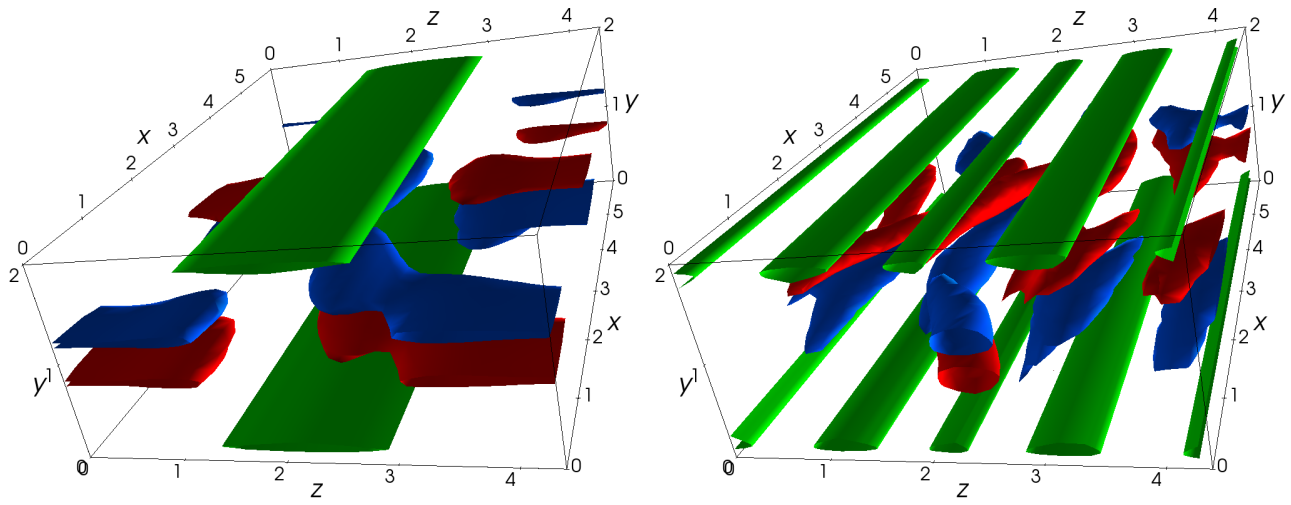

(a) (b)

Figure D.7: Flow field associated to the traveling wave solution at $L_z = 4.5$ corresponding to a lower branch solution (left) and an upper branch solution (right) around the mean turbulent fully developed flow. The green isosurfaces represents $u^+ = -8$, while red and blue surfaces represent the positive and negative streamwise vorticity at $\omega_x = \pm 0.7\text{max}(\omega_x)$.

Scientific production

- Parente E., Robinet J. C., De Palma P. & Cherubini S. "Modal and nonmodal stability of a stably stratified boundary layer flow", *Physical Review Fluids* (2020).
- Parente E., Farano M., Robinet J. C., De Palma P. & Cherubini S., "Continuing invariant solutions towards the turbulent flow" (submitted to *Philosophical Transactions A*) [Chapter 3]
- Parente E., Robinet J. C., De Palma P. & Cherubini S. "Minimal seeds for turbulent bands in channel flow" (submitted to *Journal of Fluid Mechanics*) [Chapter 4]
- Parente E., Robinet J. C., De Palma P. & Cherubini S."Linear and nonlinear optimal growth mechanisms for generating turbulent bands" (submitted to *Journal of Fluid Mechanics Rapid*) [Chapter 6]

Bibliography

Adrian, Ronald J 2007 Hairpin vortex organization in wall turbulence. *Physics of Fluids* **19** (4), 041301.

Aida, Hiroshi, Tsukahara, Takahiro & Kawaguchi, Yasuo 2010 Dns of turbulent spot developing into turbulent stripe in plane poiseuille flow. In *Fluids Engineering Division Summer Meeting*, , vol. 49484, pp. 2125–2130.

Aida, Hiroshi, Tsukahara, Takahiro & Kawaguchi, Yasuo 2011 Development of a turbulent spot into a stripe pattern in plane poiseuille flow. In *Seventh International Symposium on Turbulence and Shear Flow Phenomena*. Begel House Inc.

del Alamo, Juan C. & Jiménez, Javier 2003 Spectra of the very large anisotropic scales in turbulent channels. *Physics of Fluids* **15** (6), L41–L44.

Avila, Kerstin, Moxey, David, de Lozar, Alberto, Avila, Marc, Barkley, Dwight & Hof, Björn 2011 The onset of turbulence in pipe flow. *Science* **333** (6039), 192–196.

Azimi, S., Cossu, C. & Schneider, T 2020 Self-sustained large-scale motions in the asymptotic suction boundary layer. *https://arxiv.org/abs/2004.08862* .

Barkley, Dwight & Tuckerman, Laurette S 2005 Computational study of turbulent laminar patterns in couette flow. *Physical review letters* **94** (1), 014502.

Barkley, D. & Tuckerman, L. S. 2007 Mean flow of turbulent–laminar patterns in plane couette flow. *Journal of Fluid Mechanics* **576**, 109–137.

Barnett, Joshua, Gurevich, Daniel R & Grigoriev, Roman O 2017 Streamwise localization of traveling wave solutions in channel flow. *Physical Review E* **95** (3), 033124.

Budanur, NB, Short, Kimberly Y, Farazmand, Mohammad, Willis, Ashley P & Cvitanović, P 2017 Relative periodic orbits form the backbone of turbulent pipe flow. *Journal of Fluid Mechanics* **833**, 274–301.

Butler, Kathryn M & Farrell, Brian F 1992 Three-dimensional optimal perturbations in viscous shear flow. *Physics of Fluids A: Fluid Dynamics* **4** (8), 1637–1650.

Butler, K. M. & Farrell, B. F. 1993 Optimal perturbations and streak spacing in wall-bounded turbulent shear flow. *Physics of Fluids A* **5** (3), 774–777.

Cantwell, Brian, Coles, Donald & Dimotakis, Paul 1978 Structure and entrainment in the plane of symmetry of a turbulent spot. *Journal of Fluid Mechanics* **87** (4), 641–672.

Carlson, Dale R, Widnall, Sheila E & Peeters, Martin F 1982 A flow-visualization study of transition in plane poiseuille flow. *Journal of Fluid Mechanics* **121**, 487–505.

Cess, RD 1958 A survey of the literature on heat transfer in turbulent tube flow. *Res. Rep* pp. 8–0529.

Chandler, Gary J & Kerswell, Rich R 2013 Invariant recurrent solutions embedded in a turbulent two-dimensional kolmogorov flow. *Journal of Fluid Mechanics* **722**, 554–595.

Chen, Xi, Hussain, Fazle & She, Zhen-Su 2018 Quantifying wall turbulence via a symmetry approach. part 2. reynolds stresses. *Journal of Fluid Mechanics* **850**, 401–438.

Cherubini, Stefania & De Palma, Pietro 2013 Nonlinear optimal perturbations in a couette flow: bursting and transition. *Journal of Fluid Mechanics* **716**, 251–279.

Cherubini, Stefania, De Palma, Pietro & Robinet, Jean-Christophe 2015 Nonlinear optimals in the asymptotic suction boundary layer: Transition thresholds and symmetry breaking. *Physics of Fluids* **27** (3), 034108.

Cherubini, Stefania, De Palma, Pietro, Robinet, J-Ch & Bottaro, Alessandro 2010*a* Rapid path to transition via nonlinear localized optimal perturbations in a boundary-layer flow. *Physical Review E* **82** (6), 066302.

Cherubini, Stefania, De Palma, Pietro, Robinet, J-C & Bottaro, Alessandro 2011 The minimal seed of turbulent transition in the boundary layer. *Journal of Fluid Mechanics* **689**, 221–253.

Cherubini, S., Robinet, J.-C., Bottaro, A. & De Palma, P. 2010*b* Optimal wave packets in a boundary layer and initial phases of a turbulent spot. *Journal of Fluid Mechanics* **656**, 231–259.

Cho, Minjeong, Hwang, Yongyun & Choi, Haecheon 2018 Scale interactions and spectral energy transfer in turbulent channel flow. *Journal of Fluid Mechanics* **854**, 474–504.

Cimarelli, A., De Angelis, E., Jiménez, J. & Casciola, C. M. 2016 Cascades and wall-normal fluxes in turbulent channel flows. *Journal of Fluid Mechanics* **796**, 417–436.

Coddington, EL & Levinson, N 1995 Theory of ordinary differential equations.

Coles, Donald & Van Atta, Charles 1966 Progress report on a digital experiment in spiral turbulence. *AIAA Journal* **4** (11), 1969–1971.

Cossu, Carlo & Hwang, Yongyun 2017 Self-sustaining processes at all scales in wall-bounded turbulent shear flows. *Philosophical Transactions of the Royal Society A: Mathematical, Physical and Engineering Sciences* **375** (2089), 20160088, arXiv: https://royalsocietypublishing.org/doi/pdf/10.1098/rsta.2016.0088.

Cossu, C., Pujals, G. & Depardon, S. 2009 Optimal transient growth and very large–scale structures in turbulent boundary layers. *Journal of Fluid Mechanics* **619**, 79–94.

Cvitanović, Predrag 2013 Recurrent flows: the clockwork behind turbulence. *Journal of Fluid Mechanics* **726**, 1–4.

Dean, Roger Bruce 1978 Reynolds number dependence of skin friction and other bulk flow variables in two-dimensional rectangular duct flow. *Journal of Fluid Mechanics* .

Deguchi, Kengo, Hall, Philip & Walton, Andrew 2013 The emergence of localized vortex–wave interaction states in plane couette flow. *Journal of Fluid Mechanics* **721**, 58–85.

Deusebio, Enrico, Caulfield, CP & Taylor, John R 2015 The intermittency boundary in stratified plane couette flow. *Journal of Fluid Mechanics* **781**, 298–329.

Doohan, Patrick, Willis, Ashley P. & Hwang, Yongyun 2021 Minimal multi-scale dynamics of near-wall turbulence. *Journal of Fluid Mechanics* **913**, A8.

Duguet, Yohann, Monokrousos, Antonios, Brandt, Luca & Henningson, Dan S 2013 Minimal transition thresholds in plane couette flow. *Physics of Fluids* **25** (8), 084103.

Duguet, Yohann, Pringle, Chris CT & Kerswell, Rich R 2008 Relative periodic orbits in transitional pipe flow. *Physics of Fluids* **20** (11), 114102.

Duguet, Y. & Schlatter, P. 2013 Oblique laminar-turbulent interfaces in plane shear flows. *Phys Rev Lett.* **110**, 034502.

Duguet, Yohann, Schlatter, Philipp & Henningson, Dan S 2010 Formation of turbulent patterns near the onset of transition in plane couette flow. *Journal of Fluid Mechanics* **650**, 119.

Eckhardt, Bruno, Schneider, Tobias M, Hof, Bjorn & Westerweel, Jerry 2007 Turbulence transition in pipe flow. *Annu. Rev. Fluid Mech.* **39**, 447–468.

Eitel-Amor, Georg, Örlü, Ramis, Schlatter, Philipp & Flores, O 2015 Hairpin vortices in turbulent boundary layers. *Physics of Fluids* **27** (2), 025108.

Emmons, Howard W 1951 The laminar-turbulent transition in a boundary layer-part i. *Journal of the Aeronautical Sciences* **18** (7), 490–498.

Faisst, Holger & Eckhardt, Bruno 2003 Traveling waves in pipe flow. *Physical Review Letters* **91** (22), 224502.

Farano, M., Cherubini, S., De Palma, P. & Robinet, J.-C. 2018 Nonlinear optimal large-scale structures in turbulent channel flow. *European Journal of Mechanics - B/Fluids* **72**, 74–86.

Farano, Mirko, Cherubini, Stefania, Robinet, Jean-Christophe & De Palma, Pietro 2015 Hairpin-like optimal perturbations in plane poiseuille flow. *Journal of Fluid Mechanics* **775**, R2.

Farano, Mirko, Cherubini, Stefania, Robinet, Jean-Christophe & De Palma, Pietro 2016 Subcritical transition scenarios via linear and nonlinear localized optimal perturbations in plane poiseuille flow. *Fluid Dynamics Research* **48** (6), 061409.

Farano, Mirko, Cherubini, Stefania, Robinet, Jean-Christophe & De Palma, Pietro 2017 Optimal bursts in turbulent channel flow. *Journal of Fluid Mechanics* .

Farano, M., Cherubini, S., Robinet, J.-C., De Palma, P. & Schneider, T. M. 2019 Computing heteroclinic orbits using adjoint-based methods. *Journal of Fluid Mechanics* **858**, R3.

Farrell, Brian F 1988 Optimal excitation of perturbations in viscous shear flow. *The Physics of fluids* **31** (8), 2093–2102.

Foures, D. P. G., Caulfield, C. P. & Schmid, P. J. 2013 Localization of flow structures using ∞ -norm optimization. *Journal of Fluid Mechanics* **729**, 672–701.

Gibson, JF & Brand, E 2014 Spanwise-localized solutions of planar shear flows. *Journal of Fluid Mechanics* **745**, 25–61.

Gibson, John F, Halcrow, Jonathan & Cvitanović, Predrag 2009 Equilibrium and travelling-wave solutions of plane couette flow. *Journal of Fluid Mechanics* **638**, 243–266.

Gibson, J. F., Reetz, F., Azimi, S., Ferraro, A., Kreilos, T., Schrobsdorff, H., Farano, M., Yesil, A. F., Schutz, S. S., Culpo, M. & Schneider, T. M 2021 Channelflow 2.0. *in preparation* .

de Giovanetti, Matteo, Sung, Hyung Jin & Hwang, Yongyun 2017 Streak instability in turbulent channel flow: the seeding mechanism of large-scale motions. *Journal of Fluid Mechanics* **832**, 483–513.

Griewank, Andreas & Walther, Andrea 2000 Algorithm 799: revolve: an implementation of checkpointing for the reverse or adjoint mode of computational differentiation. *ACM Transactions on Mathematical Software (TOMS)* **26** (1), 19–45.

Hamilton, J. M., Kim, J. & Waleffe, F. 1995 Regeneration mechanisms of near-wall turbulence structures. *Journal of Fluid Mechanics* **287**, 317–348.

Henningson, Dan, Spalart, Philippe & Kim, John 1987 Numerical simulations of turbulent spots in plane poiseuille and boundary-layer flow. *The Physics of fluids* **30** (10), 2914–2917.

Henningson, Dan S & Kim, John 1991 On turbulent spots in plane poiseuille flow. *Journal of fluid mechanics* **228**, 183–205.

Henningson, Dan S, Lundbladh, Anders & Johansson, Arne V 1993 A mechanism for bypass transition from localized disturbances in wall-bounded shear flows. *Journal of Fluid Mechanics* **250**, 169–207.

Hinze, Michael, Walther, Andrea & Sternberg, Julia 2006 An optimal memory-reduced procedure for calculating adjoints of the instationary navier-stokes equations. *Optimal Control Applications and Methods* **27** (1), 19–40.

Hof, Björn, Van Doorne, Casimir WH, Westerweel, Jerry, Nieuwstadt, Frans TM, Faisst, Holger, Eckhardt, Bruno, Wedin, Hakan, Kerswell, Richard R & Waleffe, Fabian 2004 Experimental observation of nonlinear traveling waves in turbulent pipe flow. *Science* **305** (5690), 1594–1598.

Hopf, Eberhard 1948 A mathematical example displaying features of turbulence. *Communications on Pure and Applied Mathematics* **1** (4), 303–322.

Hutchins, N & Marusic, Ivan 2007 Evidence of very long meandering features in the logarithmic region of turbulent boundary layers. *Journal of Fluid Mechanics* **579**, 1–28.

Hwang, J., Lee, J., Sung, H. J. & Zaki, T. A. 2016*a* Inner–outer interactions of large-scale structures in turbulent channel flow. *Journal of Fluid Mechanics* **790**, 128–157.

Hwang, Yongyun 2015 Statistical structure of self-sustaining attached eddies in turbulent channel flow. *Journal of Fluid Mechanics* **767**, 254–289.

Hwang, Yongyun 2016 Mesolayer of attached eddies in turbulent channel flow. *Physical Review Fluids* **1** (6), 064401.

Hwang, Yongyun & Cossu, Carlo 2010*a* Amplification of coherent streaks in the turbulent couette flow: an input-output analysis at low reynolds number. *Journal of Fluid Mechanics* **643**, 333–348.

Hwang, Yongyun & Cossu, Carlo 2010*b* Self-sustained process at large scales in turbulent channel flow. *Phys. Rev. Lett.* **105**, 044505.

Hwang, Yongyun & Cossu, Carlo 2011 Self-sustained processes in the logarithmic layer of turbulent channel flows. *Physics of Fluids* **23** (6), 061702.

Hwang, Yongyun, Willis, Ashley P. & Cossu, Carlo 2016*b* Invariant solutions of minimal large-scale structures in turbulent channel flow for re_τ up to 1000. *Journal of Fluid Mechanics* **802**, R1.

Itano, Tomoaki & Toh, Sadayoshi 2001 The dynamics of bursting process in wall turbulence. *Journal of the Physical Society of Japan* **70** (3), 703–716.

Jiménez, Javier & Pinelli, Alfredo 1999 The autonomous cycle of near-wall turbulence. *Journal of Fluid Mechanics* **389**, 335–359.

Kashyap, Pavan V, Duguet, Yohann & Dauchot, Olivier 2020 Flow statistics in the transitional regime of plane channel flow. *Entropy* **22** (9), 1001.

Kawahara, Genta & Kida, Shigeo 2001 Periodic motion embedded in plane couette turbulence: regeneration cycle and burst. *Journal of Fluid Mechanics* **449**, 291–300.

Keller, Herbert B 1987 Lectures on numerical methods in bifurcation problems. *Applied Mathematics* **217**, 50.

Kendall, J 1985 Experimental study of disturbances produced in a pre-transitional laminar boundary layer by weak freestream turbulence. In *18th Fluid Dynamics and Plasmadynamics and Lasers Conference*, p. 1695.

Kerswell, R.R. 2018 Nonlinear nonmodal stability theory. *Annual Review of Fluid Mechanics* **50** (1), 319–345.

Kerswell, R. R., Pringle, C. C. T. & Willis, A. P. 2014 An optimisation approach for analysing nonlinear stability with transition to turbulence in fluids as an exemplar . *Rep. Prog. Phys.* **77**, 085901.

Kim, John, Moin, Parviz & Moser, Robert 1987 Turbulence statistics in fully developed channel flow at low reynolds number. *Journal of fluid mechanics* **177**, 133–166.

Kim, K. C. & Adrian, R. J. 1999 Very large-scale motion in the outer layer. *Physics of Fluids* **11** (2), 417–422, arXiv: https://doi.org/10.1063/1.869889.

Kline, Stephen J, Reynolds, William C, Schraub, FA & Runstadler, PW 1967 The structure of turbulent boundary layers. *Journal of Fluid Mechanics* **30** (4), 741–773.

Klingmann, Barbro GB 1992 On transition due to three-dimensional disturbances in plane poiseuille flow. *Journal of Fluid Mechanics* **240**, 167–195.

Komminaho, Jukka, Lundbladh, Anders & Johansson, Arne V. 1996 Very large structures in plane turbulent couette flow. *Journal of Fluid Mechanics* **320**, 259–285.

Kovasznay, Leslie S. G., Kibens, Valdis & Blackwelder, Ron F. 1970 Large-scale motion in the intermittent region of a turbulent boundary layer. *Journal of Fluid Mechanics* **41** (2), 283–325.

Kreilos, Tobias 2014 *Turbulence Transition in Shear Flows and Dynamical Systems Theory*. Philipps-Universität Marburg.

Kreilos, Tobias, Veble, Gregor, Schneider, Tobias M & Eckhardt, Bruno 2013 Edge states for the turbulence transition in the asymptotic suction boundary layer. *Journal of Fluid Mechanics* **726**, 100–122.

Kunii, Kohei, Ishida, Takahiro, Duguet, Yohann & Tsukahara, Takahiro 2019 Laminar–turbulent coexistence in annular couette flow. *Journal of Fluid Mechanics* **879**, 579–603.

Lagha, Maher & Manneville, Paul 2007 Modeling of plane couette flow. i. large scale flow around turbulent spots. *Physics of Fluids* **19** (9), 094105.

Landahl, MT 1980 A note on an algebraic instability of inviscid parallel shear flows. *Journal of Fluid Mechanics* **98** (2), 243–251.

Lee, J., Lee, J., Choi, J. & Sung, H. 2014 Spatial organization of large- and very-large-scale motions in a turbulent channel flow. *Journal of Fluid Mechanics* **749**, 818–840.

Lemoult, Grégoire, Aider, Jean-Luc & Wesfreid, José Eduardo 2013 Turbulent spots in a channel: large-scale flow and self-sustainability. *J. Fluid Mech* **731**, R1.

Lemoult, Grégoire, Gumowski, Konrad, Aider, Jean-Luc & Wesfreid, José Eduardo 2014 Turbulent spots in channel flow: an experimental study. *The European Physical Journal E* **37** (4), 1–11.

Levin, Ori & Henningson, Dan S 2007 Turbulent spots in the asymptotic suction boundary layer. *Journal of Fluid Mechanics* **584**, 397–413.

Liu, J., Xiao, Y., Zhang, L., Li, M., Tao, J. & Xu, S. 2020 Extension at the downstream end of turbulent band in channel flow. *Physics of Fluids* **32** (12), 121703.

Luchini, P. 2000 Reynolds-number-independent instability of the boundary layer over a flat surface: optimal perturbations. *Journal of Fluid Mechanics* **404**, 289–309.

Marensi, Elena, Willis, Ashley P. & Kerswell, Rich R. 2019 Stabilisation and drag reduction of pipe flows by flattening the base profile. *Journal of Fluid Mechanics* **863**, 850–875.

Matsubara, M & Alfredsson, P Henrik 2001 Disturbance growth in boundary layers subjected to free-stream turbulence. *Journal of fluid mechanics* **430**, 149–168.

Monokrousos, Antonios, Bottaro, Alessandro, Brandt, Luca, Di Vita, Andrea & Henningson, Dan S 2011 Nonequilibrium thermodynamics and the optimal path to turbulence in shear flows. *Physical Review Letters* **106** (13), 134502.

Moser, Robert D, Kim, John & Mansour, Nagi N 1999 Direct numerical simulation of turbulent channel flow up to re τ= 590. *Physics of fluids* **11** (4), 943–945.

Nagata, M 1990 Three-dimensional finite-amplitude solutions in plane couette flow: bifurcation from infinity. *Journal of Fluid Mechanics* **217**, 519–527.

Nayfeh, Ali H & Balachandran, Balakumar 2008 *Applied nonlinear dynamics: analytical, computational, and experimental methods*. John Wiley & Sons.

Olvera, Daniel & Kerswell, Rich R 2017 Optimizing energy growth as a tool for finding exact coherent structures. *Physical Review Fluids* **2** (8), 083902.

Orr, William M'F 1907 The stability or instability of the steady motions of a perfect liquid and of a viscous liquid. part ii: A viscous liquid. In *Proceedings of the Royal Irish Academy. Section A: Mathematical and Physical Sciences*, , vol. 27, pp. 69–138. JSTOR.

Orszag, Steven A 1971 Accurate solution of the orr–sommerfeld stability equation. *Journal of Fluid Mechanics* **50** (4), 689–703.

Paranjape, C 2019 Onset of turbulence in plane poiseuille flow. PhD thesis, PhD thesis, Institute of Science and Technology Austria.

Paranjape, Chaitanya S, Duguet, Yohann & Hof, Björn 2020 Oblique stripe solutions of channel flow. *Journal of Fluid Mechanics* **897**.

Parente, E., Robinet, J.C., De Palma, P. & Cherubini, S. 2021*a* Minimal seeds for turbulent bands. *submitted to Journal of Fluid Mechanics, arXiv:2107.10157* .

Parente, Enza, Robinet, J-Ch, De Palma, Pietro & Cherubini, Stefania 2021*b* Linear and nonlinear optimal growth mechanisms for generating turbulent bands. *submitted to Journal of Fluid Mechanics, arXiv:2107.10191* .

Park, Jae Sung & Graham, Michael D. 2015 Exact coherent states and connections to turbulent dynamics in minimal channel flow. *Journal of Fluid Mechanics* **782**, 430–454.

Pope, Stephen B 2001 Turbulent flows.

Prigent, Arnaud, Grégoire, Guillaume, Chaté, Hugues, Dauchot, Olivier & van Saarloos, Wim 2002 Large-scale finite-wavelength modulation within turbulent shear flows. *Physical review letters* **89** (1), 014501.

Pringle, Chris CT & Kerswell, Rich R 2010 Using nonlinear transient growth to construct the minimal seed for shear flow turbulence. *Physical Review Letters* **105** (15), 154502.

Pringle, Chris CT, Willis, Ashley P & Kerswell, Rich R 2012 Minimal seeds for shear flow turbulence: using nonlinear transient growth to touch the edge of chaos. *Journal of Fluid Mechanics* **702**, 415–443.

Pujals, Gregory, García-Villalba, Manuel, Cossu, Carlo & Depardon, Sebastien 2009 A note on optimal transient growth in turbulent channel flows. *Physics of fluids* **21** (1), 015109.

Rabin, SME, Caulfield, CP & Kerswell, RR 2012 Triggering turbulence efficiently in plane couette flow. *Journal of Fluid Mechanics* **712**, 244–272.

Rabin, SME, Caulfield, CP & Kerswell, RR 2014 Designing a more nonlinearly stable laminar flow via boundary manipulation. *Journal of Fluid Mechanics* **738**.

Rawat, Subhandu, Cossu, Carlo, Hwang, Yongyun & Rincon, François 2015 On the self-sustained nature of large-scale motions in turbulent couette flow. *Journal of Fluid Mechanics* **782**, 515–540.

Rawat, Subhendu, Cossu, Carlo & Rincon, François 2014 Relative periodic orbits in plane poiseuille flow. *Comptes Rendus Mécanique* **342** (8), 485–489.

Rawat, Subhandu, Cossu, Carlo & Rincon, François 2016 Travelling-wave solutions bifurcating from relative periodic orbits in plane poiseuille flow. *Comptes Rendus Mécanique* **344** (6), 448–455.

Reddy, Satish C & Henningson, Dan S 1993 Energy growth in viscous channel flows. *Journal of Fluid Mechanics* **252**, 209–238.

Reddy, Satish C, Schmid, Peter J, Baggett, Jeffrey S & Henningson, Dan S 1998 On stability of streamwise streaks and transition thresholds in plane channel flows. *Journal of Fluid Mechanics* **365**, 269–303.

Reynolds, Osborne 1883 Iii. an experimental investigation of the circumstances which determine whether the motion of water shall be direct or sinuous, and of the law of resistance in parallel channels. *Proceedings of the royal society of London* **35** (224-226), 84–99.

Reynolds, WC & Hussain, AKMF 1972 The mechanics of an organized wave in turbulent shear flow. part 3. theoretical models and comparisons with experiments. *Journal of Fluid Mechanics* **54** (2), 263–288.

Reynolds, WC & Tiederman, WG 1967 Stability of turbulent channel flow, with application to malkus's theory. *Journal of Fluid Mechanics* **27** (2), 253–272.

Schneider, Tobias M 2007 State space properties of transitional pipe flow. *Tech. Rep.*. Sierke.

Schneider, Tobias M, Gibson, John F & Burke, John 2010 Snakes and ladders: localized solutions of plane couette flow. *Physical Review Letters* **104** (10), 104501.

Schneider, Tobias M, Gibson, John F, Lagha, Maher, De Lillo, Filippo & Eckhardt, Bruno 2008 Laminar-turbulent boundary in plane couette flow. *Physical Review E* **78** (3), 037301.

Schumacher, Jörg & Eckhardt, Bruno 2001 Evolution of turbulent spots in a parallel shear flow. *Physical Review E* **63** (4), 046307.

Shimizu, Masaki & Manneville, Paul 2019 Bifurcations to turbulence in transitional channel flow. *Physical Review Fluids* **4** (11), 113903.

Singer, Bart A & Joslin, Ronald D 1994 Metamorphosis of a hairpin vortex into a young turbulent spot. *Physics of Fluids* **6** (11), 3724–3736.

Skufca, Joseph D, Yorke, James A & Eckhardt, Bruno 2006 Edge of chaos in a parallel shear flow. *Physical review letters* **96** (17), 174101.

Smith, C. R. & Metzler, S. P. 1983 The characteristics of low-speed streaks in the near-wall region of a turbulent boundary layer. *Journal of Fluid Mechanics* **129**, 27–54.

Song, Baofang, Barkley, Dwight, Hof, Björn & Avila, Marc 2017 Speed and structure of turbulent fronts in pipe flow. *Journal of Fluid Mechanics* **813**, 1045–1059.

Song, Baofang & Xiao, Xiangkai 2020 Trigger turbulent bands directly at low reynolds numbers in channel flow using a moving-force technique. *Journal of Fluid Mechanics* **903**, A43.

Tao, JJ, Eckhardt, Bruno & Xiong, XM 2018 Extended localized structures and the onset of turbulence in channel flow. *Physical Review Fluids* **3** (1), 011902.

Tao, Jianjun & Xiong, Xiangming 2013 The unified transition stages in linearly stable shear flows. *Fourteenth Asia Congress of Fluid Mechanics, Hanoi and Halong, Oct. 15-19* .

Tao, Jianjun & Xiong, Xiangming 2017 The unified transition stages in linearly stable shear flows. *arXiv preprint arXiv:1710.02258* .

Toh, Sadayoshi & Itano, Tomoaki 2003 A periodic-like solution in channel flow. *Journal of Fluid Mechanics* **481**, 67–76.

Tomkins, C. D. & Adrian, R. J. 2003 Spanwise structure and scale growth in turbulent boundary layers. *Journal of Fluid Mechanics* **490**, 37–74.

Townsend, A. 1980 *The structure of turbulent shear flow,*. Cambridge University Press, UK.

Trefethen, Lloyd N, Trefethen, Anne E, Reddy, Satish C & Driscoll, Tobin A 1993 Hydrodynamic stability without eigenvalues. *Science* **261** (5121), 578–584.

Tsukahara, Takahiro, Iwamoto, Kaoru, Kawamura, Hiroshi & Takeda, T 2006 Dns of heat transfer in a transitional channel flow accompanied by a turbulent puff-like structure. In *Turbulence Heat and Mass Transfer 5. Proceedings of the International Symposium on Turbulence Heat and Mass Transfer*. Begel House Inc.

Tsukahara, Takahiro, Kawaguchi, Yasuo & Kawamura, Hiroshi 2014 An experimental study on turbulent-stripe structure in transitional channel flow. *arXiv preprint arXiv:1406.1378* .

Tsukahara, Takahiro, Seki, Yohji, Kawamura, Hiroshi & Tochio, Daisuke 2005 Dns of turbulent channel flow at very low reynolds numbers. In *Fourth International Symposium on Turbulence and Shear Flow Phenomena*. Begel House Inc.

Tuckerman, Laurette S & Barkley, Dwight 2011 Patterns and dynamics in transitional plane couette flow. *Physics of Fluids* **23** (4), 041301.

Tuckerman, Laurette S, Chantry, Matthew & Barkley, Dwight 2020 Patterns in wall-bounded shear flows. *Annual Review of Fluid Mechanics* **52**.

Tuckerman, Laurette S, Kreilos, Tobias, Schrobsdorff, Hecke, Schneider, Tobias M & Gibson, John F 2014 Turbulent-laminar patterns in plane poiseuille flow. *Physics of Fluids* **26** (11), 114103.

Vavaliaris, Chris, Beneitez, Miguel & Henningson, Dan S 2020 Optimal perturbations and transition energy thresholds in boundary layer shear flows. *Physical Review Fluids* **5** (6), 062401.

Viswanath, D 2008 The dynamics of transition to turbulence in plane couette flow. In *Mathematics and Computation, A Contemporary View*, pp. 109–127. Springer.

Waleffe, Fabian 1995 Hydrodynamic stability and turbulence: Beyond transients to a self-sustaining process. *Studies in applied mathematics* **95** (3), 319–343.

Waleffe, F. 1997 On a self-sustaining process in shear flows . *Phys. Fluids* **9**, 883–901.

Waleffe, Fabian 1998 Three-dimensional coherent states in plane shear flows. *Physical Review Letters* **81** (19), 4140.

Waleffe, Fabian 2001 Exact coherent structures in channel flow. *Journal of Fluid Mechanics* **435**, 93–102.

Waleffe, Fabian 2003 Homotopy of exact coherent structures in plane shear flows. *Physics of Fluids* **15** (6), 1517–1534.

Wang, Zhe, Guet, Claude, Monchaux, Romain, Duguet, Yohann & Eckhardt, Bruno 2020 Quadrupolar flows around spots in internal shear flows. *Journal of Fluid Mechanics* **892**, A27.

Wedin, Hakan & Kerswell, RR 2004 Exact coherent structures in pipe flow: travelling wave solutions. *Journal of Fluid Mechanics* **508**, 333–371.

Willis, Ashley P, Cvitanović, P & Avila, Marc 2013 Revealing the state space of turbulent pipe flow by symmetry reduction. *Journal of Fluid Mechanics* **721**, 514–540.

Xiao, Xiangkai & Song, Baofang 2020 The growth mechanism of turbulent bands in channel flow at low reynolds numbers. *Journal of Fluid Mechanics* **883**.

Xiong, Xiangming, Tao, Jianjun, Chen, Shiyi & Brandt, Luca 2015 Turbulent bands in plane-poiseuille flow at moderate reynolds numbers. *Physics of Fluids* **27** (4), 041702.

Zammert, Stefan & Eckhardt, Bruno 2014 Streamwise and doubly-localised periodic orbits in plane poiseuille flow. *Journal of Fluid Mechanics* **761**, 348–359.

Zikanov, Oleg, Krasnov, Dmitry, Boeck, Thomas, Thess, Andre & Rossi, Maurice 2014 Laminar-turbulent transition in magnetohydrodynamic duct, pipe, and channel flows. *Applied Mechanics Reviews* **66** (3).

Zuccher, Simone, Luchini, Paolo & Bottaro, Alessandro 2004 Algebraic growth in a blasius boundary layer: optimal and robust control by mean suction in the nonlinear regime. *Journal of Fluid Mechanics* **513**, 135.

del Álamo, Juan C. & Jiménez, Javier 2006 Linear energy amplification in turbulent channels. *Journal of Fluid Mechanics* **559**, 205–213.

Enza PARENTE

Sustaining turbulent bands and fully-developed turbulence in channel flow

Résumé : Cette thèse vise à étudier les principaux mécanismes impliqués dans les écoulements de type canal autour de la transition vers la turbulence. Plus particulièrement, il existe une gamme de nombres de Reynolds pour laquelle la turbulence reste localisée sous la forme de bandes obliques turbulentes plongées dans un écoulement laminaire. Dans cette thèse, les principaux mécanismes à l'origine et responsables de l'évolution de ces bandes turbulentes sont étudiés au travers de techniques d'optimisation linéaires et non linéaires. Tout d'abord, dans un canal de grande dimension, il a été démontré que la perturbation d'énergie minimale capable de générer des bandes turbulentes est localisée et caractérisée par des structures à petite et grande échelles. Selon le nombre de Reynolds, ce *minimal seed* évolue dans le temps avec deux mécanismes différents : pour $Re \lesssim 1200$ une bande oblique isolée est créée ; alors que pour $Re \gtrsim 1200$, une évolution symétrique dans la direction transverse est observée, donnant lieu à deux bandes distinctes. Ensuite, en réduisant la complexité du problème à un domaine incliné, on constate que deux éléments principaux sont nécessaires pour induire la transition vers des bandes turbulentes : i) un mécanisme linéaire de type *lift-up* est nécessaire à la génération des *streaks* à l'intérieur des bandes turbulentes ; ii) des tourbillons à grande échelle assurant la localisation spatiale.
Dans la dernière partie de cette thèse, afin d'étudier les structures cohérentes habituellement observées dans les écoulements turbulents, la méthode d'optimisation non linéaire est étendue aux écoulements de canal turbulent et une 'nouvelle' méthode mathématique pour le calcul des solutions cohérentes invariantes est proposées. Dans ces deux méthodes, les équations instationnaires de Navier-Stokes sont écrites en moyenne de Reynolds et sous une forme perturbative autour du champ moyen turbulent ; des solutions en termes de structures à différentes échelles turbulentes sont trouvées.

Mots clés : bandes turbulentes, transition sous-critique, optimisation non-linéaire, écoulement turbulent, structures cohérentes, système dynamique.

Abstract : This thesis aims at studying the main mechanisms involved in transitional and turbulent channel flows. Concerning the transitional channel flow, there is a range of Reynolds numbers for which turbulent oblique bands plunged in the laminar flow are observed. In this thesis, the main mechanisms involved in the origin and growth of these turbulent bands are investigated using linear and nonlinear optimization techniques. First, in a large-sized channel, it is shown that the minimal-energy perturbation able to generate turbulent bands has a spot-like structure characterized by small- and large-scale structures. Depending on the Reynolds number, this minimal seed evolves in time with two different mechanisms: for $Re \lesssim 1200$ an isolated oblique band is created; whereas, for $Re \gtrsim 1200$, a quasi spanwise-symmetric evolution is observed, giving rise to two distinct bands. Then, reducing the problem complexity to a tilted domain, it is found that two main elements are necessary to induce transition towards turbulent bands: i) a linear energy growth mechanism such as the lift-up for generating streaks inside the turbulent bands; ii) large-scale vortices ensuring spatial localisation.
In the last part of this thesis, in order to investigate the coherent structures usually observed in turbulent flows, the nonlinear optimization technique is extended to the turbulent channel flow and a 'new' mathematical framework for the computation of statistically-invariant coherent solutions is proposed. In both techniques, the unsteady Reynolds-Averaged Navier-Stokes equations written in a perturbative form with respect to the turbulent mean flow are used and solutions with structures at multiple turbulent scales are found.

Keywords: turbulent bands, subcritical transition, nonlinear optimization, turbulent flows, coherent structure, dynamical system.